Two-photon and Three-photon Parametric Interactions in Superconducting Microwave Circuits

by

Chung Wai Sandbo Chang

A thesis
presented to the University of Waterloo
in fulfillment of the
thesis requirement for the degree of
Doctor of Philosophy
in
Electrical and Computer Engineering (Quantum Information)

Waterloo, Ontario, Canada, 2019

Examining Committee Membership

The following served on the Examining Committee for this thesis. The decision of the Examining Committee is by majority vote.

External Examiner:	Dr. Bertrand Reulet Professor, Dept. of Physics, University of Sherbrooke
Supervisor(s):	Dr. Christopher Wilson Professor, Dept. of Electrical and Computer Engineering, University of Waterloo
Internal Member:	Dr. Guo-Xing Miao Professor, Dept. of Electrical and Comptuer Engineering, University of Waterloo
Internal Member:	Dr. David Cory Professor, Dept. of Chemistry, University of Waterloo
Internal-External Member:	Dr. Matteo Mariantoni Professor, Dept. of Physics and Astronomy, University of Waterloo

Author's Declaration

I hereby declare that I am the sole author of this thesis. This is a true copy of the thesis, including any required final revisions, as accepted by my examiners.

I understand that my thesis may be made electronically available to the public.

Abstract

The flexible engineering of superconducting circuits, together with the nonlinearity available from Josephson junctions, have made microwave quantum optics a blooming research field in the past decade. Key experiments originally performed in the optical domain have become very accessible on this microwave-frequency, such that strong atom-field interactions and optical parametric interactions in microwave. From the latter, one example is the implementation of spontaneous parametric downconversion (SPDC). This process is particularly interesting as it can act as a nonclassical radiation source which give a number of potential applications in quantum information processing. We will focus on studying SPDC in microwave throughout this thesis.

In the first half of this thesis, from designs to measurements, we will explore the well-known two-photon parametric processes, SPDC and coherent coupling, which are generated by quadratic Hamiltonians. Using three resonant modes of a SQUID-terminated parametric cavity, we proceeded to combine different two-photon processes in an effort to demonstrate a multipartite nonclassical radiation source. With detailed system gain and noise calibration of our cryogenic microwave network, we confirmed our implementation by experimentally verifying that the generated states contain genuine tripartite entanglement. This multimode entangled radiation source can be an important resource for future experiments on quantum networking.

While two-photon parametric processes have found numerous important applications, they have also been the limit of experiments for over three decades, with higher-order parametric processes seemingly out of reach. In the second half of this thesis, we explore the potential of parametric resonators for achieving such higher-order processes. To do this, we first studied the necessary conditions for accessing cubic Hamiltonians through our SQUID-based interactions. We then fabricated a device dedicated to performing three-photon processes through these cubic Hamiltonians. For the first time, we observed a direct generation of photon triplets by a single SPDC process in microwave . The generation rate can exceed a photon flux density of 60 photon per second per Hertz at the device output, far surpassing any record to date for photon triplets. We studied various pump configurations corresponding to different three-photon SPDC processes starting from a cold vacuum state. Pumping at triple the frequency of a single mode, we observed a phase-space distribution with a non-Gaussian profile which shows strong skewness (third moment) in the quadrature amplitude distribution. We reconstruct the Wigner function of the propagating states from the directly measured moment matrix, demonstrating Wigner negativity. Pumping at the sum frequency of three modes, we observed non-zero coskewness between the quadrature amplitudes of the modes. By analysing the output signals and

comparing their characteristics to the predicted theoretical signatures, we confirm our implementation of three-photon SPDC processes generated by specific cubic Hamiltonians. These types of non-Gaussian states have been suggested as a resource enabling universal quantum computation with continuous variables. Our results thus open up the realm of three-photon quantum optics, enabling a wealth of novel experimental and theoretical studies.

Acknowledgements

Studying a doctorate degree is a long process and at time a challenge. Fortunately, it has never been a lone journey. I am blessed to have people wholeheartedly supporting me throughout the six years from my master study through PhD. I have received tremendous helps from my supervisor, my mentors, my friends, my colleagues and most importantly, my family.

I would like to first express my gratitude to my supervisor, Christopher Wilson, for giving me the valuable entry ticket to this wonderland of quantum physics. Working in Chris's Engineered Quantum System Laboratory has been a privilege. With Chris's generosity, I have the opportunities to attend various workshops and conferences every year which had all been enlightening experiences. Chris's close supervision and patient guidance has been keys to the fruitful results I have achieved throughout my study.

Next I would like to thank my other mentors. I was glad to have Pol working as a postdoctoral fellow in our group when our lab first started. Over cryostat operations, fabrications and techniques in measurements, Pol's professional attitude towards every details has taught me much about the qualities being an experimentalist. I also thank Chris's student, Michael. All my work is essentially derived from the parametric amplifier sample that he generously shared. He has taught me much about the use of equipment and essential skills in working with a cryostat, which were all great help as I first started. Though short, it has been a great time working with and learning from them when they were in Waterloo.

With the complexity of superconducting circuit experiments, we rely heavily on a professional support team to operate our lab. I thank our support from the quantum nanofab facility which allows us to fabricate our device in-house. The cleanroom colleagues including Vito, Nathan, Brian, Matt and others have been very helpful with our often urgent experimental need. I would like to also thank Prof. Britton Plourde and his team in Syracuse University for the help with junction fabrications for our device. I also want to thank Roberto, our technician in IQC, for his always quick and helpful responses to our need on equipment and advice on safety and electrical matters.

I am also grateful to have a strong team by my side throughout my PhD. Having been working with Vadiraj for over four years, from maters with the cryostat to fabrication needs and advice on study, over countless matters he has never hesitated to give me helping hands, I cannot thank him enough and I am very happy to have him as my office mate and as a friend. I would like to also thank Ibrahim for his helps with fabrications. His determination towards his work has always had my respect and I take it as an example that

I should follow. My thanks also go to many other groups mates including Chris, Jimmy, Jamal and many others. I enjoyed every single inspiring conversation with them, be it about science or other stories in life.

Finally, I am thankful to my mother, my brother and my grandma. Allowing me to go far from home to pursue my dream was not an easy decision by any means. Yet, as always, they put me and my will in advance of anything else. Not for a day I don't treasure what I have been given, and with that I believe I can endure every single new challenge.

Dedication

For my family who made it possible.
For my mentors who made it achievable.
For my friends who made it enjoyable.
For the observer who made it meaningful.

Table of Contents

List of Tables

List of Figures

Chapter 1

Introduction

We are now living in an exciting era in which knowledge from multiple fields, such as engineering, physics and mathematics, is slowly merging, enabling experiments that were impossible without the joint effort of multiple disciplines. Out of all the impressive milestones achieved in the past few decades, the achievement by superconducting quantum circuits is indeed a shining example. Superconducting circuits provide a large amount of freedom in designing experiments, giving scientists a test platform of immense flexibility and potential. Researches on superconducting circuits have been blooming across multiple fields in quantum information, from light-matter interactions between artificial atoms and microwave signals [1],[2] to relativistic effects using an on-chip virtual mirror [3], [4], plus many other experiments in quantum thermodynamics [5], [6].

The rapid advancement of microwave quantum optics experiments can be largely attributed to the well-developed theories and experimental methods in quantum optics throughout the last century. Many building blocks in circuit QED, such as on-chip waveguides, resonators and nonlinear elements, were developed closely following cavity QED. Multiple breakthrough experiments with superconducting circuits were inspired by the equivalent results in quantum optics, e.g. realizing entanglement generation [7] on-chip, performing parametric coupling of a single microwave photon between two electric field modes [8], experiments with which to study qubits in a cavity [9], and more. These led to a new category in research now famously known as microwave quantum optics. Microwave quantum optics experiments utilize the advantage of superconducting circuits, wherein we can engineer and tailor-make a circuit to reproduce results that were once difficult to achieve on other platforms. Not only are these results interesting from the standpoint of science, they are also fuelling the fast development of quantum computing and quantum networks using superconducting circuits.

In an effort to advance microwave quantum optics experiments enabled by superconducting circuits, in this thesis we will dive into one category of the quantum optical process: spontaneous parametric downconversions (SPDCs). These interactions are of paramount importance and have been a workhorse for quantum optics. To study the various aspects of SPDCs, we fabricated and measured a device that can achieve various parametric interactions including two-photon and three-photon SPDCs. Importantly, the generated photons in the SPDCs are emitted from the device, forming propagating states, allowing the photons to be analysed and potentially utilized by other experiments. To proceed, the thesis will be presented as follows.

In chapter 2, we will examine the basic building blocks in superconducting circuits which lay the foundation for our microwave quantum optics experiments. We will then discuss various design and fabrication considerations for a device dedicated to generating nonclassical microwave radiation through SPDCs and other parametric interactions.

In chapter 3, with the device in mind, we will move on to discuss the measurement system for the experiments. We will review the microwave network inside the dilution refrigerator, the device attachment and shielding. Then, we will discuss the calibration for system noise, system gain and input noise temperature by using a shot noise tunnelling junction (SNTJ) [10, 11] provided by NIST. Finally, we will utilize these calibrated parameters to characterize the device output states by connecting the room-temperature-measured voltage quadratures to the device output.

In chapter 4, we will study various nonclassical properties given by two-mode downconversion (TMDC), where two photons are generated simultaneously into two frequency modes. Such states are known to exhibit continuous-variable (CV) entanglement, which finds applications in qubit read-out [12, 13], quantum cryptography [14], and more. Thus, it is of great interest to extend CV entanglement beyond two parties. We studied two methods with which to extend bipartite CV entanglement to tripartite by means of combining two parametric processes. We will discuss the experimental procedures for operating the device for the entanglement generation. Finally, we will test and verify the generated output states for tripartite entanglement with two different methods.

In chapter 5, we will consider an application of two-mode downconversion. We propose a protocol named "quantum-enhanced noise radar", in which we attempt to utilize the output of TMDC as the radiation source of a noise radar. In order to benchmark the performance of the quantum output beams, we designed an ideal classical source with the same correlation structure as TMDC, which saturates the classical bound of correlation. Then, we will develop a measurement method which allows us to directly compare the performance of the quantum and classical case in the presence of significant added noise

and signal loss.

In chapter 6, we will explore the generation of three photons by a single SPDC. Generating more than two photons through a single SPDC has been an ongoing endeavour in quantum optics [15, 16, 17, 18], both in theoretical study and in experimental implementation. With a superconducting quantum interference device (SQUID), it becomes possible to engineer and enhance the higher-order nonlinearity necessary for such downconversion processes. In the first half of chapter 4, we will examine the output for a three-photon SPDC in a single mode which gives what we call a single-mode trisqueezed state. The state shows distinct features such as non-Gaussian statistics and a significant third-order moment. Wigner negativity was also predicted for this state. We characterized the distribution of the state statistically, followed by measuring the higher-order moments of the states to reconstruct the Wigner function. In the second half of chapter 4, we will move on to study three-photon SPDCs in two modes and three modes. These multimode trisqueezed states exhibit a significant third moment. They demonstrate strong two- and three-variable coskewness respectively, surprisingly with the absence of any Gaussian correlation between all pairs of modes. This indicates a new type of correlation structure in the CV framework which can enable a new scheme in quantum communications and more. We will study their correlation structure and understand their connection to the ordinary two-photon SPDCs.

Chapter 2

Flux-pumped multimode cavity

The device presented in this thesis is a flux-pumped multimode resonator made from a quarter-wavelength coplanar waveguide (CPW) cavity. At one end the cavity line is shunted to the ground through a SQUID, and at the other end it is overcoupled to the measurement line through a gap capacitor. To understand the devices working principles, we start by reviewing the basic elements used in the device, followed by a discussion surrounding the devices operations.

2.1 Building blocks

2.1.1 Josephson junction

When it comes to superconducting quantum circuits, few will doubt the importance of the Josephson junction. Proposed by Brian Josephson in 1962, it has been the soul of most modern circuit designs, acting as the main source of nonlinearity for qubits and parametric interactions. A Josephson junction is formed by connecting two pieces of a superconductor through a thin barrier which allows Cooper pairs to tunnel through, such that the quantum tunnelling connects the phase of the macroscopic wave function across the junction. The main properties of Josephson junctions can be summarized by two famous Josephson equations:

$$I = I_0 \sin(\phi) \qquad \text{current-phase relation} \tag{2.1}$$

$$V = \frac{\Phi_0}{2\pi}\dot{\phi} \qquad \text{voltage-phase relation} \tag{2.2}$$

Eq. (2.1) relates the phase change of the macroscopic wave function across the junction to the supercurrent, i.e. the stream of Cooper pairs, flowing through it. Along the current direction, the phase across the junction is defined by $\phi = \theta_1 - \theta_2$. I_0 is the critical current of the junction which determines the maximum supercurrent allowed by the junction before it is no longer superconducting. It is a device parameter which can be controlled in the oxidation process during the junction fabrication. We can connect the critical current to the normal state resistance R_n of the junction using the Ambegaokar-Baratoff formula [19], $I_0 = \frac{\pi\Delta}{2eR_n}$. For aluminum, $\frac{\Delta}{e} \approx 0.21$ meV [20]. A desired R_n can then be obtained in fabrication to achieve a target I_0. Eq. (2.2) relates the rate of change of phase to the voltage (potential energy stored) across the junction, where $\Phi_0 = \frac{h}{2e}$ is the superconducting flux quantum.

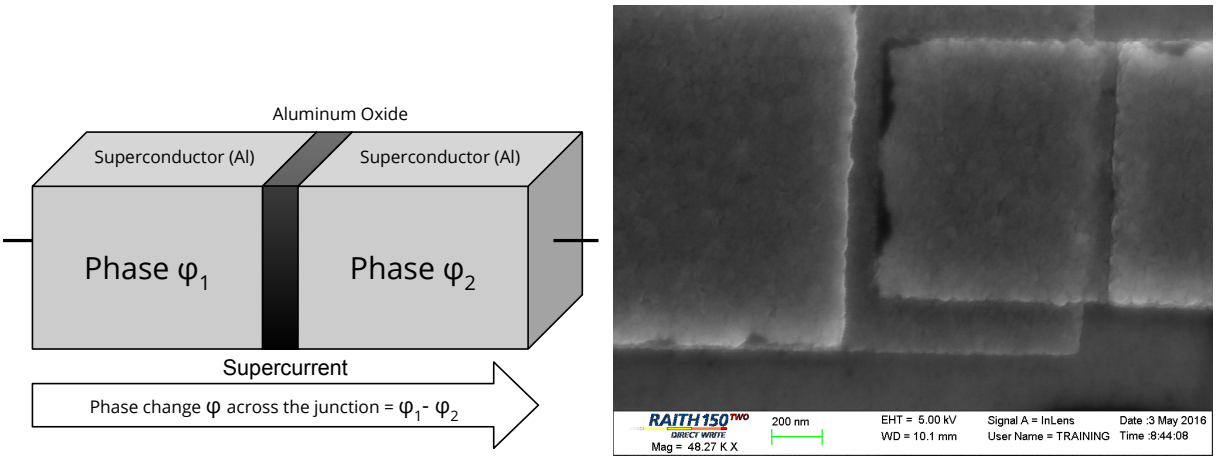

Figure 2.1: An example of a Josephson junction. (top) A diagram of a superconductor-insulator-superconductor Josephson junction. The insulator in the centre forms a barrier where the supercurrent tunnels through. As the supercurrent is passing through the thin barrier, the macroscopic wave function of the superconductor acquires a phase of ϕ_α related to the amount of current. (bottom) An SEM image of an Al-Al_2O_3-Al Josephson junction fabricated with angle evaporation known as the Dolan technique. The junction is defined by the overlapping big and small aluminum pads, and the oxide in between.

2.1.2 dc SQUID

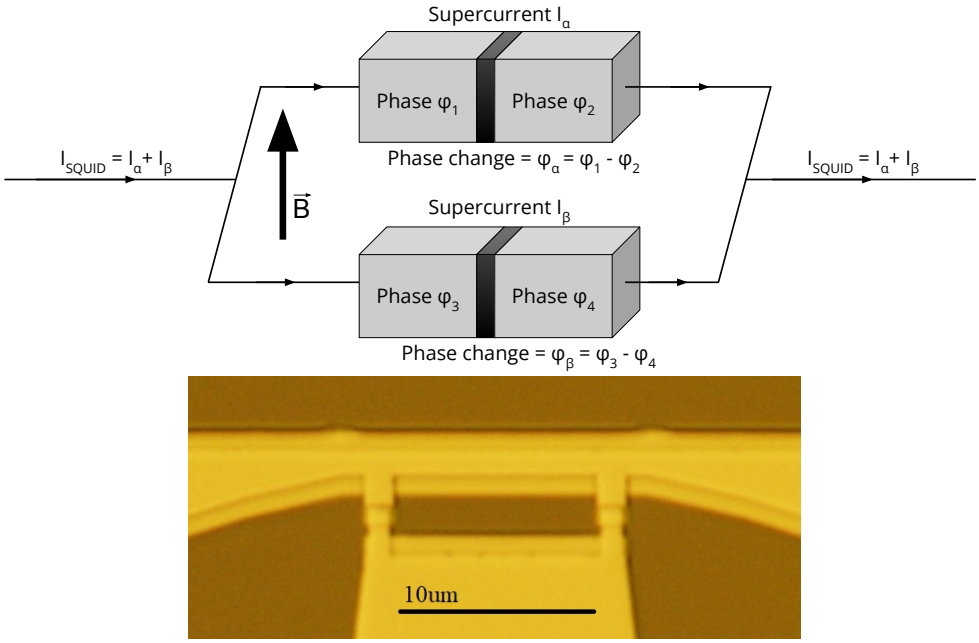

Figure 2.2: An example of a dc SQUID. (top) A simplified model of a dc SQUID. Two junctions shown in Fig. 2.1 are connected together in parallel, forming a closed loop. The loop area together with the magnetic flux density $\vec{B}$ defines the total amount of external flux Φ_{ext} threading through the SQUID. The supercurrent $I_{SQ} = I_\alpha + I_\beta$ flows through the SQUID from left to right in this example. (bottom) An image of a typical dc SQUID design in which the supercurrent passes through it vertically. The small rectangular loop determines the SQUID area. The junctions are formed on the left and right of the loop.

In order to use Josephson junctions as a tunable element, very often two junctions are connected together in parallel to form a dc SQUID (see Fig. 2.2). The phase change of the macroscopic wave function in the superconductor can be described by the supercurrent equation [21],

$$-\frac{2\pi\lambda_L^2\mu_0}{\Phi_0}\vec{J}(\vec{r},t) - \frac{2\pi}{\Phi_0}\vec{A}(\vec{r},t) = \nabla\theta(\vec{r},t), \tag{2.3}$$

where $\lambda_L = \sqrt{\frac{m_c}{\mu_0 n_c(-2e)^2}}$ is the penetration depth of the material, related to its Cooper pairs density n_c and mass m_c. $\vec{J}$ is the supercurrent density, $\vec{A}$ is the electromagnetic vector

potential, and $\nabla\theta$ is the gradient of the phase of the wave function. With a bulky SQUID in which the loop is formed with a superconductor thicker than its penetration depth, due to the Meissner effect [22], no current will flow through the centre of the cross section of the SQUID loop. We can then choose the path in which $\vec{J} = 0$ and take the line integral clockwise along the SQUID in Fig. 2.2 to obtain the round-trip phase change,

$$\oint \nabla\theta(\vec{r},t)\cdot\vec{dl} = (\theta_2-\theta_1)+(\theta_4-\theta_2)+(\theta_3-\theta_4)+(\theta_1-\theta_3).$$

For the sections without junctions, from Eq. 2.3, the phase change is contributed by vector potential only,

$$\begin{aligned}\theta_4-\theta_2 &= \int_2^4 \nabla\theta(\vec{r},t)\cdot\vec{dl} = -\frac{2\pi}{\Phi_0}\int_2^4 \vec{A}(\vec{r},t)\cdot\vec{dl}\\ \theta_1-\theta_3 &= \int_3^1 \nabla\theta(\vec{r},t)\cdot\vec{dl} = -\frac{2\pi}{\Phi_0}\int_3^1 \vec{A}(\vec{r},t)\cdot\vec{dl}.\end{aligned}$$

For the sections with junctions, the phase changes derive from both the vector potential and the junction phases,

$$\begin{aligned}\theta_2-\theta_1 &= \int_1^2 \nabla\theta(\vec{r},t)\cdot\vec{dl} = -\phi_\alpha - \frac{2\pi}{\Phi_0}\int_1^2 \vec{A}(\vec{r},t)\cdot\vec{dl}\\ \theta_3-\theta_4 &= \int_4^3 \nabla\theta(\vec{r},t)\cdot\vec{dl} = \phi_\beta - \frac{2\pi}{\Phi_0}\int_4^3 \vec{A}(\vec{r},t)\cdot\vec{dl}.\end{aligned}$$

In a superconducting loop, as in any quantum mechanical system, the wave function must be single-valued. Thus, the integration of the round-trip phase must be equal to an integer multiple of 2π, as the wave function phase must repeat itself when returning to the same location. As a result, summing the above four equations gives

$$\begin{aligned}2\pi k &= \phi_\beta-\phi_\alpha - \frac{2\pi}{\Phi_0}\oint \vec{A}(\vec{r},t)\cdot\vec{dl}\\ &= \phi_\beta-\phi_\alpha - 2\pi\frac{\Phi_{ext}}{\Phi_0}.\end{aligned} \tag{2.4}$$

Thus, we can control the phase $\phi_\beta - \phi_\alpha$ of the junctions by applying an external flux, making the SQUID a flux-tunable element in the circuit. Not only does it allow a static flux bias to be set, it can also respond to a fast-oscillating magnetic flux of up to typically 20 GHz [23], below the plasma frequency of the SQUID. The fast flux tunability is crucial

for driving the SQUID to perform parametric interactions, which is often referred to as pumping. Physically, pumping can be conducted by fabricating a waveguide called a fast-flux line or pump line, running microwave signals in proximity to the SQUID. The pump signal then creates an oscillating magnetic field which modulates the SQUID junction phase at the chosen pump frequency.

SQUID as a tunable inductive element

With the two Josephson equations Eq. (2.1) and (2.2), the SQUID acts as a nonlinear tunable inductive element in the circuit for small oscillations. To conveniently analyse the tunability, we define the phase across the SQUID, ϕ_{SQ}, and the phase travelling a round trip along the SQUID loop, ϕ_{loop},

$$\phi_{SQ} = \frac{\phi_\beta + \phi_\alpha}{2}$$
$$\phi_{loop} = \phi_\beta - \phi_\alpha = 2\pi \frac{\Phi_{ext}}{\Phi_0},$$

where the second equation makes use of Eq. (2.4) with $k = 0$ for $0 \leq \Phi_{ext} < \Phi_0/2$. Now we are left with only one degree of freedom ϕ_{SQ} in the expression of the SQUID current,

$$\begin{aligned} I_{SQ} &= I_{0,\alpha} \sin\left(\phi_{SQ} - \frac{\phi_{loop}}{2}\right) + I_{0,\beta} \sin\left(\phi_{SQ} + \frac{\phi_{loop}}{2}\right) \\ &= (I_{0,\alpha} + I_{0,\beta}) \sin(\phi_{SQ}) \cos\left(\pi \frac{\Phi_{ext}}{\Phi_0}\right) - (I_{0,\alpha} - I_{0,\beta}) \cos(\phi_{SQ}) \sin\left(\pi \frac{\Phi_{ext}}{\Phi_0}\right) \end{aligned} \tag{2.5}$$

By maximizing I_{SQ} w.r.t. ϕ_{SQ}, we obtain the SQUID critical current,

$$I_{0,SQ} = \sqrt{(I_{0,\alpha} - I_{0,\beta}) + 4 I_{0,\alpha} I_{0,\beta} \cos^2\left(\pi \frac{\Phi_{ext}}{\Phi_0}\right)} \tag{2.6}$$

which shows that the critical current of a SQUID is tunable by external flux, and maximum tunability occurs when the two SQUID junctions are identical.

In a standard flux pump configuration, the SQUID junctions are often designed to be symmetrical in order to give the maximum tunability, such that $I_{0,\alpha} = I_{0,\beta} = I_0$. Eq. (2.5) simplifies to

$$I_{SQ} = 2 I_0 \cos\left(\pi \frac{\Phi_{ext}}{\Phi_0}\right) \sin(\phi_{SQ}) = I_{0,SQ} \sin(\phi_{SQ}), \tag{2.7}$$

such that the SQUID behaves as a single Josephson junction. Differentiating Eq. (2.7) w.r.t. time and using Eq. (2.2),

$$V_{SQ} = \frac{\Phi_0}{2\pi} \frac{1}{2I_0 \left|\cos\left(\pi \frac{\Phi_{ext}}{\Phi_0}\right)\right| \cos\left(\phi_{SQ}\right)} \dot{I}_{SQ}$$

By comparing this to the standard constitutive relation for an inductor, we can then define the effective SQUID inductance

$$L_{SQ} = \frac{\Phi_0}{2\pi} \frac{1}{2I_0 \left|\cos\left(\pi \frac{\Phi_{ext}}{\Phi_0}\right)\right| \cos\left(\phi_{SQ}\right)}. \tag{2.8}$$

The SQUID inductance is therefore tunable by external flux, as well as being nonlinearly dependent on ϕ_{SQ} and Φ_{ext}, which plays an important role in realizing the parametric processes detailed in a later section.

Improving pump coupling by kinetic inductance

Among other reasons, it is desirable to increase the pump coupling to the SQUID in order to minimize the amount of pump power needed to activate the parametric processes. While this can be naively achieved by increasing the SQUID loop area, it comes with the price of an increased sensitivity to magnetic flux noise from the environment, whereby degrading the devices performance. Alternatively, we implemented a novel SQUID design to increase the pump coupling by exploiting kinetic inductance.

Consider a modified SQUID loop in which we replaced the horizontal upper arm with a meandered nanowire, as shown in Fig. 2.3. As the meandered path has a narrow cross section $w \times d$, the assumption that $\vec{J} = 0$ no longer holds for the nanowire part of the SQUID loop. By assuming a homogeneous current density over the cross section of the nanowire of length t, from Eq. (2.3),

$$\begin{aligned} \phi_\beta - \phi_\alpha - 2\pi \frac{\Phi_{ext}}{\Phi_0} - \frac{2\pi}{\Phi_0} \int_{\mathrm{t}} \left(\frac{\lambda_L^2 \mu_0}{wd}\right) I dl &= 2\pi k \\ \phi_\beta - \phi_\alpha - 2\pi \frac{\Phi_{ext}}{\Phi_0} - 2\pi \frac{L_k I}{\Phi_0} &= 2\pi k \end{aligned} \tag{2.9}$$

where $L_k = \left(\frac{t\lambda_L^2 \mu_0}{wd}\right)$ is the kinetic inductance of the meandered nanowire.

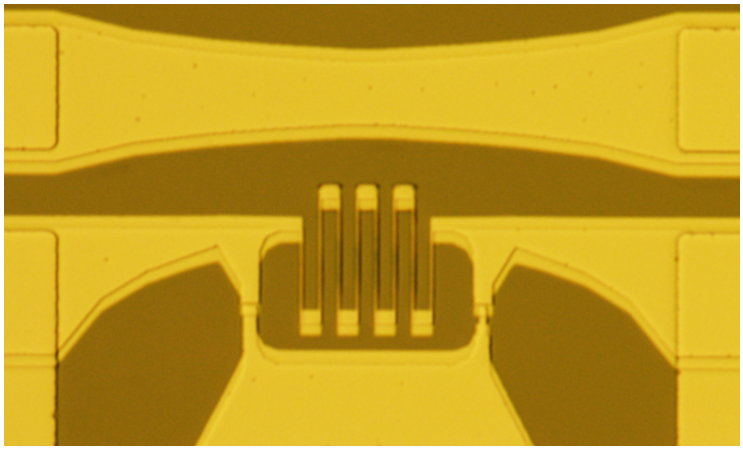

Figure 2.3: A modified SQUID design with increased pump coupling. The top path of the SQUID in Fig. 2.2 is replaced by a nanowire of the superconductor. It is meandered in order to increase the total length and, thus, the total kinetic inductance. With the pump line being above the SQUID, the ground current of the pump signal passes through the nanowire and provides the strong modulation of junction phases.

With this design, the phase across the junctions can be tuned by threading a supercurrent through the nanowire. With CPW waveguides, as much current flows in the ground planes as in the centre conductor. Thus, by fabricating the pump line right above the SQUID, the nanowire efficiently captures half of the ground current of the pump signal. From experiments, we have observed more than 30 dB stronger pump coupling with the SQUID using the kinetic inductance (Fig. 2.3) in comparison to a typical SQUID design (Fig. 2.2).

2.1.3 Coplanar waveguide quarter-wavelength cavity

In this work, the SQUID is utilized as a nonlinear tunable boundary condition in a quarter-wavelength cavity. It is a distributed, one-dimensional resonator which can support multiple frequency modes. We begin by understanding the resonant condition of a quarter-wavelength cavity with a simplified, low-loss transmission line model, followed by developing a numerical method to analyse its frequency modes and coupling to the measurement line.

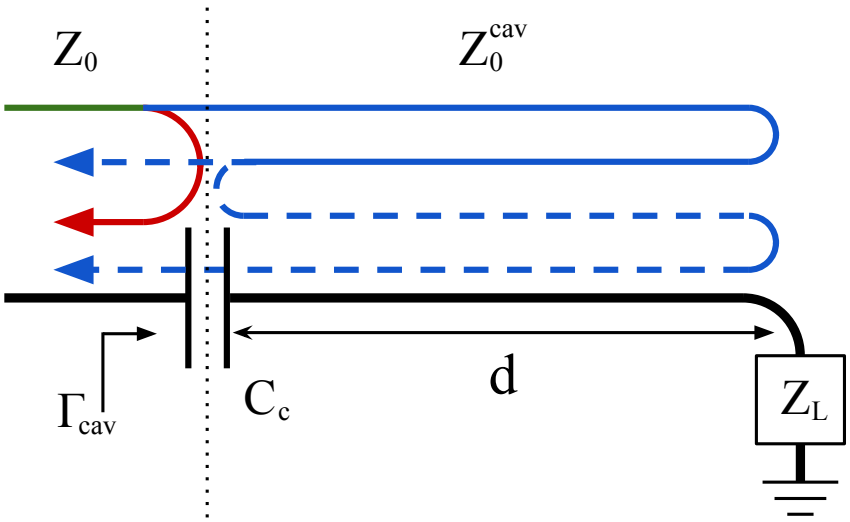

Figure 2.4: A diagram of a capacitively coupled quarter-wavelength cavity. The resonator is formed by sandwiching a waveguide with length d through the coupling capacitor C_c and a load impedance Z_L as the two boundary conditions. The incoming signal (green) impinging on the cavity will be either reflected (red) by the coupling capacitor or transmitted (blue) into the cavity. The transmitted signal will eventually be absorbed by the cavity, or will leave the cavity through the coupling capacitor. A frequency is at resonance with the cavity when the red and blue waves are leaving the cavity with destructive interference.

Considering Fig. 2.4, the incoming signal (green) impinging on the cavity will be partly reflected (red) by the coupling capacitor. The transmitted signal (blue) through the capacitor will be travelling round trips inside of the cavity, losing energy at the boundaries (the capacitor or Z_L) or along the waveguide due to loss. In order for the cavity to store energy of the incoming signals, the two outgoing signals (red and blue) must destructively interfere as they are leaving the cavity.

Locating resonant modes through impedance transformation

To find the resonant frequencies where the above destructive interference occurs, we can calculate the phase of the two outgoing signals above and sweep the frequency in order to check when they are out of phase.

For the reflection at the cavity output due to the coupling capacitor, it is simply given

by the usual reflection relations,

$$\Gamma_c(\omega) = \frac{Z_c(\omega) - Z_0}{Z_c(\omega) + Z_0}$$
$$\phi_\Gamma^c(\omega) = \arctan \frac{\mathrm{Im}\{\Gamma_c(\omega)\}}{\mathrm{Re}\{\Gamma_c(\omega)\}}$$

Typically the impedance of the coupling capacitor is much greater than that of the transmission line; thus, the phase of reflection due to the coupling capacitor is roughly zero.

For the reflection due to the load impedance, it can be found by considering an impedance transformation of the load Z_L due to the cavity waveguide of length d and the coupling capacitor C_c. For a waveguide, its propagation constant is given by $\gamma = \alpha + j\beta$. $\alpha \geq 0$ is the attenuation constant referring to the loss in the waveguide. $\beta = \omega\sqrt{\epsilon_{eff}}/c$ is the phase change per unit length, where ϵ_{eff} is the effective dielectric constant of the CPW structure, which is roughly equal to the average of air and silicon. c is the speed of light in a vacuum. The internal loss of the cavity can be described by the internal quality factor of the cavity, Q_0. With a SQUID-terminated superconducting resonator, the internal quality factor Q_0 is typically above $50,000$. Then, we can estimate α from β by $Q_0 = \frac{\beta}{2\alpha}$ if a small loss needs to be considered. Assuming a low-loss waveguide such that the characteristic impedance of the cavity waveguide Z_0^{cav} is real, the impedance Z_L' at a distance d from Z_L is given by [24]

$$Z_L'(\gamma) = Z_0^{cav} \frac{Z_L + Z_0^{cav} \tanh \gamma d}{Z_0^{cav} + Z_L \tanh \gamma d}. \tag{2.10}$$

The total impedance of the cavity Z_{cav} is then simply the sum of Z_L' and Z_{C_c},

$$Z_{cav} = \frac{1}{j\omega C_c} + Z_L' \tag{2.11}$$

Therefore, we can calculate the magnitude and phase of the overall reflection coefficient of the cavity

$$\Gamma_{cav}(\omega) = \frac{Z_{cav}(\omega) - Z_0}{Z_{cav}(\omega) + Z_0}$$
$$\phi_\Gamma^{cav}(\omega) = \arctan \frac{\mathrm{Im}\{\Gamma^{cav}(\omega)\}}{\mathrm{Re}\{\Gamma^{cav}(\omega)\}}$$

Finally, we can solve the transcendental equation

$$\phi_\Gamma^{cav}(\omega_n) = \phi_\Gamma^c(\omega_n) + (2n+1)\pi \approx (2n+1)\pi \tag{2.12}$$

for the ω_n corresponding to the cavity mode n.

External quality factor estimation

The coupling of the signal in the cavity to the measurement line can be described by the external quality factor Q_e, which is related to the coupling capacitor. To evaluate the external quality factor numerically using the above model, we can assume a lossless resonator by setting $\alpha = 0$ for the propagation constant. Then, following [25], the information of the external quality factor is given by the slope of the phase around the resonant mode ω_n. We define the upper and lower frequencies of the resonant mode $\omega_{n,upper}$ and $\omega_{n,lower}$, respectively corresponding to a point in phase $\phi_\Gamma^{cav}(\omega_n) - \pi/2$ and $\phi_\Gamma^{cav}(\omega_n) + \pi/2$ for the n^{th} resonant mode. The external quality factor is then given by

$$Q_e(n) = \frac{\omega_n}{\omega_{n,upper} - \omega_{n,lower}}.$$

Designing a cavity with uneven mode spacing

An ordinary quarter-wavelength cavity has higher-order modes with frequencies being the odd multiple of the fundamental mode, such that the frequency spacing between successive modes is nominally equal. With the motivation detailed in later chapters, we want to design a cavity which has uneven frequency spacing between the successive resonant modes. Following the approach adopted in [8], this can be achieved by modifying the cavity dispersion relation using a waveguide with varying impedance. Such a cavity can be designed by cascading Eq. (2.10) in a straightforward manner.

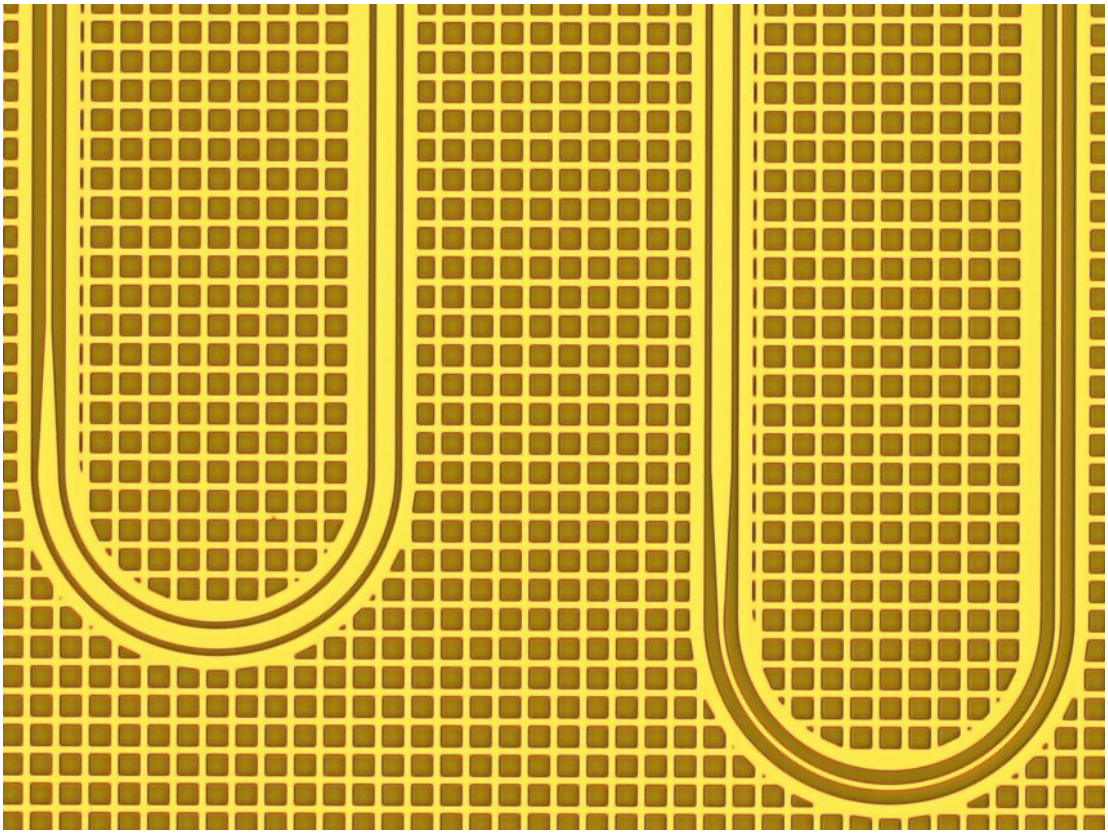

Figure 2.5: An optical image of the varying impedance design.

Using our device as an example, we divide the cavity waveguide into two groups of six sections. The lengths and impedance are summarized in Table. 2.1. The first six waveguide sections are increasing in length roughly according to the first six numbers in the Fibonacci sequence. In each successive section, we also increase the impedance from 5 to 6 Ωs by decreasing the line width of the CPW structure, as illustrated in Fig. 2.5. This is then restarted and repeated from the seventh section (1b in Table. 2.1) for the remaining sections. Tapers of 100 μm are inserted in between each section, with the exception of a longer taper between sections $6a$ and $1b$.

Section	Length [μm]	Impedance [Ω]
1a	790	41
2a	780	47.75
3a	1550	54.12
4a	2330	60.94
5a	3840	67.06
6a	6050	72.2
1b	680	41
2b	789	47.75
3b	1550	54.12
4b	2330	60.94
5b	3840	67.06
6b	6102	72.2
Total length including tapers	32031	

Table 2.1: A table of lengths and impedance of the resonator design. The lengths of the first six sections are designed according to the first six numbers of the Fibonacci sequence, with impedance being increased by roughly 7 Ω in each successive section. This is repeated for the remaining six sections. Tapers of 100 μm are inserted in between each section, with the exception of a longer 400 μm taper between sections $6a$ and $1b$.

To analyse the response of this cavity, we can apply Eq. (2.10) in order to relate the load impedance Z_L to the impedance at the connection between the first and second waveguide sections, Z_{L1}, by using the characteristic impedance of the first waveguide section $Z_0^{cav_1}$. This can then be repeated until we have reached the coupling capacitor,

$$\begin{aligned} Z_{L1}(\gamma) &= Z_0^{cav_1} \frac{Z_L + Z_0^{cav_1} \tanh \gamma d}{Z_0^{cav_1} + Z_L \tanh \gamma d} \\ Z_{L2}(\gamma) &= Z_0^{cav_2} \frac{Z_{L2} + Z_0^{cav_2} \tanh \gamma d}{Z_0^{cav_2} + Z_{L2} \tanh \gamma d} \\ &\vdots \\ Z'_L(\gamma) &= Z_0^{cav_{10}} \frac{Z_{L9} + Z_0^{cav_{10}} \tanh \gamma d}{Z_0^{cav_{10}} + Z_{L9} \tanh \gamma d}, \end{aligned}$$

which can be connected to Eq. (2.11) and apply the same analysis as that of an ordinary quarter-wavelength cavity. Using this particular design, and by substituting Z_L with the

impedance of a SQUID given in 2.1.2, we calculated the expected mode frequencies of our cavity assuming no loss. We found large anharmonicity that was as much as 600 MHz, as shown by the uneven frequency spacing in Fig. 2.6.

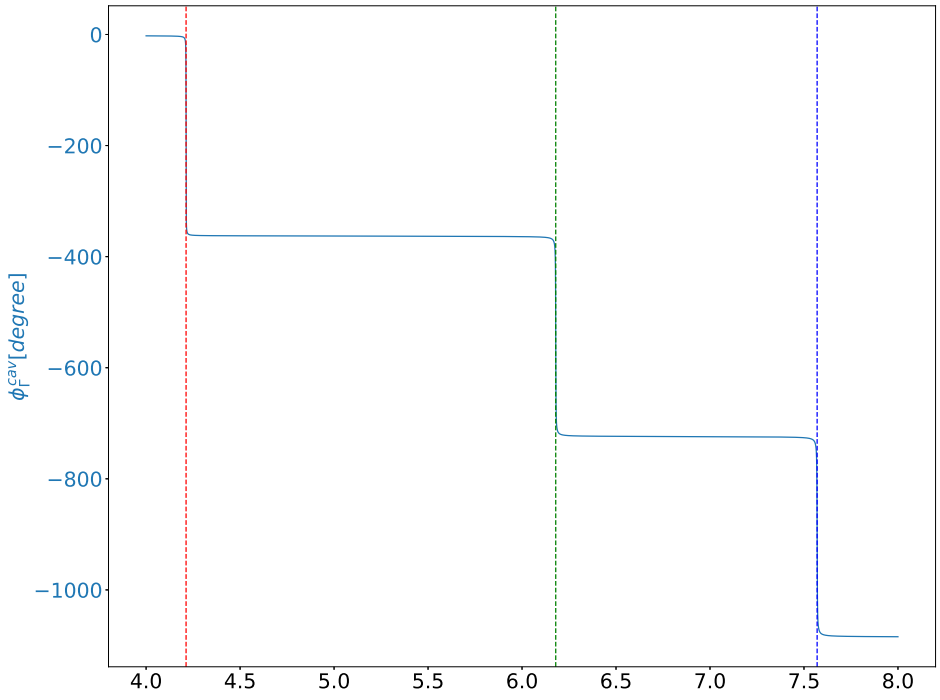

Figure 2.6: The expected unbiased frequency modes of the cavity from 4-8 GHz with the stepped-impedance design. Within the 4-8 GHz bandwidth, modes are expected roughly at 4.21 GHz, 6.18 GHz and 7.57 GHz, respectively represented by the red, green and blue dotted vertical lines. The frequency spacing between the successive modes is 1.97 GHz and 1.39 GHz respectively, giving a difference in spacing of 600 MHz. The simulation assumes a lossless resonator and an external quality factor $Q_e = 6,800$ at the mode around 4 GHz.

2.2 Device operation

By terminating the quarter-wavelength cavity with a SQUID, we arrive at the flux-tunable cavity, as depicted by the schematic in Fig. 2.7. To operate the device, we implemented two flux bias lines. Firstly, we attached a DC coil to the device holder. The coil provides a

static background flux to set the resonant frequency of the modes. Secondly, we fabricated an on-chip fast-flux line next to the SQUID, according to the design detailed in section 2.1.2. It provides the fast-oscillating flux to drive the parametric processes.

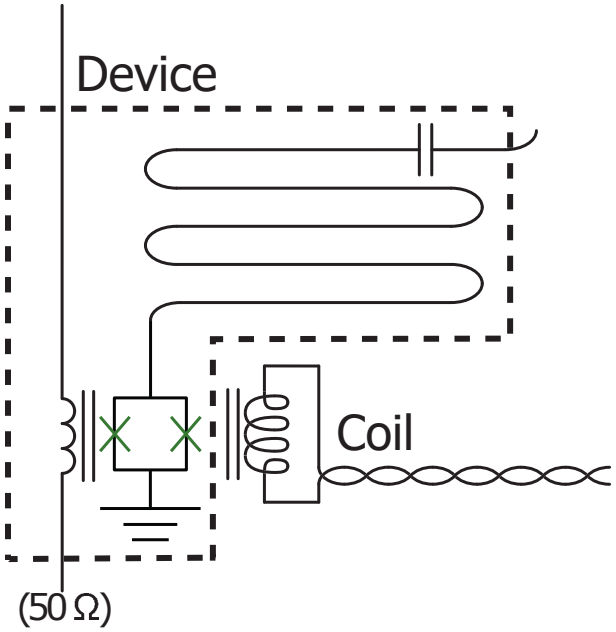

Figure 2.7: A schematic of the device attached to the pump and biasing lines.

2.2.1 Tuning the resonant modes with static external flux

The static flux tuning by the DC coil can be easily observed from the experiment, which is very often performed as a first step in learning the characteristics of the cavity. Upon applying magnetic flux, the SQUID inductance increases from its minimum. As the SQUID acts as a boundary of the cavity, the increasing SQUID inductance gradually transforms the cavity from a quarter-wavelength cavity into a half-wavelength cavity; thus, cavity frequency drops with increasing flux bias. The flux tuning of the cavity frequency is periodic. This follows the periodicity of L_{SQ} with flux according to Eq. (2.8). Within the 4-8 GHz measurement bandwidth of our cryogenic microwave network, we measured the three expected second, third and fourth harmonic modes, with their maximum frequency respectively located at 4.217, 6.171 and 7.578 GHz, as shown in Fig. 2.8.

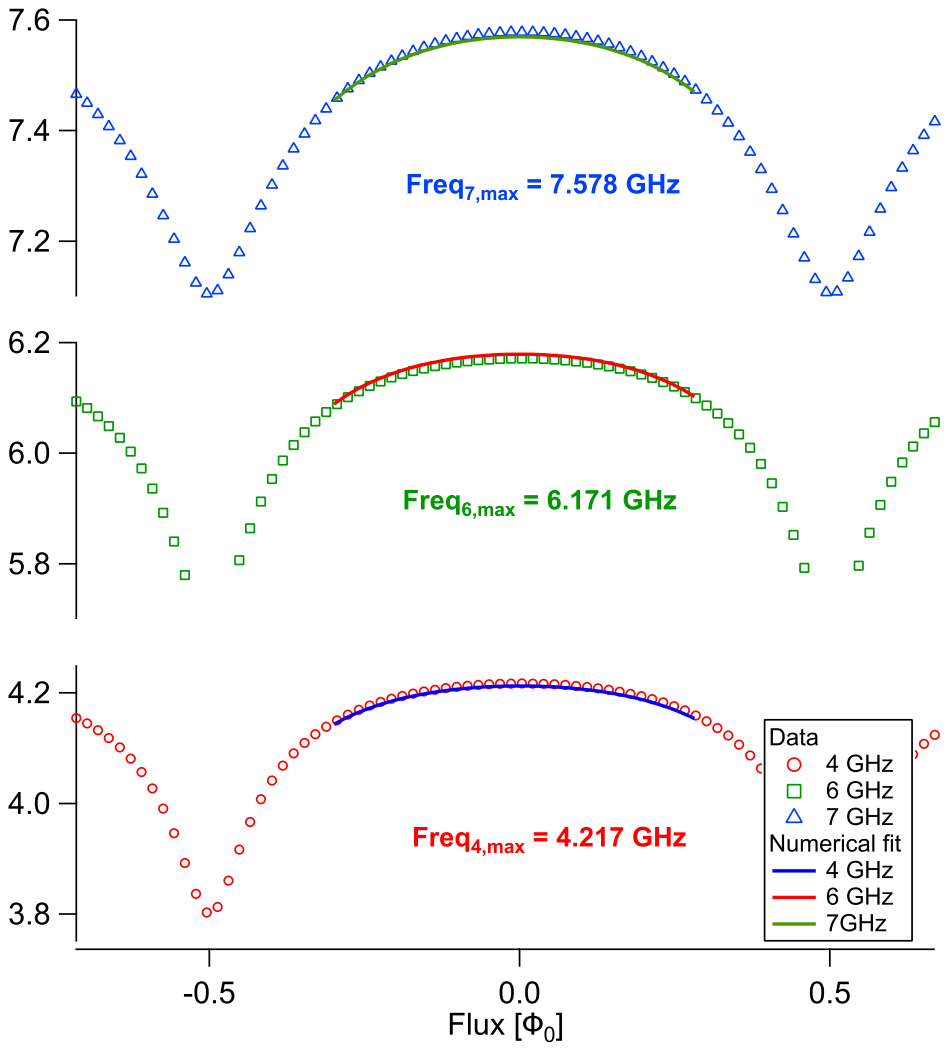

Figure 2.8: Frequency tuning of the cavity. As the external flux increases from zero to $\Phi_0/2$, the SQUID inductance increases, which then reduces the resonant frequencies of the cavity. As all of the modes are coupled to the SQUID, the above tuning of all three resonant modes happens simultaneously. The resonant frequencies drop to a minimum when the external flux equals $\Phi_0/2$, and then increase back to the maximum when the external flux is Φ_0. The lines with markers are the fitted resonant frequencies using the mentioned model 2.1.3 by also taking into account the kinetic inductance and the asymmetry in the SQUID. All three predicted frequency curves were fitted with the same physical parameters.

2.2.2 Interactions among the modes due to the SQUID

The normal modes in the cavity resonator only interact with each other when the SQUID is driven by a pump. To demonstrate the interactions among the modes due to the SQUID, we will proceed with an example in which the SQUID is symmetrical, focusing on the two-mode downconversion process. Other processes can then be understood in a similar manner with a modification of the potential energy of the SQUID and a different choice of pump frequency.

Following [26], we now introduce the concept of node flux, which connects to the voltage in the circuit as $\Phi = \int_{-\infty}^{t} V(\tau) d\tau$. Due to the SQUID, the external flux ($\hat{\Phi}_{ext}$) modulates the cavity flux ($\hat{\Phi}_c$) of the three cavity modes considered. Here, we follow section 2.1.2 and identify that $\hat{\phi}_{loop} = 2\pi \frac{\hat{\Phi}_{ext}}{\Phi_0}$ and $\hat{\phi}_{SQ} = 2\pi \frac{\hat{\Phi}_c}{\Phi_0}$ for a SQUID-terminated cavity. The interaction is thus given by the cosine potential of the SQUID,

$$\hat{H}_{\mathrm{SQ}} = 2E_J \left| \cos\left(\pi \frac{\hat{\Phi}_{ext}}{\Phi_0} \right) \right| \cos\left(2\pi \frac{\hat{\Phi}_c}{\Phi_0} \right), \tag{2.13}$$

where $E_J = \frac{\Phi_0 I_0}{2\pi}$ is the Josephson energy of one junction. In a superconducting resonator, the flux $\hat{\Phi}_k$ of a mode k is proportional to the quadrature operators expressed in terms of the corresponding bosonic operators, i.e. $\hat{\Phi}_k \propto \hat{a}_k + \hat{a}_k^\dagger$. By applying a static flux bias and a pump signal, the external flux takes the form $\hat{\Phi}_{ext} = \Phi_{bias} + \hat{\Phi}_p$. Then, we can expand the cosines to the first order in $\hat{\Phi}_p$ around Φ_{bias}, and to the second order in $\hat{\Phi}_c$,

$$\hat{H}_{\mathrm{SQ}} \approx \hbar g_0 \left(\hat{a}_p + \hat{a}_p^\dagger \right) \left(\hat{a}_1 + \hat{a}_1^\dagger + \hat{a}_2 + \hat{a}_2^\dagger + \hat{a}_3 + \hat{a}_3^\dagger \right)^2 \tag{2.14}$$

where g_0 is the intrinsic interaction strength determined by the coupling between the pump and the cavity modes. With this SQUID interaction, the full Hamiltonian of the flux-pumped resonator with the concerning modes becomes

$$\begin{aligned} \hat{H} &= \hat{H}_0 + \hat{H}_{\mathrm{SQ}} \\ &= \hbar\omega_p \hat{a}_p^\dagger \hat{a}_p + \sum_k \hbar\omega_k \hat{a}_k^\dagger \hat{a}_k + \hat{H}_{\mathrm{SQ}}. \end{aligned} \tag{2.15}$$

We can now switch to the interaction picture via a unitary transformation of $\hat{H}$ by $\hat{U}_0 =$

$e^{\frac{i}{\hbar}\hat{H}_0 t}$,

$$\begin{aligned}\hat{H}_{int} &= i\hbar\dot{\hat{U}}_0\hat{U}_0^\dagger + \hat{U}_0\hat{H}\hat{U}_0^\dagger \\ &= \hbar g_0\left(\hat{a}_p e^{-i\omega_p t} + \hat{a}_p^\dagger e^{i\omega_p t}\right) \\ &\quad\times\left(\hat{a}_1 e^{-i\omega_1 t} + \hat{a}_1^\dagger e^{i\omega_1 t} + \hat{a}_2 e^{-i\omega_2 t} + \hat{a}_2^\dagger e^{i\omega_2 t} + \hat{a}_3 e^{-i\omega_3 t} + \hat{a}_3^\dagger e^{i\omega_3 t}\right)^2, \end{aligned} \tag{2.16}$$

where the free Hamiltonian is transformed away and the SQUID interaction becomes time-dependent.

By expanding the parentheses we obtain many terms with different time dependencies. This naturally provides us with a wide selection of interactions. Moreover, the time dependency of the interactions is an important feature of the SQUID Hamiltonian. It allows us to only selectively activate one or more interactions while leaving the other interactions deactivated. This enables us to perform a sequence of processes in time by pulsing, and we can also combine multiple terms in order to give a more complex interaction.

To selectively activate a two-mode downconversion, we can apply a pump signal with a frequency corresponding to the sum frequency of two cavity modes, e.g. setting $\omega_p = \omega_1 + \omega_2$. Eq. (2.16) becomes

$$\hat{H}_{int} = \hbar g_0\left(\hat{a}_p^\dagger\hat{a}_1\hat{a}_2 + \hat{a}_p\hat{a}_1^\dagger\hat{a}_2^\dagger\right) + \hat{H}_{\text{rot}}(t).$$

Being time-dependent at GHz, the effect of the terms contained by $\hat{H}_{\text{rot}}(t)$ will very quickly average to zero and, thus, can be neglected in comparison to the static term in the Hamiltonian. As a result, we can apply rotating wave approximation and obtain

$$\hat{H}_{\text{RWA}} = \hbar g_0\left(\hat{a}_p^\dagger\hat{a}_1\hat{a}_2 + \hat{a}_p\hat{a}_1^\dagger\hat{a}_2^\dagger\right)$$

Finally, given that the pump signal is a strong, coherent tone, we can apply the parametric approximation [27] and replace $\hat{a}_p$ with the classical amplitude α_p. We then obtain the effective two-photon SPDC Hamiltonian for two modes,

$$\begin{aligned}\hat{H}_{\text{TMDC}} &= \hbar g_0\left(\alpha_p^*\hat{a}_1\hat{a}_2 + \alpha_p\hat{a}_1^\dagger\hat{a}_2^\dagger\right) \\ &= \hbar g_0\left|\alpha_p\right|\left(\hat{a}_1\hat{a}_2 e^{i\theta_p} + \hat{a}_1^\dagger\hat{a}_2^\dagger e^{-i\theta_p}\right) \\ &= \hbar g\left(\hat{a}_1\hat{a}_2 e^{i\theta_p} + \hat{a}_1^\dagger\hat{a}_2^\dagger e^{-i\theta_p}\right)\end{aligned}$$

where $g = g_0\left|\alpha\right|$ is the effective interaction strength, depending on the pump power.

Chapter 3

Device measurement system

In this chapter, I will talk about the measurement system we used for the experiments that we made with superconducting microwave circuits. We will also go through some calibration techniques for obtaining important system parameters, such as system gain and input noise.

In order to generate quantum entanglement and possibly other nonclassical radiation, the device needs to operate at a temperature below ≈ 50 mK so that it is superconducting and, more importantly, in order to minimize thermal excitation. This process is done by attaching the device to the cold stage of a dilution refrigerator. Unfortunately, this makes direct access to the device impossible. The device can only be measured through a cryogenic microwave network which must isolate the device from thermal radiation, as well as amplifying the output signals for detection at room temperature (RT).

In order to verify the nonclassicality in the output signals, we need to know the system gain accurately from the device output to the RT microwave digitizers, plus the thermal excitation at the device. Thus, we also decided to connect a calibration source in our set-up - a shot noise tunnel junction (SNTJ). Here we will present our measurement system and calibration results.

3.1 Device mounting

In order to connect the device to the measurement system, the device is first mounted on a PCB with larger CPW traces. Thermal grease is added between the contact of the device (the silicon side) and the PCB. The CPW lines on the device are wire-bonded to the CPW

lines on the PCB. Each of the PCB traces leads to a SMA connector of a sample holder. The sample holder is made of oxygen-free high-conductivity (OFHC) copper for improved thermalization. Finally, the sample holder is mounted to a cold finger directly attached to the cold stage of the dilution refrigerator as shown in Fig. 3.1.

The DC magnetic coil is mounted on top of the sample holder. An aluminium acting as the magnetic shield is then installed over the cold finger to isolate the device from the surrounding magnetic flux.

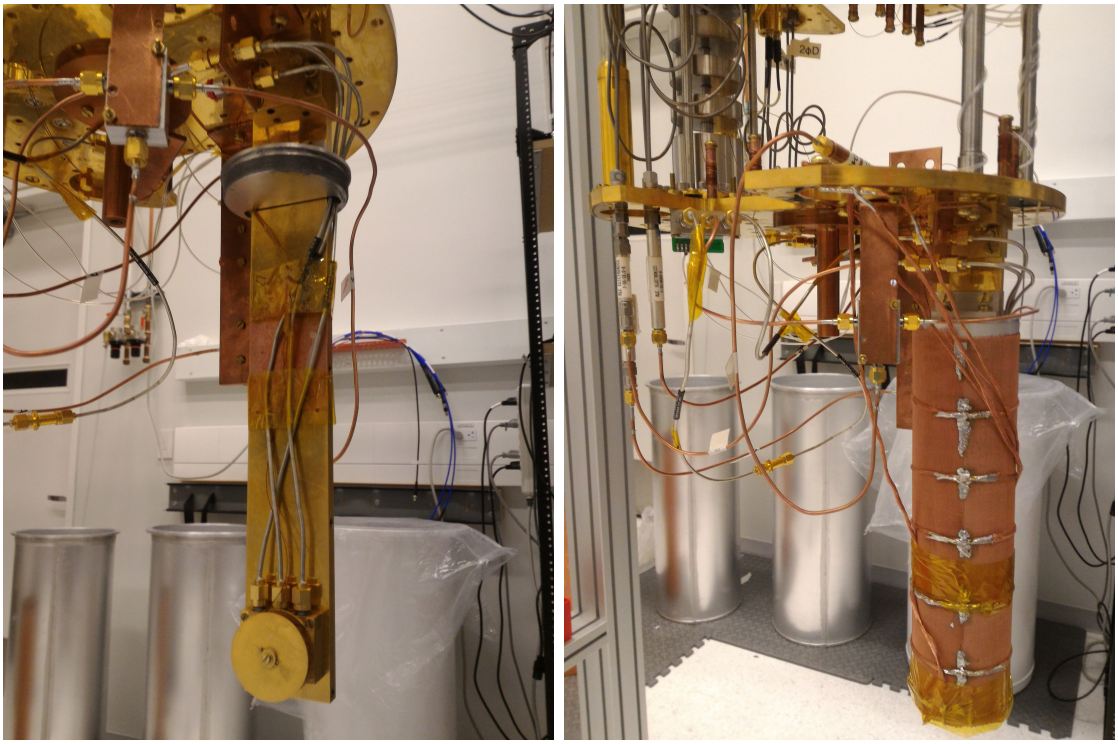

Figure 3.1: Photos of the sample holder attached to the dilution refrigerator. (left) The sample holder is attached to the cold finger which, in turn, is attached directly to the bottom stage of the fridge. The DC magnetic coil is then mounted on top of the device. The material of the coil body, sample holder and cold finger are all OFHC copper. (right). After installing the aluminium magnetic shield. The copper mesh and braids help thermalize the aluminium which becomes a poor thermal conductor when superconducting.

3.2 Microwave network

Our cryogenic-free dilution refrigerator is composed of five cooling stages, with the successive stage having roughly a drop of 10 times in temperature, depicted by Fig. 3.2. Microwave signals are transmitted through 50 Ω SMA cables to the device after some attenuations via the input line and pump line. The output line signal is amplified through a high electron mobility transistor (HEMT) amplifier as the first stage before the further amplification at RT. At the bottom stage, the reflection measurement of the device is performed using circulators. The microwave switch toggles between the device and the SNTJ, respectively for measurement and calibration within the same cooldown.

3.2.1 Cables, attenuation and filtering

	Input		Output		Pump	
Stages	Matl.	Att. [dB]	Matl.	Att. [dB]	Matl.	Att. [dB]
300 K $\Longleftrightarrow$ 50 K	BeCu	20	BeCu	0	BeCu	10
50 K $\Longleftrightarrow$ 3 K	BeCu	20	BeCu	0	BeCu	20
3 K $\Longleftrightarrow$ 800 mK	SS	3	Nb	0	SS	10
800 mK $\Longleftrightarrow$ 100 mK	Nb	3	Nb	1	Nb	6
100 mK $\Longleftrightarrow$ 10 mK	Nb	40	Nb	0	Nb	3
Within the same stage	Cu					

Table 3.1: A list of cable materials and attenuations of the cryogenic microwave network. BeCu: Beryllium copper, SS: Stainless steel, Nb: Niobium, Cu: Copper. The attenuators are attached to the lower temperature stage in each row.

In order to manage the heat load better between temperature stages while still carrying microwave signals, it is important to tailor the cable materials and properties to each of the different stages. Each of the SMA cables used are nominally 50 Ω cables with outer conductor and inner conductor diameters being 2.19 mm and 0.51 mm respectively. BeCu copper cables are used here because of the first two inter-stage connections for their reduced electrical and thermal conductivity, which roughly equals 20% of Cu. As the 50K and 3K stages are cooled directly by the pulse tube compressor, these stages can handle the amount of heat transmitted by BeCu.

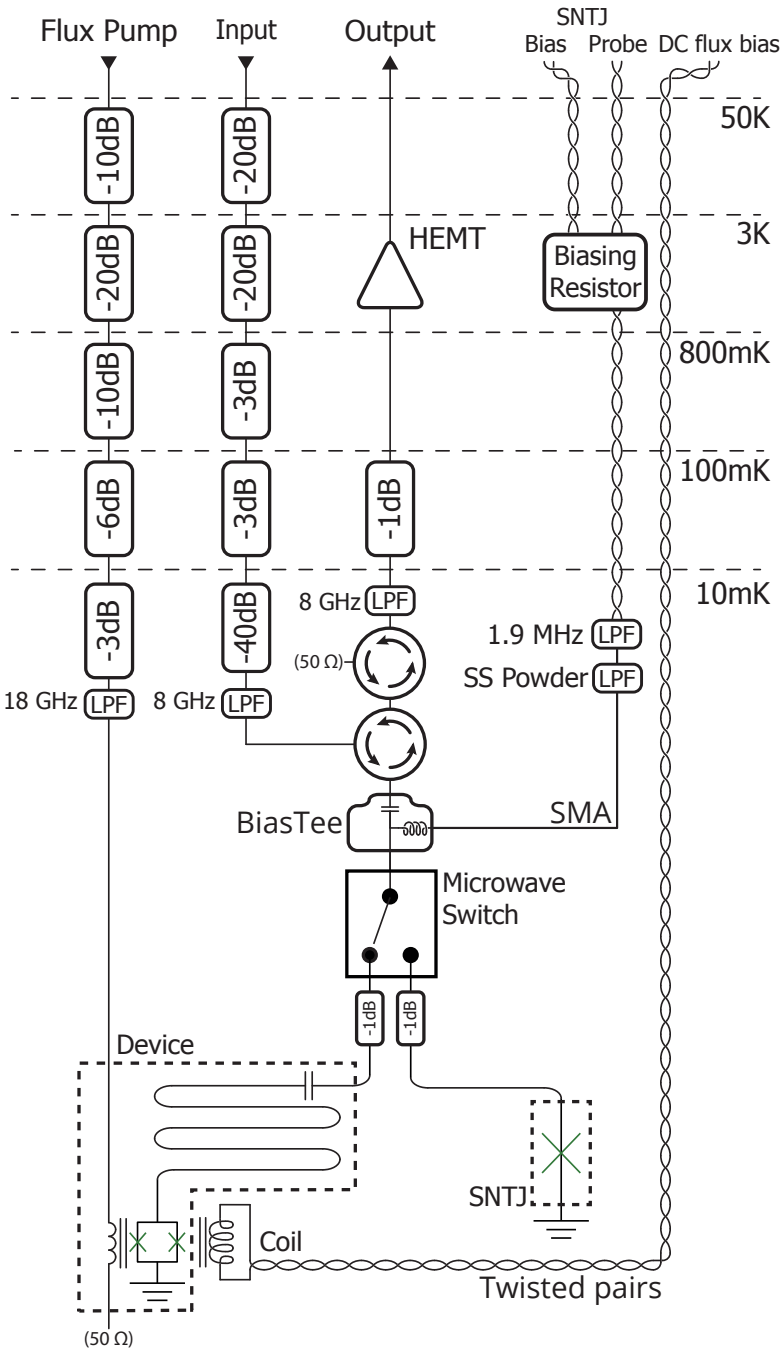

Figure 3.2: The cryogenic microwave network inside the dilution refrigerator.

Down the 800mK stage, higher isolation is required due to the reduced cooling power of these lower stages. Stainless steel cables are used for the input line and pump line between 3K and 800mK stage for a level of thermal conductivity 10 times lower at low temperature compared to BeCu. While also being double in terms of attenuation per unit length, the extra loss is small compared to the overall attenuation that we need to introduce to the system for the input and pump lines.

From 800mK to 10mK, we used Nb cables to undertake superconducting at these temperatures, where they have very high electrical transmission while simultaneously being poor thermal conductors. For the same reason, Nb cable is used to connect from 800mK to the HEMT amplifier to minimize signal loss. Finally, within the same temperature stage standard, Cu cables can be used for low loss and availability of different lengths.

Room temperature radiation can generate a high thermal occupation at microwave frequencies and excite high temperature thermal vacuum state in the device. Besides, the high temperature radiation tends to break Cooper pairs in superconducting thin films, introducing dissipation and ultimately preventing the device from staying superconducting. For this reason, the input lines are strongly attenuated to reduce the amount of high-frequency radiation that reaches the device. In order to estimate how much attenuation is needed, we can consider the photon flux density of the emitted noise by a circuit element. The noise emitted by a circuit element with a nonzero real impedance is proportional to the Bose-Einstein distribution

$$\langle n \rangle_{th} = \frac{1}{e^{\hbar\omega/k_B T} - 1} \tag{3.1}$$

where k_B is Boltzmann constant. Over the frequency range of 4-16 GHz, Eq. (3.1) is roughly linear for a high temperature ($k_B T \gg \hbar\omega$) such that we can attenuate the signal according to the temperature ratio. For example, at 6 GHz,

$$\langle n \rangle_{th}^{T=3\ \mathrm{K}} \,/\, \langle n \rangle_{th}^{T=0.8\ \mathrm{K}} \approx 4.3.$$

However, going further down the stages the scaling becomes exponential, for instances,

$$\langle n \rangle_{th}^{T=100\ \mathrm{mK}} \,/\, \langle n \rangle_{th}^{T=24\ \mathrm{mK}} \approx 9700,$$

which suggests we should have much more attenuation than the temperature ratio.

As a result, it is common to observe a large attenuation being installed at the cold stage in order to attain a sufficient level of isolation. Without other considerations, we want to install as much attenuation as possible to make the device cold. In reality, we are generally limited by the cooling power of the stages and we want to make sure that

we have sufficient input signal power reaching the device. Thus, the value of attenuations should be balanced between the shielding of noise and useful signal.

For the input line to the device, we installed 40 dB at the 10 mK stage to prevent the radiation from reaching the device. Meanwhile, for the pump line, only 3 dB of attenuation is installed at 10 mK because a high pump power is often required by the experiments. In terms of the output, in order to maximize signal-to-noise ratio, we need to minimize the attenuation between the device output and the first stage amplifier. Thus, we only have the 1 dB attenuators installed as a damper to prevent stray resonances along the output line. Hence, in order to attenuate the thermal radiation emitted by the HEMT amplifier (≈ 4 K), circulators are used instead of the attenuator.

As the total noise power seen by the device is proportional to the bandwidth, our usual approach will be to minimize the bandwidth of the system by using different filters. The bandwidth bottleneck of our microwave network is set by the circulators which only span from $4 - 8$ GHz[1]. Therefore, we can filter out everything above 8 GHz using waveguide low-pass filters (LPF) for the input and output lines. In particular, the circulators have poor isolation outside of the $4 - 8$ GHz bandwidth. Being that our pump signals span a wide range from 1-18 GHz, a 18 GHz LPF is thus used.

3.2.2 Signal routing

Signals are routed differently according to the experiments performed. The following section outlines the typical operations for the experiments concerned in this thesis.

Device characterization

The characterization of the device requires a continuous wave (CW) coherent tone to be sent and reflected by the device. For instance, the vector network analyser (VNA) port 1 sends a signal down the input line, routed through the circulator towards the bias tee AC port and leaving from the AC/DC port (bottom) to the microwave switch. The switch is toggled to the device side such that the CW tone is reflected and returned to the circulator. The reflected signal then travels up the output line, is amplified and finally transmitted to the port 2 of the VNA.

[1] Can be expanded to 4-12 GHz using a diplexer to combine different circulators

Driving parametric processes

Parametric processes are driven by CW pump tones generated at RT, transmitted down the pump line to the device. In SPDC, the input port is terminated by a 50 Ω matched resistor at room temperature, such that input to the device is in a near-vacuum state. In order to observe the generated photons, the microwave switch is toggled to the device, such that any emitted signals from the device travel up along the output line.

System calibration

In order to perform system calibration, the microwave switch is toggled to the SNTJ to measure its output noise power corresponding to different bias voltages. The noise signal then travels the same path as the device output above the microwave switch.

3.3 Absolute system calibration

Due to the weak output signal power of a superconducting circuit device, the amplifier chain is always installed as part of the detection system. The amplifier gain and cable loss can vary by a significant amount between room temperature and low temperature. Thus, it is in general inaccurate to estimate the LT system gain using RT measured numbers.

Unfortunately, in many tests of output signals for their quantum properties, it is necessary to compare the exact output signal power to the energy scale of vacuum fluctuation of a bosonic system. Thus, it is necessary to determine the exact gain of the system in order to convert the RT measured power to that at the device output. Together with the other reasons detailed in later sections, we recognise the need for a sophisticated method to calibrate the system gain and thermal excitation at the device. In this thesis, we will demonstrate an absolute system calibration through the use of an SNTJ.

3.3.1 Room temperature noise output from SNTJ

Our calibration source is a SNTJ with matched impedance (50 Ω) to the transmission line, provided by NIST. It is an aluminum tunnel junction fabricated to be 50 Ω at low temperature. In the sample holder of the SNTJ, a strong rare earth magnet is installed in proximity to the junction in order to prevent the junction from going superconducting below the transition temperature. The SNTJ is DC-coupled to the measurement line by

having one end wire bonded to the transmission line and the other bonded to the ground of its sample holder.

The primary electronic thermometry is then performed by measuring the output noise power of the SNTJ after passing through the full amplifier chain, while different bias voltage across the junction is applied. First, when the junction is not biased, or if the bias voltage is low comparing to vacuum fluctuation ($eV \ll \hbar\omega$), the output noise power will be dominated by Johnson-Nyquist noise [28]. Meanwhile, if the bias voltage increases such that ($eV \gg \hbar\omega$), then the junction enters the shot noise regime where the output noise power scales linearly with the bias voltage. Thus, by fitting the measured RT noise data P_{RT} to the expression [10], [11] for a matched SNTJ:

$$P_{RT} = G \cdot BW \cdot k_B \left\{ T_N + \frac{1}{2} \left[\left(\frac{eV + hf}{2k_B} \right) \coth \frac{eV + hf}{2k_B T} + \left(\frac{eV - hf}{2k_B} \right) \coth \frac{eV - hf}{2k_B T} \right] \right\}, \tag{3.2}$$

we can obtain the system gain G measured from the SNTJ output port to detectors at RT. We also obtain the system noise temperature T_N combining amplifier noise and cable loss, and the electron temperature T of the SNTJ. Because the SNTJ absorbs noise over a much broader frequency range than the cavity, we take T to be an upper bound on the input noise temperature at the cavity frequency. The constraints of the fit are the frequency-concerned f and the bandwidth BW of the measurement. The bias voltage V is then the independent variable of the fit. In practice, we can generate a triangular wave at roughly 1 kHz to apply the bias voltage.

3.3.2 AC calibration circuit

In order to make the path calibrated by the SNTJ as similar as possible to the actual device path, the calibration is performed in *situ* with a microwave switch mounted on the cold stage of the cryostat (see Fig. 3.3). The switch is placed as far down the signal path as possible to minimize the different between the signal paths. Then, the two short paths that differ below the switch are made as identical as possible by using a pair of copper cables with the same length and identical room temperature transmissions (see Fig. 3.3).

Image noise rejection

Being a broadband device, SNTJ emits noise over the full bandwidth of our measurement. While this feature allows it to calibrate all the frequency modes of interest, it creates

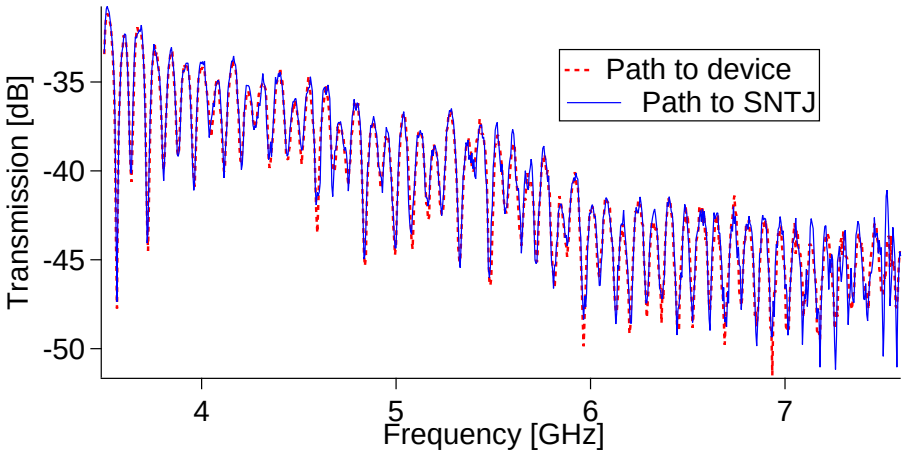

Figure 3.3: The overall transmission through the fridge is reflected by the device and SNTJ, measured at room temperature. The ripples in the transmissions of the two paths overlap, suggesting that the difference due to the short copper cables is very small.

the problem of image noise for the commonly used heterodyne down-conversion detection system which can render the calibration erroneous.

In a heterodyne receiver, a high frequency signal f_S (in GHz range) is first down-converted to an intermediate frequency f_{IF} (in MHz range), which is later digitized. This operation is performed by mixing f_S with an LO signal f_{LO} detuned from f_S by the frequency of the IF signal, i.e. $f_{LO} = f_{IF} + f_S$. In practice, the mixer always down-converts two signals, while one being the desired f_S, it also down-converts an image signal at $f_{IM} = f_S + 2 \times f_{IF}$, such that the IF signal becomes the sum of the desired signal and the image. As a result, this roughly doubles the measured noise from the SNTJ.

While it is possible to just divide the measured noise power by two to take the average and assume the gains are the same for both the signal and image, this is generally inaccurate. From the experiments, we have seen that this assumption creates a systematic error of a few percent between the calibrated signal powers by different digitizers. In order to solve this image-noise problem, we fabricated three narrow bandwidths ($\approx$ 300 MHz) band-pass filter centered at the three cavity modes for our measurement. This operation reduces the power of the image signal by 20 dB comparing to the desired signal, allowing a more accurate calibration.

3.3.3 DC calibration circuit

The voltage across the SNTJ is applied using the biasing circuit shown in Fig. 3.4 with an arbitrary function generator at RT. The resistance of all the components is explicitly measured. A 4-wire biasing scheme is used from room temperature down to the cold bias tee. In order to be compatible with the microwave system, the bias is converted into a 2-wire scheme at this point.

Voltage biasing and measurement

In order to convert a voltage applied from RT to that across the SNTJ, we implemented a series of voltage divisions inside the cryostat. The resistors are thermalized to 4 K in order to minimize thermal noise according to Eq. (3.1). We divided the conversion circuit into two stages, wherein the first stage involves a voltage divider with a ratio roughly of $1:10$ which can be adjusted as needed. Following the divider, a large resistor R_1 is connected in series with the rest of the circuit, where we then use the measured resistance of the other components to calculate the expected voltage drop accurately across the SNTJ. The conversion factor is $V_{\mathrm{SNTJ}} = 0.845 \times V_{\mathrm{probe}}$.

With the measured probe voltage and this conversion, we obtain the voltage across the SNTJ to high precision. The voltage at the probe points is measured differentially with an INA110 precision instrumentation amplifier at room temperature. The remaining voltage division between the probe points and the SNTJ is calculated using the measured resistance values in Fig. 3.4.

To verify the connections before the cooldown, we performed a RT voltage measurement using a sine wave at 1 kHz, with a peak-to-peak voltage of 10 V. As the SCwire is normal and resistive, we will obtain a higher V_{probe} than the one shown in the circuit above for low temperature. As expected, we measured a higher $V_{\mathrm{probe}} = 600$ μVpp comparing to when the system is cold which corresponds accurately to the simulated value for $V_{\mathrm{probe}} = 600$ μVpp. In the same RT test, a second INA was installed at the SNTJ location to measure the drop across a 50 Ω resistor. We measured $V_{\mathrm{SNTJ}} = 384$ μVpp, compared to the expected 371 μVpp from the simulation. The triangular wave measurement was repeated and similar results were obtained.

Circuit grounding

The SNTJ is grounded to the sample holder which then connects directly to the fridge ground. As a result, a stray return path is created through the other microwave equipment

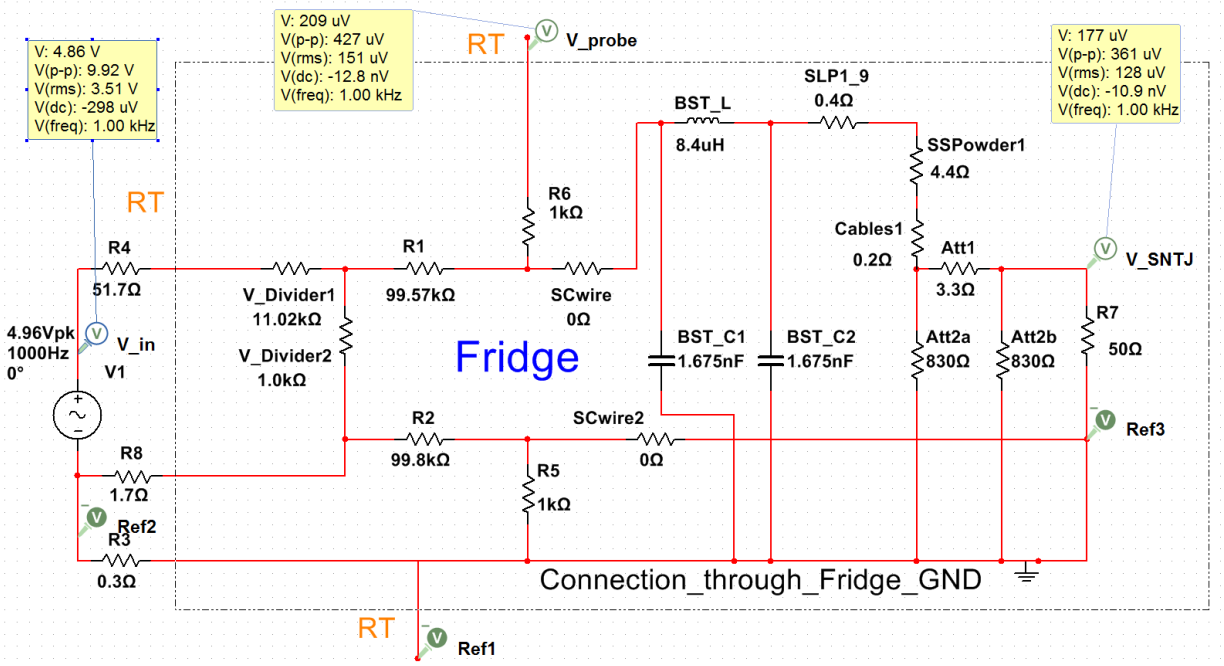

Figure 3.4: The schematic of the DC circuit for SNTJ calibration for low temperature.

to the AFG. In turn, this creates a low-resistance path which routes the return biasing current from the fridge ground to the wall socket, and finally back to the AFG, by-passing the biasing resistor R_2 in Fig. 3.4. Not only is this path noisy, the resistance ($\approx 30\ \Omega$) has also created a background current for the experiment which resulted in a DC offset in the SNTJ bias.

With all the microwave devices this path is difficult to remove. Our solution was thus to use a thick copper braid to connect the fridge ground directly to the ground of the AFG. This operation effectively shorts out the stray grounding path, giving a quieter and offset-free DC biasing for the SNTJ measurement.

Thermalization of components

The biasing resistors used are metal film resistors with small temperature coefficient of resistance (10 ppm/C), making them particularly suitable for low temperature applications. In first experiments, we thermalized the resistors by casting them in Stycast. However, we found that differential contraction of the parts on cooling tended to destroy the resistors.

With this fact in mind, to provide the flexibility they need when thermalizing, we clamped the resistor by OFHC copper pieces and mounted them onto the 3 K plate directly, with the resistor partially immersed in thermal grease. Most of the other filters and cables are thermalized by their AC connections only, with some aids from copper tapes. The microwave switch and the SNTJ holder are clamped by bigger OFHC copper plates and mounted to the MXC stage to ensure good thermalization.

Protective measures when operating SNTJ

SNTJ is a DC coupled junction. Unlike a capacitively coupled device, SNTJ is exposed to the direct current and is easily destroyed by a discharge or a bias voltage too high. While the latter is prevented by having the large biasing resistor in series with the junction, the former can happen due to static discharge, or simply because of the charges building up. Thus, we need to make sure the SNTJ is always seeing a closed circuit all the time. First, this is done by using a RT switching circuiting which toggles the SNTJ bias and probe connections (see Fig. 3.2) either to the AFG or to the ground. Then, whenever we need to change any AC or DC connections to the fridge, we simply toggle to the short-circuit side to protect the SNTJ.

Second, we need to make sure the SNTJ is in a closed circuit when the low temperature microwave switch is toggled to the device. By default, the switch will leave the SNTJ open, which is avoided by attaching a 1 dB attenuator below the switch. Then, the shunt resistor in the attenuator's pi network always closes the circuit for the SNTJ. In order to keep the transmissions identical, we also attached the same 1 dB attenuator for the path to the device.

3.3.4 Performing the calibration

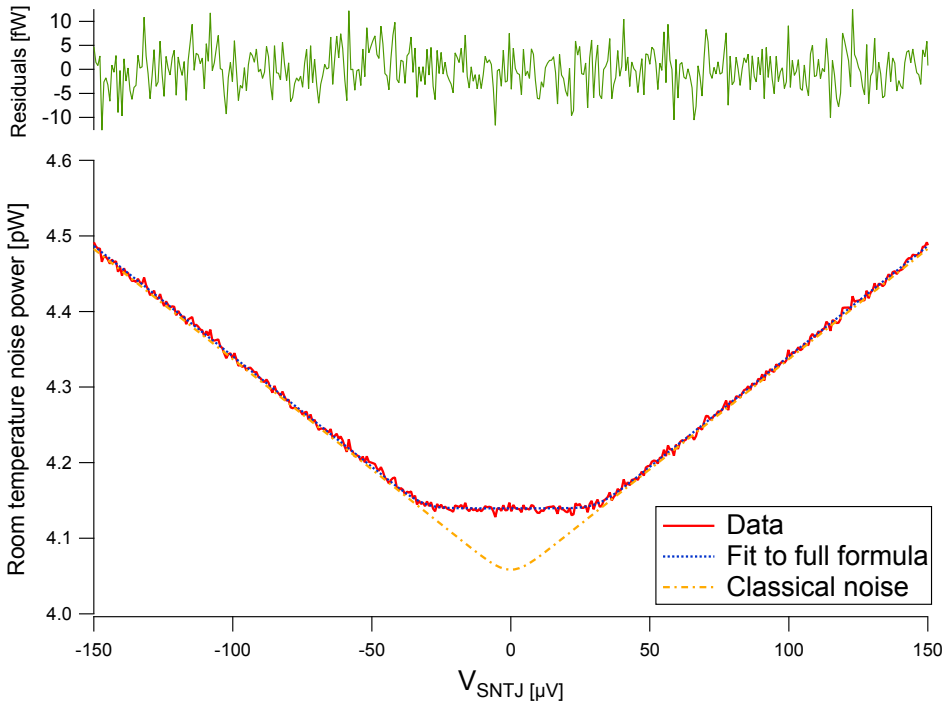

Figure 3.5: Fit of the noise power from the SNTJ measure at room temperature for a mode at 7.554 GHz. The noise power (solid red) is shown as a function of the SNTJ bias voltage. The theory curve (dotted blue) shows the fit to Eq. (3.2), from which we extract the system gain, G, the physical electron temperature corresponding to the electron temperature at the SNTJ, T, and the system noise temperature, T_N. The green curve on top shows the residuals of the fit.
The flatness of the zero-voltage power is a strong qualitative indication that the system is in the quantum regime where $\hbar\omega \gg k_B T$. By means of a comparison, we included the corresponding classical curve (dash-dot orange), with the frequency set to $f = 0$, such that the vacuum noise contribution is zero.

To perform the calibration, we toggle the base microwave switch to the SNTJ. We then applied a triangular wave from the RT AFG at 1 kHz with a peak-to-peak voltage at 10 Vpp. At the same time, we measure the probe voltage and find $V_{\text{probe}} = 429$ μVpp which is very close to the simulated voltage at $V_{\text{probe}} = 427$ μVpp. Using the conversion factor of

our DC circuit, we then calculated $V_{\mathrm{SNTJ}} = 361$ μVpp. This measurement corresponds to an amplitude of roughly $7 \times h(6\mathrm{GHz})/e$, so fulfilling $eV \gg \hbar\omega$ in Eq. (3.2).

Having checked the DC bias, we then measure the noise output centered at the cavity modes. With some averaging, we are able to obtain the plots of RT noise against voltage across the SNTJ for the different modes.

As a demonstration, the noise power measurement and the corresponding fit is shown in Fig. 3.5 for a mode around 7.5 GHz. We obtained the system gain $G = 45.6$ dB, $T = 25.8$ mK and $T_N = 8.03$ K. The flatness of the curve near zero voltage is a strong qualitative indication that the system is in the quantum regime where $\hbar\omega \gg k_B T$. To provide a comparison, we included the corresponding classical curve, with the fitting frequency in Eq. (3.2) set to zero such that there is no contribution from the vacuum fluctuation. This clearly illustrates the existence of vacuum fluctuation in a bosonic mode and its important role as quantum noise in the SNTJ calibration.

In order to account for any subtle differences in the transmission towards each digitizer, calibrations need to be performed with the individual digitizer for each frequency mode. Typically, 500-1000 triggers with gives 1 million samples of noise measurement are averaged in order to obtain a sufficient set of data necessary to reduce the uncertainty in the calibrated system gain and input noise temperature.

3.4 Conversion of acquired data at digitizers to device output

Having the system gain and input noise temperature, the next step is to correctly interpret the data acquired by the digitizer at room temperature and convert them back to the device output variances and covariances. We will demonstrate the conversion by taking two cavity modes as examples. This method can be extended to other modes in a straightforward manner.

3.4.1 Interpretation of acquired data at the digitizer

To begin with, we want to make a connection between the acquired data and the signal entering the digitizer. At the digitizer, the data is acquired as a time series of the I and Q quadrature amplitude of the signals. The analysis can be started by considering the voltage operator of a microwave signal in a transmission line, derived in [3]. For clarity, we will use

the operators in the continuum limit, $\hat{X}(\omega), \hat{P}(\omega)$ to denote room temperature quadrature terms, and $\hat{A}(\omega), \hat{A}^\dagger(\omega)$ as the room temperature bosonic operators. To achieve consistency, we will use the lower-case letters to denote the device output operators, i.e. $\hat{x}(\omega), \hat{p}(\omega)$ as the device output quadrature terms and $\hat{a}(\omega), \hat{a}^\dagger(\omega)$ as the device output bosonic operators. We are using the convention $\hat{X}(\omega) = \hat{A}(\omega) + \hat{A}^\dagger(\omega), \hat{P}(\omega) = -i\left(\hat{A}(\omega) - \hat{A}^\dagger(\omega)\right)$, where we define the quadrature operators from bosonic operators with a prefactor of one. The voltage operator in time domain has the form

$$\hat{V}(x,t) = \int_0^\infty d\omega \sqrt{\frac{\hbar\omega Z_0}{4\pi}} \left(\hat{A}(\omega)e^{-i(\omega t - kx)} + \hat{A}^\dagger(\omega)e^{i(\omega t - kx)}\right).$$

We can separate the quadrature terms by considering the cos and sin components

$$\begin{aligned}\hat{V}(x,t) &= \int_0^\infty d\omega \sqrt{\frac{\hbar\omega Z_0}{4\pi}} \hat{X}(\omega)\cos(\omega t - kx) \\ &\qquad + \int_0^\infty d\omega \sqrt{\frac{\hbar\omega Z_0}{4\pi}} \hat{P}(\omega)\sin(\omega t - kx) \\ &= \hat{I}(x,t) + \hat{Q}(x,t).\end{aligned}$$

Starting with the $\hat{I}(x,t)$ term and letting the digitizer sit at $x = 0$, we can compute the variance at room temperature over a bandwidth BW centered at ω_0,

$$\langle \hat{I}(0,t)\hat{I}(0,t)\rangle = \frac{\hbar Z_0}{4\pi} \int_{\omega_0 - \pi BW}^{\omega_0 + \pi BW} \int_{\omega_0 - \pi BW}^{\omega_0 + \pi BW} d\omega d\omega' \sqrt{\omega}\sqrt{\omega'} \left\langle \hat{X}(\omega)\hat{X}(\omega')\right\rangle \cos(\omega t)\cos(\omega' t)$$

We can get rid of one integral by recognizing that the continuous bosonic operators have the commutator $\left[\hat{A}(\omega), \hat{A}^\dagger(\omega')\right] = \delta(\omega - \omega')$, and the different frequency modes are orthogonal for a stationary process, such that $\left\langle \hat{X}(\omega)\hat{X}(\omega')\right\rangle = S_{XX}(\omega)\delta(\omega - \omega')$, where $S_{XX}(\omega)$ is the power spectral density. For a quantum thermal state, $S_{XX}(\omega) = \coth \frac{\hbar\omega}{2k_B T}$.

$$\begin{aligned}\langle \hat{I}(0,t)\hat{I}(0,t)\rangle &= \frac{\hbar Z_0}{4\pi} \int_{\omega_0 - \pi BW}^{\omega_0 + \pi BW} d\omega S_{XX}(\omega)\omega \cos^2 \omega t \\ &= \frac{1}{2}\frac{\hbar Z_0}{4\pi} \int_{\omega_0 - \pi BW}^{\omega_0 + \pi BW} d\omega S_{XX}(\omega)\omega \left(\cos 2\omega t + 1\right). \end{aligned} \tag{3.3}$$

In the measurement the 2ω component will be filtered out over the time average. We will also evaluate the integral uniquely over a narrow bandwidth, $2\pi BW$, determined by

the sampling frequency around a center frequency, ω_0. Finally, assuming a flat output spectrum over the bandwidth of interest,

$$\begin{aligned}\langle \hat{I}(0,t)\hat{I}(0,t)\rangle &\approx \frac{1}{2}\frac{\hbar Z_0}{4\pi}\int_{\omega_0-\pi BW}^{\omega_0+\pi BW} d\omega\ \omega S_{XX}(\omega) \\ &= \frac{\hbar\omega_0 Z_0 BW}{4} S_{XX}(\omega_0),\end{aligned}$$

such that

$$S_{XX}(\omega_0) = \frac{4\langle \hat{I}(0,t)\hat{I}(0,t)\rangle}{\hbar\omega_0 Z_0 BW} \tag{3.4}$$

which is measured in a unit of number of photons per second per Hertz. The other variances and covariances can be interpreted in a similar way; thus the derivations are not repeated here.

3.4.2 Conversion of operators from room temperature to device output

In the previous section, we have connected the spectral density to the acquired data from the measurement. Next, we need to find out how the spectral density is scaled by the amplifier chain.

System output variance

The scaling can be conveniently analysed using discrete mode bosonic operators. Follow [29], the input-output relationship of a linear, phase-preserving amplifier can be described as

$$\hat{A}_k = \sqrt{G_k}\hat{a}_k + \sqrt{G_k - 1}\hat{h}_k^\dagger \qquad \text{for mode } k, \tag{3.5}$$

where $\hat{a}_k, \hat{A}_k$ are respectively the input and output bosonic operators of the amplifier chain. Note that $\hat{a}_k$ is also the output of our device. G_k is the overall system gain and $\hat{h}_k^\dagger$ is the

bosonic operator of the added noise by the system. For the variance in mode 1,

$$\begin{aligned}\left\langle \hat{X}_1^2 \right\rangle &= \langle \hat{A}_1\hat{A}_1 + \hat{A}_1\hat{A}_1^\dagger + \hat{A}_1^\dagger\hat{A}_1 + \hat{A}_1^\dagger\hat{A}_1^\dagger\rangle \\ &= (G_1)\langle \hat{a}_1\hat{a}_1 + \hat{a}_1\hat{a}_1^\dagger + \hat{a}_1^\dagger\hat{a}_1 + \hat{a}_1^\dagger\hat{a}_1^\dagger\rangle + (G_1-1)\langle \hat{h}_1\hat{h}_1 + \hat{h}_1\hat{h}_1^\dagger + \hat{h}_1^\dagger\hat{h}_1 + \hat{h}_1^\dagger\hat{h}_1^\dagger\rangle \\ &\quad + \sqrt{G_1(G_1-1)}\left(\cancelto{0}{\langle \hat{x}_1\hat{x}_{HEMT,1}\rangle} + \cancelto{0}{\langle \hat{x}_{HEMT,1}\hat{x}_1\rangle}\right) \\ &= G_1\langle \hat{x}_1^2\rangle + (G_1-1)\langle \hat{x}_{HEMT,1}^2\rangle, \end{aligned} \tag{3.6}$$

where we denote the added system noise by $\langle \hat{x}_{HEMT,1}^2\rangle$ for mode 1.

Next we derive the output $\langle \hat{x}_1^2\rangle$ from the device, by assuming the device works as an ideal two-mode squeezer (see Eq. (4.4),(4.5)). Here we have the device output variance as

$$\begin{aligned}\langle \hat{x}_1^2\rangle &= \langle \hat{x}_1^{in}\hat{x}_1^{in}\rangle \cosh^2 r + \langle \hat{x}_1^{in}\hat{x}_2^{in}\rangle \cosh r \sinh r \\ &\quad + \langle \hat{x}_2^{in}\hat{x}_1^{in}\rangle \sinh r \cosh r + \langle \hat{x}_2^{in}\hat{x}_2^{in}\rangle \sinh^2 r\end{aligned}$$

where the superscript *in* refers to the input state. For simplicity, we assume that the initial states are quantum thermal states at temperature T_1 and T_2. With these states, the expectation values of the photon nonconserving terms vanish. We can then apply the usual discrete mode bosonic commutation relations to arrive at

$$\begin{aligned}\langle \hat{x}_1^2\rangle &= \langle \cancelto{0}{\hat{a}_1\hat{a}_1} + \hat{a}_1\hat{a}_1^\dagger + \hat{a}_1^\dagger\hat{a}_1 + \cancelto{0}{\hat{a}_1^\dagger\hat{a}_1^\dagger}\rangle \cosh^2 r + \frac{1}{2}\langle \cancelto{0}{\hat{a}_2\hat{a}_2} + \hat{a}_2\hat{a}_2^\dagger + \hat{a}_2^\dagger\hat{a}_2 + \cancelto{0}{\hat{a}_2^\dagger\hat{a}_2^\dagger}\rangle \sinh^2 r \\ &\quad + \langle \cancelto{0}{\hat{a}_1\hat{a}_2} + \cancelto{0}{\hat{a}_2^\dagger\hat{a}_1} + \cancelto{0}{\hat{a}_1\hat{a}_2^\dagger} + \cancelto{0}{\hat{a}_1^\dagger\hat{a}_2}\rangle \cosh r \sinh r \\ &= g_1 \coth\frac{\hbar\omega_1}{2k_BT_1} + (g_1-1)\coth\frac{\hbar\omega_1}{2k_BT_2} \\ &= (g_1-1)\left(\coth\frac{\hbar\omega_1}{2k_BT_1} + \coth\frac{\hbar\omega_1}{2k_BT_2}\right) + \coth\frac{\hbar\omega_1}{2k_BT_1}\end{aligned} \tag{3.7}$$

where $g_1 = \cosh^2 r$ is the power gain of the parametric amplifier. r is the squeezing parameter by a SPDC, which will be detailed in section 4.1. In the last two lines we have used the thermal photon distribution $\langle \hat{a}^\dagger\hat{a}\rangle_{Thermal} = 1/(e^{\hbar\omega/k_BT} - 1)$.

3.4.3 Room temperature output with pump on and off

By substituting (3.7) to (3.6), we can describe the signal output of the amplifier chain for the two cases with the pump turned on and off.

Pump ON

With the pump turned on we keep g_1 in the equation, as given by the gain of the parametric amplification. The system output for mode 1 is then given by

$$\begin{aligned}\langle \hat{X}_1^2 \rangle_{ON} &= G_1 \langle \hat{x}_1^2 \rangle + (G_1 - 1)\langle \hat{x}_{HEMT,1}^2 \rangle \\ &= G_1 \left(g_1 \coth \frac{\hbar\omega_1}{2k_B T_1} + (g_1 - 1) \coth \frac{\hbar\omega_2}{2k_B T_2} \right) + (G_1 - 1)\langle \hat{x}_{HEMT,1}^2 \rangle. \end{aligned} \tag{3.8}$$

Pump OFF

With the pump turned off, we simply set $g_1 = 1$ in Eq. (3.8) and get

$$\langle \hat{X}_1^2 \rangle_{OFF} = G_1 \coth \frac{\hbar\omega_1}{2k_B T_1} + (G_1 - 1)\langle \hat{x}_{HEMT,1}^2 \rangle. \tag{3.9}$$

3.4.4 Device output variance

The device output variance can be obtained from the ON-OFF measurement. By subtracting the ON data by the OFF data,

$$\langle \hat{X}_1^2 \rangle_{ON} - \langle \hat{X}_1^2 \rangle_{OFF} = G_1 \left(\langle \hat{x}_1^2 \rangle - \coth \frac{\hbar\omega_1}{2k_B T_1} \right), \tag{3.10}$$

where we assumed that the amplified system noise is the same for both the ON and OFF case. The device output variance is then given by

$$\langle \hat{x}_1^2 \rangle = \frac{\langle \hat{X}_1^2 \rangle_{ON} - \langle \hat{X}_1^2 \rangle_{OFF}}{G_1} + \coth \frac{\hbar\omega_1}{2k_B T_1}.$$

Discrete mode approximation

Similar to many entanglement measures, the device output variance here is derived for discrete modes, which are an approximation. To make a connection to the acquired data, we think of our continuous modes as being made up of a density of discrete modes. Thus, we can associate the discrete variance with the continuous variance per unit bandwidth

(spectral density) by relating the discrete mode operators to the signal spectral density, i.e. $\langle \hat{X}_1^2 \rangle \approx S_{XX}(\omega)$. Then we obtain the overall conversion equation:

$$\langle \hat{x}_1^2 \rangle = \frac{4\left(\langle \hat{I}_1^2(0,t)\rangle_{ON} - \langle \hat{I}_1^2(0,t)\rangle_{OFF}\right)}{G_1 \hbar\omega_1 Z_0 BW} + \coth\frac{\hbar\omega_1}{2k_B T_1} \tag{3.11}$$

Note that the coth() term represents the input quantum noise that must be added back to the measured noise. This is because, when measuring the OFF power, the input quantum noise is also measured. If this is not properly accounted for, then we may erroneously infer entanglement when it does not exist. Thus, it is important to characterize the temperature of the input field properly. The other quadrature variances can be computed similarly.

3.4.5 Device output covariance

Similar to the variance conversion, the covariance from the device can be computed as a scaling of the acquired data at room temperature. Consider the room temperature covariance $\langle \hat{X}_1 \hat{X}_2 \rangle$ of mode 1 and 2:

$$\begin{aligned}
\langle \hat{X}_1 \hat{X}_2 \rangle &= \left\langle \left(\hat{A}_1 + \hat{A}_1^\dagger\right)\left(\hat{A}_2 + \hat{A}_2^\dagger\right)\right\rangle \\
&= \left\langle \hat{A}_1\hat{A}_2 + \hat{A}_1\hat{A}_2^\dagger + \hat{A}_1^\dagger\hat{A}_2 + \hat{A}_1^\dagger\hat{A}_2^\dagger \right\rangle \\
&= \sqrt{G_1 G_1}\langle \hat{x}_1\hat{x}_2\rangle + \sqrt{G_1(G_2-1)}\cancelto{0}{\langle \hat{x}_1 \hat{x}_{HEMT,1}\rangle} \\
&\quad + \sqrt{G_2(G_1-1)}\cancelto{0}{\langle \hat{x}_{HEMT,1}\hat{x}_2\rangle} + \sqrt{(G_1-1)(G_2-1)}\cancelto{0}{\langle \hat{x}_{HEMT,1}\hat{x}_{HEMT,2}\rangle} \\
&= \sqrt{G_1 G_1}\langle \hat{x}_1\hat{x}_2\rangle
\end{aligned}$$

where we assume that the input quantum noise and HEMT noise are uncorrelated. Furthermore, we assume (and measure) that the amplifier noise at different frequency is not correlated either. Thus, only the first term remains,

$$\langle \hat{x}_1\hat{x}_2\rangle = \frac{\langle \hat{X}_1\hat{X}_2\rangle}{\sqrt{G_1 G_2}}$$

Applying the same discrete mode approximation, we obtain the conversion for covariance:

$$\langle \hat{x}_1\hat{x}_2\rangle = \frac{4\langle \hat{I}_1(0,t)\hat{I}_2(0,t)\rangle}{\sqrt{G_1 G_2 \omega_1\omega_2 Z_{0,1}Z_{0,2}}\hbar BW} \tag{3.12}$$

3.5 Other measurement considerations

3.5.1 ON-OFF chopped measurement

From section 3.4.4, we need to perform a pump ON-OFF subtraction for the RT-measured signals in order to remove the amplifier noise and obtain the device output variance. The signal power in our system is measured by the number of photons per second per Hertz (photon/s/Hz). With our HEMT amplifier, the noise power spectral density ranges from $25 - 40$ photon/s/Hz over the $4 - 8$ GHz measurement bandwidth. Thus, the noise power is rather large compared to the $1 - 5$ photon/s/Hz of the device output signal power. Unfortunately, the noise power is not stable and can drift a few percentages over a long measurement. As a result, subtracting the average of a long acquisition of ON signal by another long acquisition of OFF signal can result in a large systematic error in the device output variance.

One solution here is to perform repeated ON-OFF chopped measurements each within a short period of time, in order that the OFF signal be subtracted from the ON signal before a significant drift in system noise has occurred. An accurate ON-OFF signal difference can then be obtained by averaging over each of the measured differences. This approach is employed for most of the data acquisition considered in this thesis.

3.5.2 Digitizers triggering for correlation measurement

In order to maximize the measurable correlation between two or more signals, the sampling of the digitizers must be highly synchronized. In practice, this is done by making sure that, firstly, the digitizers are triggered by a single external trigger signal so that they start to acquire data at the same time. Secondly, the sampling clocks of the digitizers should have zero relative phase. Establishing a relative phase at a low sampling frequency will lead to a computation of correlation between different time with the two sets of data.

The former phase can easily be achieved by ensuring that the two digitizers are always armed before a software trigger signal has been sent through a star trigger. The second requirement can be solved by having all the digitizers use the same digital sampling clock. In case multiple digitizers are used, the phase of the sampling clocks should be individually adjusted until all the clocks are in phase. For example, with Aeroflex 3036, the phase adjustment can be done by temporarily increasing and decreasing the sampling frequency of the digitizer in order to create the required phase shift.

Chapter 4

Two-photon parametric processes

Two-photon parametric interactions have a long history in experiments. Their quantum mechanical properties were first studied with optical systems in 1980s, where SPDC processes were used to generate photon pairs [30, 31] and have since become an important nonclassical light source. With the advancement in circuit QED, similar experiments in the microwave regime began to prevail around 2010 and have since come a long way. Ground-breaking experiments include the generation of two-mode squeezed signals [7] corresponding to continuous variable (CV) entanglement, and also the parametric coherent coupling between two signals [8]. Later, it was realized that by combining two parametric processes it was possible to extend the two-mode entanglement to three modes and beyond, generating what is known as multipartite entanglement [32, 33].

We will explore the properties of two-photon parametric processes in this chapter with experimental results. In the first section we lay out the theory for TMDC which generate entanglement. Then, we explore the theoretical predictions with experimental data and verify the entanglement in our output signal. Finally, we consider the experimental generation of tripartite entanglement and perform different verification on the results.

4.1 Two-mode downconversion - Theory

4.1.1 Output operators of two-mode downconversion

As discussed in section 2.2.2, the TMDC to two frequency modes 1 and 2 is given by

$$\hat{H}_{TMDC} = \hbar g \left(\hat{a}_1 \hat{a}_2 e^{i\theta_p} + \hat{a}_1^\dagger \hat{a}_2^\dagger e^{-i\theta_p} \right). \tag{4.1}$$

The operators for the output modes $\hat{a}_k(t)$ can be evaluated by solving the HEM, i.e. $\dot{\hat{a}}_k(t) = \frac{1}{i\hbar}\left[\hat{a}_k(t), \hat{H}_{TMDC}\right]$. Since $\hat{H}_{TMDC}$ is often applied for a fixed time t, we characterize the degree of squeezing through the squeezing parameter $r = gt$. From Eq.(4.1), we can express the output $\hat{a}_k(r)$ for TMDC in terms of the input vacuum state operator $\hat{a}_k(0)$ as:

mode 1

$$\begin{aligned} \hat{a}_1(r) &= \hat{a}_1(0)\cosh r - i\hat{a}_2^\dagger(0)e^{i\theta}\sinh r \\ \hat{a}_1^\dagger(r) &= \hat{a}_1^\dagger(0)\cosh r + i\hat{a}_2(0)e^{-i\theta}\sinh r \end{aligned} \tag{4.2}$$

mode 2

$$\begin{aligned} \hat{a}_2(r) &= \hat{a}_2(0)\cosh r - i\hat{a}_1^\dagger(0)e^{i\theta}\sinh r \\ \hat{a}_2^\dagger(r) &= \hat{a}_2^\dagger(0)\cosh r + i\hat{a}_1(0)e^{-i\theta}\sinh r \end{aligned} \tag{4.3}$$

As a convention, the two output modes are often called signal and idler.

4.1.2 Continuous-variable correlation between two modes

Each frequency mode in a cavity can be approximately understood as an independent harmonic oscillator. The quadrature terms, usually noted as the position x and the momentum p of the oscillator, or by the I and Q microwave convention, respectively, refer to the real and imaginary part of the amplitude of the frequency mode. In this chapter, they are defined as $\hat{x} = \left(\hat{a} + \hat{a}^\dagger\right)$ and $\hat{p} = -i\left(\hat{a} - \hat{a}^\dagger\right)$. Similar to the bosonic operators above, the quadrature operators can evolve with TMDC. For simplicity, in the following section we have chosen a pump phase $\theta_p = \pi/2$. Thus, the quadrature operators are

$$\begin{aligned} \hat{x}_1(r) &= \hat{x}_1(0)\cosh r + \hat{x}_2(0)\sinh r \\ \hat{p}_1(r) &= \hat{p}_1(0)\cosh r - \hat{p}_2(0)\sinh r \end{aligned} \tag{4.4}$$

$$\begin{aligned} \hat{x}_2(r) &= \hat{x}_2(0)\cosh r + \hat{x}_1(0)\sinh r \\ \hat{p}_2(r) &= \hat{p}_2(0)\cosh r - \hat{p}_1(0)\sinh r \end{aligned} \tag{4.5}$$

With the above expressions, by computing the covariance $\langle \hat{x}_1 \hat{x}_2 \rangle$ and $\langle \hat{p}_1 \hat{p}_2 \rangle$ we can see that the correlation structure takes the form $\langle \hat{x}_1 \hat{x}_2 \rangle = -\langle \hat{p}_1 \hat{p}_2 \rangle$ in the case of TMDC.

4.1.3 Connection between correlation and entanglement

Entanglement can be roughly related to the uncertainty in the relative position and total momentum of two objects [34]. These can be expressed as the variance of the combined variables $x_1 - x_2$ and $p_1 + p_2$ [35]. In separable systems these variances will not go below a certain classical bound.

With harmonic oscillators, the analogy is that entanglement is related to the uncertainty of the relative quadrature amplitudes between two modes. Thus, we can study how the uncertainty changes as two thermal vacuum states evolve under the TMDC Hamiltonian. For instance, using Eq (4.4) and (4.5), we can observe a drop in the variance of the combined quadratures $\hat{x}_1 - \hat{x}_2$ and $\hat{p}_1 + \hat{p}_2$ with increasing squeezing, r. For $\hat{x}_1 - \hat{x}_2$,

$$\begin{aligned}
\mathrm{Var}\left(\hat{x}_1(r) - \hat{x}_2(r)\right) &= \left\langle \left(\hat{x}_1(r) - \hat{x}_2(r)\right)^2 \right\rangle - \left\langle \left(\hat{x}_1(r) - \hat{x}_2(r)\right) \right\rangle^2 \\
&= \langle \hat{x}_1^2(r) \rangle + \langle \hat{x}_2^2(r) \rangle - \langle \hat{x}_1(r)\hat{x}_2(r) \rangle - \langle \hat{x}_2(r)\hat{x}_1(r) \rangle \\
&\quad \cancelto{0}{-\langle \hat{x}_1(r) \rangle^2} \cancelto{0}{- \langle \hat{x}_2(r) \rangle^2} + \cancelto{0}{2\langle \hat{x}_1(r) \rangle \langle \hat{x}_2(r) \rangle} \\
&\quad \cancelto{0}{-\langle \hat{x}_1(r) \rangle^2} \\
&= \langle \hat{x}_1^2(r) \rangle + \langle \hat{x}_2^2(r) \rangle - \langle \hat{x}_1(r)\hat{x}_2(r) \rangle - \langle \hat{x}_2(r)\hat{x}_1(r) \rangle \\
&= \left(\langle \hat{x}_1^2(0) \rangle + \langle \hat{x}_2^2(0) \rangle \right) \left(\cosh r - \sinh r \right)^2 \\
&= \left(\langle \hat{x}_1^2(0) \rangle + \langle \hat{x}_2^2(0) \rangle \right) e^{-2r}.
\end{aligned} \tag{4.6}$$

Similarly, for $\hat{p}_1 + \hat{p}_2$,

$$\begin{aligned}
\mathrm{Var}\left(\hat{p}_1(r) + \hat{p}_2(r)\right) &= \left\langle \left(\hat{p}_1(r) + \hat{p}_2(r)\right)^2 \right\rangle - \left\langle \left(\hat{p}_1(r) + \hat{p}_2(r)\right) \right\rangle^2 \\
&= \langle \hat{p}_1^2(r) \rangle + \langle \hat{p}_2^2(r) \rangle + \langle \hat{p}_1(r)\hat{p}_2(r) \rangle + \langle \hat{p}_2(r)\hat{p}_1(r) \rangle \\
&= \left(\langle \hat{p}_1^2(0) \rangle + \langle \hat{p}_2^2(0) \rangle \right) \left(\cosh r - \sinh r \right)^2 \\
&= \left(\langle \hat{p}_1^2(0) \rangle + \langle \hat{p}_2^2(0) \rangle \right) e^{-2r}.
\end{aligned} \tag{4.7}$$

Here, we assume that the input is a thermal vacuum state such that the first moments are zero. As the variances drop below that of two cold vacuum states, the modes become entangled. For maximally entangled continuous variable states, their variances reduce to zero.

To understand the effect of a thermal input state with finite temperature, we simply

substitute the input state variances with thermal photon distributions, e.g.

$$\begin{aligned}\mathrm{Var}\left(\hat{x}_1(r)-\hat{x}_2(r)\right) &= \left(\langle\hat{x}_1^2(0)\rangle_{Thermal}+\langle\hat{x}_2^2(0)\rangle_{Thermal}\right)e^{-2r}\\ &= \left(\coth\frac{\hbar\omega_1}{2k_BT_1}+\coth\frac{\hbar\omega_2}{2k_BT_2}\right)e^{-2r}.\end{aligned}$$

With a high temperature thermal state and a small amount of squeezing, the output variances can be higher than that of a cold vacuum state and no entanglement is present. This motivates the need for a proper thermalization of the cavity in order to generate entanglement.

The above discussion was intended to give a simple physical picture of entanglement in a CV system. In the next section, we will outline a general entanglement verification method for Gaussian CV systems.

4.1.4 Entanglement verification by PPT criterion

A more sophisticated method for continuous variable entanglement verification is the positive-partial transpose criterion (PPT) [36] based on the covariance matrix of the signals. This method works for testing Gaussian output states which contain pair-wise correlation. It is thus suitable for the TMDC states. In a later section we will also apply this method to test for tripartite Gaussian entangled states.

For Gaussian states generated by quadratic Hamiltonians, such as the TMDC Hamiltonian, the output state is fully characterized by the $2N\times 2N$ covariance matrix $\mathbf{V}$ of the x and p voltage quadratures of the propagating modes. We collect the $N-$mode quadrature operator terms into a vector operator $\hat{\mathbf{K}}=(\hat{x}_1,\hat{p}_1,\hat{x}_2,\hat{p}_2,\ldots,\hat{x}_N,\hat{p}_N)^T$, and we define the elements in $\mathbf{V}$ as $V_{ij}=\left\langle\hat{\mathbf{K}}_i\hat{\mathbf{K}}_j+\hat{\mathbf{K}}_j\hat{\mathbf{K}}_i\right\rangle/2$, assuming the modes are mean-zero.

Physicality of covariance matrix

The first step in the PPT test is to verify if the measured covariance matrices are physical. To be physical in a classical sense, $\mathbf{V}$ needs to be real, symmetric and positive semidefinite. To be physical in the quantum sense, $\mathbf{V}$ must also obey the Heisenberg uncertainty principle. The uncertainty principle can be expressed in terms of the symplectic eigenvalues [37], ν_i of $\mathbf{V}$, which are found by diagonalization of $\mathbf{V}$ through a canonical transformation of $\hat{\mathbf{K}}$.

We can write the commutation relation as $\left[\hat{\mathbf{K}}_i, \hat{\mathbf{K}}_j\right] = 2i\Omega_{ij}$, where $\mathbf{\Omega} = \mathbf{I}_N \otimes \begin{pmatrix} 0 & 1 \\ -1 & 0 \end{pmatrix}$. As an example, for a two-mode state,

$$\mathbf{\Omega} = \begin{pmatrix} 0 & 1 & 0 & 0 \\ -1 & 0 & 0 & 0 \\ 0 & 0 & 0 & 1 \\ 0 & 0 & -1 & 0 \end{pmatrix}. \tag{4.8}$$

With this definition, the symplectic eigenvalue can be calculated as the absolute values of the regular eigenvalues of $i\mathbf{\Omega}\mathbf{V}$. Using these definitions, the uncertainty principle requires $\nu_i \geq 1$ for all i.

Separability of the PPT covariance matrix

If $\mathbf{V}$ of an output state passes the physicality tests, we can then proceed to test the state for separability using the PPT criterion, as depicted by Fig. 4.1.

Figure 4.1: An illustration of the positive partial transpose test. Beginning with the original covariance matrix $\mathbf{V}$, a partial time-reversal is applied to one of the partitions, e.g. mode i of the multimode system. Then the partial time-reversed output state is checked again if it still obeys the uncertainty relations as a physicality test. If the output state is still physical, it means the subsystems in the original state, represented by $\mathbf{V}$, were not entangled. If the partial time-reversed matrix failed the test, it implies that the subsystems described in $\mathbf{V}$ were entangled.

The principle behind the PPT criterion is that if we time-reverse a subsystem (a partition) of a multimode entangled state, then the resulting total state will be unphysical. Thus, testing for entanglement then corresponds to confirmation that the covariance matrix of the partially time-reversed state $\tilde{\mathbf{V}}$ is unphysical[1]. In our covariance matrix description,

[1]The PPT test was originally applied to test a density matrix, where the test of physicality is to check if the matrix is positive semidefinite. The partial transpose of a density matrix corresponds to a partial time-reversal on the subsystems.

partial time-reversal corresponds to changing the sign of a subset of the p quadratures. For instance, for a 1-mode—(N-1)-mode bipartition of the total state which attempts to separate mode i from other modes, the corresponding transformation is $\mathbf{V} \to \tilde{\mathbf{V}} = \mathbf{\Lambda_i}^T \mathbf{V} \mathbf{\Lambda_i}$, where $\mathbf{\Lambda_i} = \mathrm{diag}\left(a_1, a_2, \ldots, a_{2i}, \ldots, a_{2N}\right)$ is a diagonal matrix with all $a = 1$ except $a_{2i} = -1$. Thus, we have the entanglement condition as

$$\tilde{\nu}_{min} \equiv \nu_{min}\left(\tilde{\mathbf{V}}\right) < 1. \tag{4.9}$$

We note that a commonly quoted measure of entanglement in continuous variable system is the logarithmic negativity, which is a function of ν_{min}, specifically,

$$\mathcal{N} \equiv \max\left[0, -\ln\left(\tilde{\nu}_{min}\right)\right] > 0.$$

General entanglement bound for two-mode states

For a two-mode state, the entanglement bound from the PPT test can be expressed as below. By defining the following variables using the variance and covariance of the two modes,

$$\begin{aligned} P_1 &= \left(\left\langle \hat{x}_1^2 \right\rangle + \left\langle \hat{p}_1^2 \right\rangle\right)/2 \\ P_2 &= \left(\left\langle \hat{x}_2^2 \right\rangle + \left\langle \hat{p}_2^2 \right\rangle\right)/2 \\ P &= \left(P_1 + P_2\right)/2 \\ \delta P &= \left(P_1 - P_2\right)/2 \\ C &= \left(\left\langle \hat{x}_1 \hat{x}_2 \right\rangle - \left\langle \hat{p}_1 \hat{p}_2 \right\rangle\right)/2 \end{aligned}$$

we can find a simple expression for the entanglement condition defined by $\tilde{\nu}_{min}$, where it requires

$$\tilde{\nu}_{min} = P - \sqrt{\delta P^2 + C^2} < 1. \tag{4.10}$$

4.2 Two-mode downconversion - Experiment

4.2.1 Measurement setup

From the fridge AC circuit described in Fig. 3.2, the output signal at room temperature is further routed by the circuit described in Fig. 4.2.

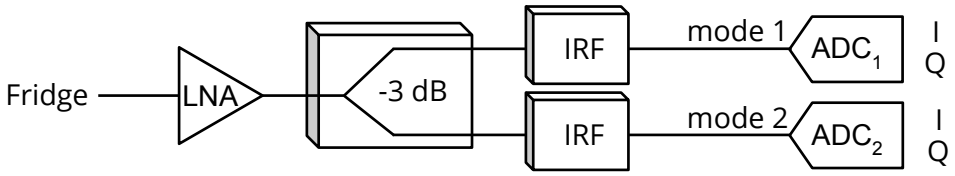

Figure 4.2: The room temperature signal routing for the two-mode downconversion measurement. The output signal from the fridge is first amplified by a chain of two low-noise amplifiers. After the amplifiers, the signal is split into two paths, where each goes through an image-rejection filter and is then digitized. The digitizers each gives the time-series I and Q quadratures data, centered at the frequency modes.

Measurement scheme

The quadrature signals are acquired using the ON-OFF chopped measurement with the ON acquisition and OFF acquisition each taking one second. Within the digitizers, an analogue heterodyne mixing followed by direct digital downconversion of the IF signal produces the sampled I and Q quadratures used in the correlation measurements. The incoming signal is first downconverted to an IF which is sampled at 250 MHz, then, the FPGA gives I and Q samples at a maximum rate of 200 MS/s. We then choose to digitally downsample the I and Q samples to 1 MHz which defines the bandwidth (BW) for the signal conversion detailed in section 3.4. We note that the choice of BW can be set to as high as 200 MHz, limited by the FPGA.

In the acquisition, 200 or more triggers worth of data are acquired and averaged to obtain a sufficiently high signal-to-noise ratio for the TMDC measurements. From each trigger we obtain 1 million samples of the I and Q quadratures from each digitizer. The I and Q samples are internally calibrated so we can convert the input signals into powers. Following the TMDC output measurement, the system is immediately calibrated for the system gain and input noise temperature using the SNTJ (see section 3.3).

The variance and covariance terms between the two modes are then calculated, followed by a conversion using the system calibration (see section 3.4.4) to give the variance and

covariance referred to the device output. We then form the N-mode covariance matrix:

$$\mathbf{V}_{1,\ldots,N} = \begin{array}{c} \\ x_1 \\ p_1 \\ \vdots \\ \vdots \\ x_N \\ p_N \end{array} \begin{array}{c} \begin{array}{cccccc} x_1 & p_1 & \ldots & \ldots & x_N & p_N \end{array} \\ \begin{pmatrix} \langle x_1 x_1 \rangle & \langle x_1 p_1 \rangle & \ldots & \ldots & \langle x_1 x_N \rangle & \langle x_1 p_N \rangle \\ \langle p_1 x_1 \rangle & \langle p_1 p_1 \rangle & \ldots & \ldots & \langle x_1 x_N \rangle & \langle x_1 p_N \rangle \\ \vdots & \vdots & \ddots & & \vdots & \vdots \\ \vdots & \vdots & & \ddots & \vdots & \vdots \\ \langle x_N x_1 \rangle & \langle x_N p_1 \rangle & \ldots & \ldots & \langle x_N x_N \rangle & \langle x_N p_N \rangle \\ \langle p_N x_1 \rangle & \langle p_N p_1 \rangle & \ldots & \ldots & \langle p_N x_N \rangle & \langle p_N p_N \rangle \end{pmatrix} \end{array}. \tag{4.11}$$

With a two-mode covariance matrix $\mathbf{V}_{1,2}$, at least 10 individual terms corresponding to the upper triangle needs to be computed to fully characterize the output.

4.2.2 Selection of effective pump phase

From Eq.(4.1), we observe that there is a degree of freedom in choosing the pump phase. In practice, all the local phases of the digitizer LOs, and the phases picked up by the signals throughout the transmission, including the pump phase, play a role in determining the final, effective phase of TMDC.

To understand the effect of a different pump phase, we take a step back and consider the general form of the correlators, e.g. $\langle \hat{x}_1 \hat{x}_2 \rangle$ and $\langle \hat{x}_1 \hat{p}_2 \rangle$ by including the pump phase. Using Eq. (4.2) and (4.3), we compute the correlators

$$\begin{aligned} \langle \hat{x}_1 \hat{x}_2 \rangle &= -\langle \hat{p}_1 \hat{p}_2 \rangle \\ &= \Big\langle \Big(\hat{a}_1 \cosh r - i\hat{a}_2^\dagger \sinh r e^{i\theta_p} + \hat{a}_1^\dagger \cosh r + i\hat{a}_2 \sinh r e^{-i\theta} \Big) \\ &\qquad \times \Big(\hat{a}_2 \cosh r - i\hat{a}_1^\dagger \sinh r e^{i\theta} + \hat{a}_2^\dagger \cosh r + i\hat{a}_1 \sinh r e^{-i\theta} \Big) \Big\rangle \\ &= 2 \cosh r \sinh r \sin \theta_p, \end{aligned} \tag{4.12}$$

$$\begin{aligned} \langle \hat{x}_1 \hat{p}_2 \rangle &= \langle \hat{p}_1 \hat{x}_2 \rangle \\ &= \Big\langle \Big(\hat{a}_1 \cosh r - i\hat{a}_2^\dagger \sinh r e^{i\theta_p} + \hat{a}_1^\dagger \cosh r + i\hat{a}_2 \sinh r e^{-i\theta_p} \Big) \\ &\qquad \times -i \Big(\hat{a}_2 \cosh r - i\hat{a}_1^\dagger \sinh e^{-\theta_p} - \hat{a}_2^\dagger \cosh r - i\hat{a}_1 \sinh r e^{-i\theta_p} \Big) \Big\rangle \\ &= -2 \cosh r \sinh r \cos \theta_p. \end{aligned} \tag{4.13}$$

The overall covariance is split between the two groups of correlators, $\langle \hat{x}_1 \hat{x}_2 \rangle, \langle \hat{p}_1 \hat{p}_2 \rangle$ and $\langle \hat{x}_1 \hat{p}_2 \rangle, \langle \hat{p}_1 \hat{x}_2 \rangle$. Thus, computing one set alone could underestimate the actual covariance that the state contains. Second, due to the relative negative sign between Eq. (4.12) and (4.13), directly averaging the data taken throughout a long acquisition can wash out the covariances as the relative phases of the pump and LOs drift.

To solve this problem, we can digitally rotate the phase of the data to select an effective θ_p for Eq. (4.12) and Eq. (4.13). With the measured quadrature data, we can rotate one of the modes, e.g. x_1, p_1 into x_1', p_1', using the following expressions,

$$\begin{aligned} x_1' &= x_1 \cos\theta_c - p_1 \sin\theta_c \\ p_1' &= p_1 \cos\theta_c + x_1 \sin\theta_c, \end{aligned} \tag{4.14}$$

where θ_c is the correcting phase. θ_c depends on the amplitude of the four covariances $\langle x_1 x_2 \rangle, \langle x_1 p_2 \rangle, \langle p_1 x_2 \rangle, \langle p_1 p_2 \rangle$. For TMDC it takes the form

$$\theta_c = -\theta_{TMDC} = -\arctan \frac{\langle x_1 p_2 \rangle + \langle p_1 x_2 \rangle}{\langle x_1 x_2 \rangle - \langle p_1 p_2 \rangle}. \tag{4.15}$$

With the above rotation, the covariance will be contained only by the correlators $\langle x_1' x_2 \rangle$ and $\langle p_1' p_2 \rangle$, and the other correlators $\langle x_1' p_2 \rangle$ and $\langle p_1' x_2 \rangle$ will become zero. This is essentially a diagonalization of the cross-correlation sector of the covariance matrix Eq. (4.11) where we are placing the matrix into a standard form (for two modes) [38],

$$\begin{array}{c} \\ x_1 \\ p_1 \\ x_2 \\ p_2 \end{array} \begin{array}{c} \begin{array}{cccc} x_1 & p_1 & x_2 & p_2 \end{array} \\ \begin{pmatrix} P_1 & 0 & C & 0 \\ 0 & P_1 & 0 & -C \\ C & 0 & P_2 & 0 \\ 0 & -C & 0 & P_2 \end{pmatrix} \end{array}. \tag{4.16}$$

We note that this phase rotation cannot change the symplectic eigenvalues of the matrix.

Trigger jitter

In measuring covariance, one additional problem is trigger jitter between the digitizers. Trigger jitter means that one digitizer could start to collect time-series data one time bin (= one microsecond in our measurement) before or after the other digitizer. As a result, in some triggers we need to shift the time series data of one digitizer when computing the covariance. This can be seen by plotting the covariance of the signal against different time delay between the two sets of time-series data (see Fig. 4.3).

4.2.3 Error analysis

Here we analyse the acquired data to justify that our ON-OFF chopped measurement was able to remove the drifting system noise. It also helps us to put error bars on our measurements. With the measured quadrature voltages I and Q being Gaussian random variables with variance σ^2 (which is a very good assumption), the square quadratures I^2, Q^2 are described by a χ-square distribution with one degree of freedom. If we define $y = I^2, Q^2$ then we have

$$P(y) = \frac{1}{\sqrt{2\pi y\sigma^2}} e^{-y/2\sigma^2}. \tag{4.17}$$

We then find that the expected value of I^2, Q^2 is

$$E(y) = \int_0^\infty dy \frac{y}{\sqrt{2\pi y\sigma^2}} e^{-y/2\sigma^2} = \sigma^2. \tag{4.18}$$

The variance of the square quadratures can then be calculated as $\mathrm{Var}(y) = E(y^2) - E(y)^2$. We find

$$E(y^2) = \int_0^\infty \frac{y^2}{\sqrt{2\pi y\sigma^2}} e^{-y/2\sigma^2} = 3\sigma^4. \tag{4.19}$$

This yields finally

$$\mathrm{Var}(y) = \mathrm{Var}(I^2) = \mathrm{Var}(Q^2) = 2\sigma^4. \tag{4.20}$$

If we then think of averaging a number of measurements, N, of I_i^2, Q_i^2, we get, e.g., the estimator

$$\bar{I}^2 = \frac{1}{N} \sum I_i^2. \tag{4.21}$$

The variance of this estimator is then

$$\mathrm{Var}(\bar{I}^2) = \frac{1}{N^2} \sum \mathrm{Var}(I^2) = \frac{1}{N} \mathrm{Var}(I^2) = \frac{2}{N} \sigma^4. \tag{4.22}$$

which is the theoretical prediction for the uncertainty in our variance and covariance measurements.

To confirm that we successfully remove the drift of our system and that our averaging is effective, we can compare this theoretical prediction to the measured variance (of the variance) as a function of N. Without performing the ON-OFF subtraction, we find that the experimental values agree well with the theoretical predictions up to $N \sim 10^6$. Beyond this point, the raw ON or OFF values saturate, indicating drift in the system. Including the subtraction, we only start to see saturation at the level of $N \sim 10^9$.

In the following sections, we calculate the error bars for the measurements. We start by analysing the propagation of error in the variance and covariance terms of the covariance matrices.

Error in variance at the device output

A number of the scale parameters in (3.11) and (3.12) have their own uncertainties, which will contribute to the final uncertainties in $\mathbf{V}$. Starting from the uncertainties of the raw variance and covariances, described above, standard propagation-of-error formulas were then used to calculate the uncertainties of the scaled values at the device output. The error calculation was performed for each element of $\mathbf{V}$. These error terms can be gathered in the form of an error matrix, $\mathbf{V}_\sigma$, which has the same dimension as $\mathbf{V}$. As described below, these error matrices were finally used to calculate the error in the various entanglement measurements.

Considering (3.11), for mode i, in the first term we have:

- a constant factor that contributes no variance
$$K = \frac{4}{Z_0 \hbar \omega_i BW},$$
- the error of the ON-OFF power divided by the gain
$$\sigma_{quotient} = \sqrt{\left(\frac{\sqrt{\sigma^2_{I_i,ON} + \sigma^2_{I_i,OFF}}}{\langle \hat{I}_i^2 \rangle_{ON} - \langle \hat{I}_i^2 \rangle_{OFF}}\right)^2 + \left(\frac{\sigma_{G_i}}{G_i}\right)^2} \times \frac{\left(\langle \hat{I}_i^2 \rangle_{ON} - \langle \hat{I}_i^2 \rangle_{OFF}\right)}{G_i},$$
- giving the total error in the first term as $\sigma_{1st} = K \times \sigma_{quotient}$.

For the second term, we have:

- a constant factor
$$K' = \frac{\hbar \omega}{2k_B},$$
- the derivative of the coth term
$$\frac{d(\coth(K'x))}{dx} = K' \left(1 - \coth^2(K'x)\right),$$

- giving the error in the second term $\sigma_{2nd} = K' \times \left(1 - \coth^2\left(\frac{\hbar\omega}{2k_B T_i}\right)\right) \times \sigma_{T_i}$.

Thus, the total error in the calculated device output variance equals

$$\sigma_{mm} = \sqrt{\sigma_{1st}^2 + \sigma_{2nd}^2},$$

which will form the diagonal of the error matrix $\mathbf{V}_\sigma$.

Error in covariance at the device output

Considering (3.12), for mode i and j, we have:

- a constant factor

$$K = \frac{4}{\hbar\sqrt{\omega_i \omega_j Z_{0,i} Z_{0,j}} BW},$$

- the error in numerator

$$\sigma_{I_i I_j} = \text{measured error in } \langle \hat{I}_i \hat{I}_j \rangle,$$

- and the error in the denominator

$$\sigma_{\sqrt{G_i G_j}} = 0.5 \times \sqrt{\left(\frac{\sigma_{G_i}}{G_i}\right)^2 + \left(\frac{\sigma_{G_j}}{G_j}\right)^2} \times \sqrt{G_i G_j}$$

giving the total error in the calculated device output covariance

$$\sigma_{mn} = K \times \sqrt{\left(\frac{\sigma_{I_i I_j}}{\langle \hat{I}_i \hat{I}_j \rangle}\right)^2 + \left(\frac{\sigma_{\sqrt{G_A G_B}}}{\sqrt{G_A G_B}}\right)^2} \times \frac{\langle \hat{I}_i \hat{I}_j \rangle}{\sqrt{G_i G_j}},$$

which corresponds to the off-diagonal terms in the error matrices.

We can then form the error matrices in the same way as the covariance matrices

$$\mathbf{V}_\sigma = \begin{array}{c} \\ x_1 \\ p_1 \\ \vdots \\ \vdots \\ x_N \\ p_N \end{array} \begin{array}{c} \begin{array}{cccccc} x_1 & p_1 & \dots & \dots & x_N & p_N \end{array} \\ \begin{pmatrix} \sigma_{\langle x_1 x_1 \rangle} & \sigma_{\langle x_1 p_1 \rangle} & \dots & \dots & \sigma_{\langle x_1 x_N \rangle} & \sigma_{\langle x_1 p_N \rangle} \\ \sigma_{\langle p_1 x_1 \rangle} & \sigma_{\langle p_1 p_1 \rangle} & \dots & \dots & \sigma_{\langle x_1 x_N \rangle} & \sigma_{\langle x_1 p_N \rangle} \\ \vdots & \vdots & \ddots & & \vdots & \vdots \\ \vdots & \vdots & & \ddots & \vdots & \vdots \\ \sigma_{\langle x_N x_1 \rangle} & \sigma_{\langle x_N p_1 \rangle} & \dots & \dots & \sigma_{\langle x_N x_N \rangle} & \sigma_{\langle x_N p_N \rangle} \\ \sigma_{\langle p_N x_1 \rangle} & \sigma_{\langle p_N p_1 \rangle} & \dots & \dots & \sigma_{\langle p_N x_N \rangle} & \sigma_{\langle p_N p_N \rangle} \end{pmatrix} \end{array}.$$

Error analysis for two-mode entanglement bound

To estimate the error in $\tilde{\nu}$ (Eq. (4.10)), we consider the following error propagation:

- the error in P_i

$$\sigma_{P_i} = \frac{1}{2}\sqrt{\sigma^2_{\langle x_i^2 \rangle} + \sigma^2_{\langle p_i^2 \rangle}},$$

- the error in P and δP

$$\sigma_{P/\delta P} = \frac{1}{2}\sqrt{\sigma^2_{P_1} + \sigma^2_{P_2}},$$

- and the error in C

$$\sigma_C = \frac{1}{2}\sqrt{\sigma^2_{\langle x_1 x_2 \rangle} + \sigma^2_{\langle p_1 p_2 \rangle}}.$$

- giving the error in the second term of (4.10) as

$$\sigma_{2nd} = \frac{\sqrt{\sigma^2_{\delta P}\delta P^2 + \sigma^2_C C^2}}{2\sqrt{\delta P^2 + C^2}}$$

- and the total error in $\tilde{\nu}$ as

$$\sigma_{\tilde{\nu}} = \sqrt{\sigma^2_P + \sigma^2_{2nd}}.$$

4.2.4 Results

With the measurement scheme and data analysis method for TMDC output introduced, we can now proceed to compute the covariance. As a first step of the measurement, we measure the covariance between the I,Q quadratures at room temperature. In the measurement of TMDC, we considered the modes at 4.204 GHz and 6.155 GHz. The pump frequency is simply the sum at 10.359 GHz. A range of pump power was considered in order to study how the output varies with the pump strength.

Correlation in two-mode downconversion

Due to the possible trigger jitter and other possible causes of asynchronization in signal acquisition, it is necessary to compute the covariance over a range of time delays τ between two sets of I,Q data, e.g. $\langle I_1(t)I_2(t+\tau)\rangle$. This can be computed digitally by shifting the data sample-wise when calculating the covariance. In the measurements presented here, the sample period is 1 μs, corresponding to the inverse sampling frequency. The result is shown in Fig. 4.3. We digitally rotated the data according to section 4.2.2 to maximize the covariance in $\langle I_1 I_2\rangle$ and $\langle Q_1 Q_2\rangle$. We can clearly see the TMDC correlation structure where $\langle I_1 I_2\rangle = -\langle Q_1 Q_2\rangle$. Due to the rotation, the other two correlators $\langle I_1 Q_2\rangle$ and $\langle Q_1 I_2\rangle$ become zero.

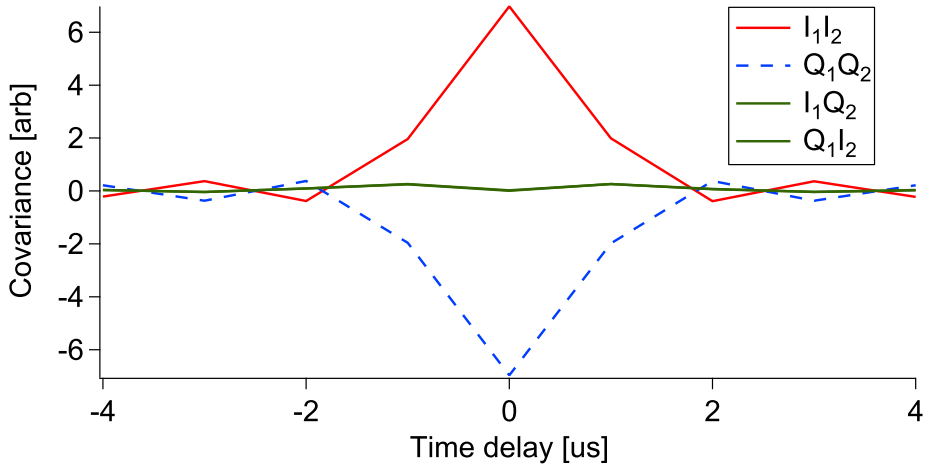

Figure 4.3: Two-mode covariances in a two-mode downconversion. The measured data is digitally rotated to maximize the covariance in $\langle I_1 I_2 \rangle$ and $\langle Q_1 Q_2 \rangle$. As expected, we observe $\langle I_1 I_2 \rangle = -\langle Q_1 Q_2 \rangle$.
The shape of the correlation functions with time delay is determined by the bandwidth of the time traces.

Two-mode entanglement in the output signals

Taking the trigger jitter into account, we select the time delay with the maximum covariance and form the following 2×2 covariance matrix $\mathbf{V}_{1,2}$:

$$\mathbf{V}_{1,2} = \begin{pmatrix} 1.51 & 0.00 & 1.03 & 0.00 \\ 0.00 & 1.51 & 0.00 & -1.03 \\ 1.03 & 0.00 & 1.51 & 0.00 \\ 0.00 & -1.03 & 0.00 & 1.52 \end{pmatrix}, \mathbf{V}_{\sigma} = \begin{pmatrix} 0.004 & 0.002 & 0.002 & 0.001 \\ 0.002 & 0.005 & 0.001 & 0.002 \\ 0.002 & 0.001 & 0.003 & 0.002 \\ 0.001 & 0.002 & 0.002 & 0.003 \end{pmatrix}.$$

The minimum eigenvalue of the matrix is $\lambda_{min}(\mathbf{V}_{1,2}) = 0.480 \pm 0.003 > 0$, thus, the matrix represents a physical state in a classical sense. Next, to check if it fulfills the uncertainty principle, we compute its symplectic eigenvalue. We find $\nu_{min} = |\lambda(i\Omega \mathbf{V}_{1,2})|_{min} = 1.104 \pm 0.004 > 1$, the matrix represents a physical state in a quantum sense. Finally, to verify entanglement, we perform the partial time-reversal operation on our state by the transformation $\mathbf{V} \rightarrow \tilde{\mathbf{V}}_{1,2} = \mathbf{\Lambda_2}^T \mathbf{V}_{1,2} \mathbf{\Lambda_2}$. By computing the symplectic eigenvalue we find $\tilde{\nu}_{min} = \left|\lambda\left(i\Omega \tilde{\mathbf{V}}_{1,2}\right)\right|_{min} = 0.481 \pm 0.002 < 1$, meaning that the state is no longer physical. Thus, the state under test is indeed entangled.

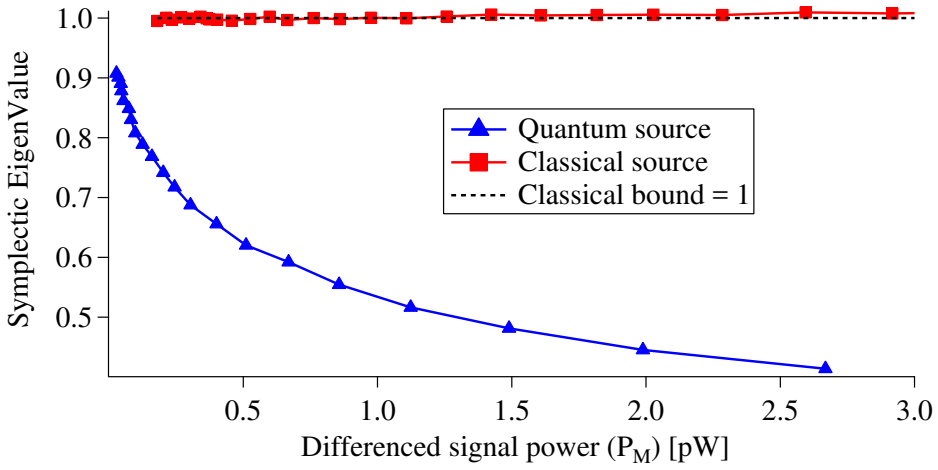

Figure 4.4: A plot of $\tilde{\nu}_{min}$ of TMDC and a classical source. $\tilde{\nu}_{min}$ of the partial time-reversed TMDC signal clear goes below the classical bound, with the amount of entanglement increases with increasing output power as expected, though the increase slows down possibly due to loss and undesired nonlinearity. In a separated measurement, not shown here, a minimum was observed. Conversely, $\tilde{\nu}_{min}$ of the classical signal generated by a classical source (see section 5.2.1) hovers around the classical bound and never drops below it.

We can vary the device output power by varying the pump power. By measuring $\tilde{\nu}_{\min}$ for different output powers, we study the relations between the output power and the amount of entanglement in TMDC. The result is shown in Fig. 4.4. The symplectic eigenvalues of the TMDC signals clearly shows a violation of classical bound, with the violation increasing with higher output signal power produced by stronger pumping. The increase slows down as output power has increased possibly due to the device starting to perform nonideally due to the presence of undesired nonlinearity. We compare this to the results for an ideal classical source (see section 5.2.1) which hover around the bound, but do not violate it.

4.3 Coherent coupling between two modes

In order to extend the Gaussian entanglement to three modes, we will first review another important two-photon parametric interaction given by the SQUID. It is a signal coupling process similar to the beam-splitter coupling in quantum optics. With multiple modes

coupled through a SQUID, it is possible to couple the signal in one mode to another with selective coupling strength. Importantly, the coupling is coherent in a sense that the two coupled signals keep a constant phase relationship determined by the pump signal. This is essential to allow quantum information to transfer from one mode to another. In the following we will call it coherent coupling (CC).

To study the process, a similar analysis to section 2.2.2 can be performed. Now instead of setting the pump frequency to the sum of two modes, coherent coupling requires the pump frequency to be set at the exact difference of the two coupled modes. As a result, it has the following effective interaction Hamiltonian:

$$\hat{H}_{CC} = \hbar g(\hat{a}_1 \hat{a}_2^\dagger e^{i\theta_p} + \hat{a}_1^\dagger \hat{a}_2 e^{-i\theta_p}). \tag{4.23}$$

Solving the associated HEM, we get output operators (by choosing the pump phase to be $\theta_p = -\pi/2$):

mode 1

$$\hat{a}_1(t) = \hat{a}_1(0)\cos r + \hat{a}_2(0)\sin r \tag{4.24}$$

mode 2

$$\hat{a}_2(t) = \hat{a}_2(0)\cos r - \hat{a}_1(0)\sin r \tag{4.25}$$

From the above expressions, we see that the process couples signal between the two modes with a ratio given by the interaction strength r. When an input signal enters from a mode, its power can be split according to the ratio, like a beam splitter. They are associated with $\sin r$ $(\cos r)$ comparing to the $\sinh r$ $(\cosh r)$ carried by the squeezed state outputs. Thus, the coupling represents a photon number conserving process.

Correlation in coherent coupling

Unlike in TMDC, with these output operators, we find, with the above choice of pump phase, that the correlation structure gives $\langle \hat{x}_1 \hat{x}_2 \rangle = \langle \hat{p}_1 \hat{p}_2 \rangle$ without the minus sign found for squeezing, as shown in Fig. 4.5. Also, one can also easily check that the variance of the combined variable $\mathrm{Var}\,(\hat{x}_1(r) - \hat{x}_2(r)) = \mathrm{Var}\,(\hat{x}_1(0) - \hat{x}_2(0))$ remains unchanged with the coupling for any r. This indicates that, starting from thermal vacuum states, the coherent coupling interaction alone does not give rise to two-mode entanglement, in contrast to TMDC where the variance drops with higher squeezing r.

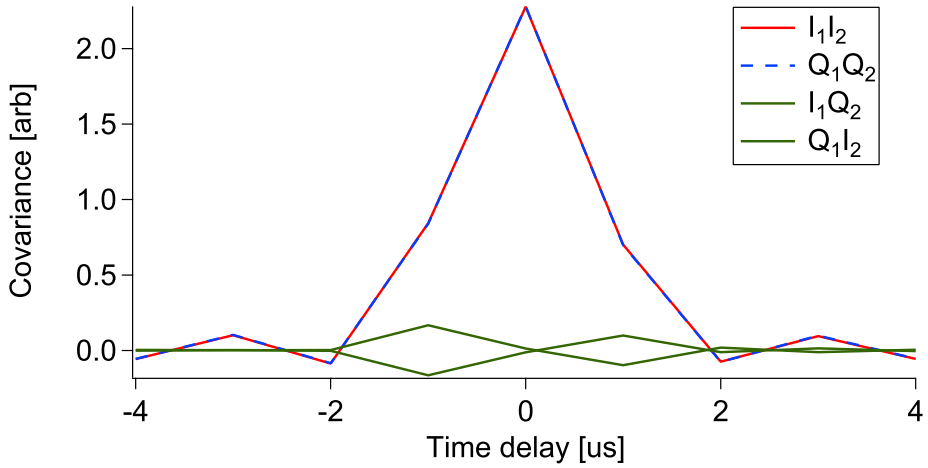

Figure 4.5: Covariances of coherent coupling. The measured data is, again, digitally rotated to maximize the covariance in $\langle I_1 I_2 \rangle$ and $\langle Q_1 Q_2 \rangle$. As expected the observed structure where $\langle I_1 I_2 \rangle = \langle Q_1 Q_2 \rangle$ is different from the TMDC correlation.

4.4 Tripartite entanglement - Theory

Using the above two-photon parametric interactions, we will proceed to study an extension of two-mode entanglement to more modes. By simultaneously performing two two-photon parametric processes, earlier work demonstrated a type of quantum correlation, known as coherence, between three microwave frequencies in a single resonator [39]. Further, the same method can create a tripartite entanglement where three modes together exhibit bipartite inseparability [32], [33]. This can be done experimentally by performing a simultaneous, two-tone pumping.

4.4.1 Simultaneous parametric processes

To study the effect of the simultaneous pumping, we consider the following example of a two-tone pumping scheme. From the previous discussions, we learnt that by pumping at $\omega_{p1} = \omega_1 + \omega_2$ we perform two-mode downconversion to mode 1 and mode 2. Meanwhile, by applying a pump at $\omega_{p2} = \omega_3 - \omega_2$, we coherently couple signals between mode 2 and mode 3. When the two processes are performed simultaneously, we can observe an extra,

indirect effective interaction between mode 1 and 3, which generates a correlation between the two modes.

In order to understand the origin of this extra interaction, we can follow section 2.2.2 to study the effective interaction given by the two-tone pumping. By combining two pump signals at room temperature and sending them to the device, the pump signals superimpose and sum up to give the interaction Hamiltonian

$$\hat{H}_{\mathrm{SQ}} \approx \hbar g_0 \left(\hat{a}_{p_1} + \hat{a}_{p_1}^\dagger + \hat{a}_{p_2} + \hat{a}_{p_2}^\dagger\right) \left(\hat{a}_1 + \hat{a}_1^\dagger + \hat{a}_2 + \hat{a}_2^\dagger + \hat{a}_3 + \hat{a}_3^\dagger\right)^2 . \tag{4.26}$$

Using a similar derivation, we will obtain the effective interaction Hamiltonian which, by definition, only contains both the TMDC and coherent coupling.

$$\hat{H}_{TMDC_{12}+CC_{23}} = \hbar g_1 \left(\hat{a}_1\hat{a}_2 + \hat{a}_1^\dagger\hat{a}_2^\dagger\right) + \hbar g_2 \left(\hat{a}_2\hat{a}_3^\dagger + \hat{a}_2^\dagger\hat{a}_3\right).$$

Consider the time-evolution brought by this Hamiltonian, using the BakerCampbellHausdorff formula,

$$e^{X+Y} = e^X e^Y e^{-\frac{1}{2}[X,Y]} \ldots \tag{4.27}$$

where X and Y respectively correspond to TMDC and coherent coupling, i.e.

$$X = g_1 \left(\hat{a}_1\hat{a}_2 + \hat{a}_1^\dagger\hat{a}_2^\dagger\right)$$
$$Y = g_2 \left(\hat{a}_2^\dagger\hat{a}_3 + \hat{a}_2\hat{a}_3^\dagger\right)$$

The commutator becomes

$$[X, Y] = g_1 g_2 \left(\hat{a}_1\hat{a}_3 - \hat{a}_1^\dagger\hat{a}_3^\dagger\right).$$

which is an effective TMDC interaction between mode 1 and 3. We note that while there are other terms in Eq. (4.27), the series eventually terminates due to the special structure of the operators [32, 33]. We can focus on the effect brought by the commutator.

Now the effect of the simultaneous pumping is more understandable. It is equivalent to not only applying two pumps sequentially, but also followed by a third effective pump that introduces additional correlations. As a result, the simultaneous pumping potentially entangles the two modes. This, therefore, hints at simultaneous parametric processes as a possible way of generating entanglement among multiple frequency modes.

4.4.2 Schemes for generating multipartite entanglement

Motivated by the above, we want to study multipartite entanglement with experiments. As a first step, we consider two schemes for combined pumping in attempts of generating tripartite entanglement.

Coupled-mode

The first scheme, proposed by [32], is the same as the example in the previous section. We will call this a coupled-mode scheme (see Fig. 4.6).

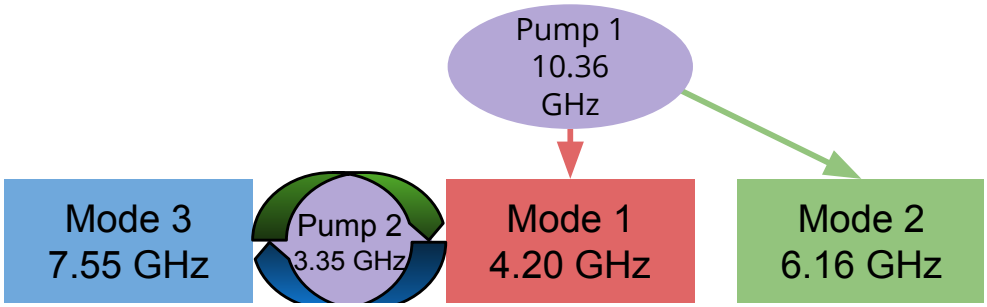

Figure 4.6: Coupled-mode scheme. The purple ellipses represent the two pump signals applied simultaneously to the device for performing two-mode downconversion and coherent coupling. Pump 1 down converts photons into mode 1 & 2, while pump 2 coherently swaps the photons between mode 1 & 3.

In this scheme, pump 1 down converts photons into mode 1 & 2. This will create nonzero correlation in the quadrature terms between the mode 1 & 2. The coherent coupling due to pump 2 will then swap mode 1 & 3. As mode 3 is in the vacuum state, this operation will transfer the downconverted photons from mode 1 to mode 3, effectively sharing the downconverted signal between mode 1 & 3 with a ratio depending on the strength of pump 2. This creates an effective TMDC pumping between mode 2 & 3. There will be output signal from all three modes with nonzero covariance among the modes.

Bisqueezing

The second scheme called bisqueezing in [33] simultaneously applies two downconversion pumps, with one of the modes in common (see figure 4.7).

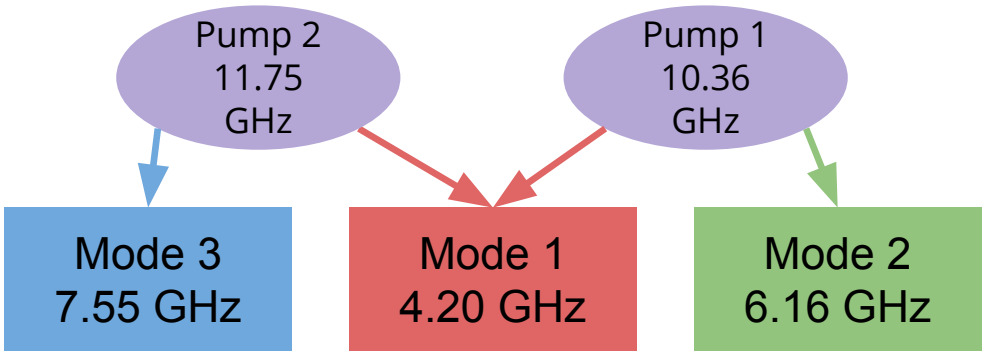

Figure 4.7: Bisqueezing scheme. The purple ellipses represent the two pump signals applied simultaneously to the device. Pump 1 down-converts photons into mode 1 & 2, while pump 2 down-converts photons into mode 1 & 3 at the same time.

These schemes can be understood more intuitively for one will expect entanglement arising naturally from the downconversion to mode 1 & 2, and mode 1 & 3. What was not obvious is, however, while mode 2 never directly interacts with mode 3, a similar covariance structure to a coherently coupled pair $\langle \hat{x}_2 \hat{x}_3 \rangle = \langle \hat{p}_2 \hat{p}_3 \rangle$ can be detected between them. This implies that mode 2 & 3 were coherently coupled in some senses, again, giving rise to a nontrivial tripartite covariance structure which multimode entanglement maybe detected.

A summary of pump frequencies and modes involved in each scheme is shown in Table. 4.1.

	Frequencies [GHz]				
Scheme	Modes			Pumps	
Coupled-mode	4.2039	6.1551	7.5538	10.359	3.3499
Bisqueezing	4.2042	6.1553	7.5545	10.359	11.7587

Table 4.1: Mode and pump frequencies for each scheme. In the coupled-mode (CM) scheme, the first pump frequency is the sum frequency of modes 1 & 2, while the second pump frequency is the difference frequency between modes 1 & 3. In the bisqueezing (BS) scheme, the two pump frequencies are the sum frequencies of modes 1 & 2 and modes 1 & 3.

4.4.3 Tripartite entanglement verification

To verify the tripartite entanglement given by the three-mode output states, we examined two verification procedures.

Full inseparability

The PPT criterion and $\mathcal{N}$ suffice to fully characterize two-mode states, however, as one might expect, classifying entanglement quickly becomes complex with increasing number of modes. For three-mode results, early work [40, 41] suggested we can still classify entanglement based on the PPT criterion by considering the three possible bipartitions of the state, as shown in Fig. 4.8.

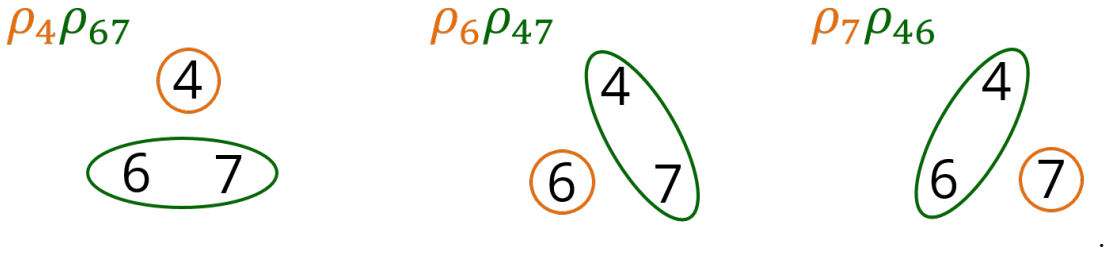

Figure 4.8: All possible bipartitions of a three-mode output state. In our case we therefore have bipartitions 4-67, 6-47 and 7-46.

Recall in the two mode case (see section 4.1.4), the PPT test checks if one mode can be separated from the other. Similarly, in the three mode case, we can apply the PPT test and check if any one mode can be separated from the other two modes, essentially testing if any biparitions in Fig. 4.8 is possible. To perform the test, we simply apply the partial time-reversal on one of the three modes. In terms of the three-mode covariance matrices, similar to the two-mode case, this will render the resultant matrix, e.g. $\mathbf{V}_{4-67}$, unphysical if the three-mode state contains tripartite entanglement.

The early work proposed a "highest" class of "fully inseparable" states, where all bipartitions are entangled, that is, the PPT test indicates inseparability of all three bipartitions. This class can be quantified by the so-called tripartite negativity $\mathcal{N}^{tri} = \left(\mathcal{N}^A\mathcal{N}^B\mathcal{N}^C\right)^{1/3}$, where A, B, C label bipartitions of the states, which is only nonzero for these fully inseparable states [33].

Genuine tripartite entanglement

It was later pointed out that [42, 43, 44], although this test ruled out that any one mode was separable from the whole, it did not rule out that the state being a mixture of states, each of which was separable. That is, there could still exist states of the form $\rho = a\rho_1\rho_{23} + b\rho_2\rho_{13} + c\rho_3\rho_{12}$, where $a + b + c = 1$, which are fully inseparable according to the above definition. It was suggested that the term "genuine" tripartite entanglement be reserved for states that cannot be written as such a convex sum. We note that this distinction between full inseparability and genuine entanglement only exists for mixed states, so understanding the purity of the state under study is important.

[43] derived a set of generalized inequalities to test for genuine tripartite entanglement. In the simplest form, we define linear combinations of our quadratures $u = h_1x_1 + h_2x_2 + h_3x_3$ and $v = g_1p_1 + g_2p_2 + g_3p_3$, where h and g are arbitrary constants to be optimized. We can reduce the optimization space and simplify the bound by putting constraints on the coefficients. We will use the two cases 1) $h_l = g_l = 1, h_m = h_n = h, g_m = g_n = g, hg < 1$ and 2) $h_l = g_l = 1, h_m = -g_n, h_n = -g_m$ both with the search domain $[-1, 1]$, and it was shown that states without genuine entanglement satisfy the inequality

$$S \equiv \Delta u^2 + \Delta v^2 \geq 2. \tag{4.28}$$

Violating this inequality is only a sufficient condition for entanglement. A stricter bound can be found by allowing all of the h and g to be optimized independently. This comes at the cost of having to optimize the inequality in a higher dimensional search space.

4.5 Tripartite entanglement - Experiment

4.5.1 Measurement setup

We perform the measurement on the three-mode output states using two microwave digitizers. While it would be ideal to use three microwave digitizers, a pair-wise acquisition of data can be performed as the output state is Gaussian and, therefore, exhibits only pair-wise correlations. With our simultaneous pumping schemes, the steady-state outputs can be acquired sequentially as three pairs of mode, as pair 1 & 2, pair 2 & 3 and pair 1 & 3.

Signal routing with IRFs

In practice, the use of image-rejection filters requires a more sophisticated RT signal routing, comparing to the TMDC measurement. While we can simply measure a pair of modes and swap the filters, this requires a new system calibration each time it is done. Very often we need to acquire a small amount of test data from each pair of modes in order optimize the configurations, where making such frequent changes is problematic. In our measurement, this is avoided by combining the image-rejection filters using a combination of power splitters and RT microwave switch, as illustrated in Fig. 4.9.

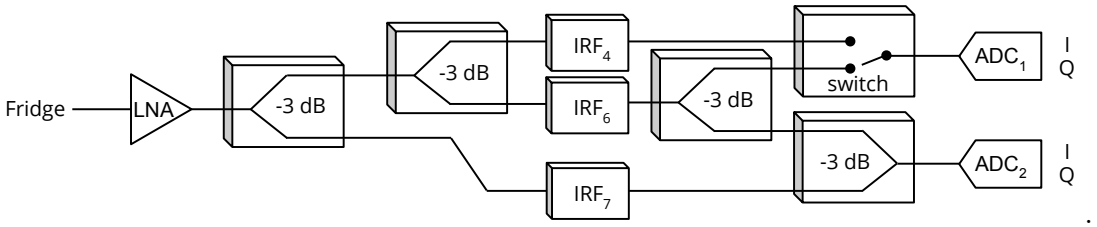

Figure 4.9: A schematic of room temperature signal routing for the pair-wise acquisition of three-mode output states. The circuit combines a microwave switch and power splitters to allow image rejection for all three modes while measured using two microwave digitizers.

In Fig. 4.9, after amplification, the signal is first split into two paths. The lower path goes through the IRF for the mode around 7 GHz, where the upper path is further split and filtered to obtain the modes close to 4 and 6 GHz. When measuring the pairs of 4 & 6 and 4 & 7, the microwave switch connects to the upper path; when measuring the 6 & 7 pair, the switch is toggled to the lower path. Using this circuit, no rewiring is needed apart from electrically toggling the switch, allowing a more flexible measurement and configuration optimization.

Measurement scheme

The measurement for the three-mode output state is very similar to the TMDC output state, except now the same measurement needs to be repeated three times for the three pairs of modes. We have typically acquired 1000 triggers worth of data for each pair using the same ON-OFF measurement, where each trigger takes one second and gives 1 million samples. Similarly, pair-wise system calibrations are performed following each measurement. From all three acquisitions, a total of 21 terms of the upper diagonal of the three-mode covariance matrix $\mathbf{V}_{1,2,3}$ need to be computed.

4.5.2 Error propagation for tripatite entanglement tests

Numerical error propagation for PPT criterion

We do not have a simple closed-form expression for $\tilde{\nu}_{min}$ in the three-mode case. We will therefore numerically calculate the errors for the three-mode case. We will also verify the method by comparing numerically calculated results for the two-mode case to the analytical formulas above.

To calculate the derivatives, we treat $\tilde{\nu}_{min}$ as a function of the covariance matrix $\mathbf{V}$ and numerically vary the individual elements of $\mathbf{V}$ around their measured values. These variations are made with some constraints. First, we note that $\mathbf{V}$ is symmetric and vary accordingly the off-diagonal terms in symmetric pairs, $V_{mn} = V_{nm}$. The diagonal terms are varied individually.

With these constraints, we use the central difference method to calculate the partial derivatives of $\tilde{\nu}_{min}$ with respect to the elements $\{V_{mn}\}$. In more details, we calculate the partial derivative of $\tilde{\nu}$ with respect to the element V_{mn} as

$$\tilde{\nu}'_{mn} = \frac{\partial \tilde{\nu}}{\partial V_{mn}} = \frac{(\tilde{\nu}^{+}_{mn} - \tilde{\nu}^{-}_{mn})}{2d}, \tag{4.29}$$

where $\tilde{\nu}^{\pm}_{mn}$ are the symplectic eigenvalues computed for $\mathbf{V}$ with V_{mn} replaced by $V_{mn} \pm d$, keeping in mind the symmetry considerations noted above. The variation d is chosen to be an order of magnitude below the smallest error term.

With these partial derivatives, the total error $\sigma_{\tilde{\nu}}$ can be computed in the standard way as

$$\sigma^2_{\tilde{\nu}} = \sum_{m,n} (\tilde{\nu}'_{mn})^2 V^2_{\sigma_{mn}}$$

where the summation is restricted to the lower triangle of the matrices ($n \leq m$).

As a verification of our method, in the two-mode case we compared the numerically estimated error to the analytical error for the example in section 4.2.4. We obtain $\sigma_{\tilde{\nu}} = 0.00226$ and $\sigma_{\tilde{\nu}} = 0.00225$, respectively, validating the method.

Error propagation for genuine tripartite entanglement

As explained in the main text and Ref. [43], genuine tripartite entanglement was studied by computing the variances of linear combinations of the mode quadratures, namely $u =$

$h_1x_1 + h_2x_2 + h_3x_3$ and $v = g_1p_1 + g_2p_2 + g_3p_3$, where the h_i and g_i are arbitrary real constants. In particular, we examined the quantity $S = \Delta u^2 + \Delta v^2$. The error in S can then be computed by a straightforward application of standard propagation-of-error formulas. In particular, the expressions for the two variance terms are (for mean-zero variables):

$$\begin{aligned}\left\langle u^2 \right\rangle &= \left(h_1^2 \left\langle x_1^2 \right\rangle + h_2^2 \left\langle x_2^2 \right\rangle + h_3^2 \left\langle x_3^2 \right\rangle\right) + 2\left(h_1h_2 \left\langle x_1x_2 \right\rangle + h_1h_3 \left\langle x_1x_3 \right\rangle + h_2h_3 \left\langle x_2x_3 \right\rangle\right) \\ \left\langle v^2 \right\rangle &= \left(g_1^2 \left\langle p_1^2 \right\rangle + g_2^2 \left\langle p_2^2 \right\rangle + g_3^2 \left\langle p_3^2 \right\rangle\right) + 2\left(g_1g_2 \left\langle p_1p_2 \right\rangle + g_1g_3 \left\langle p_1p_3 \right\rangle + g_2g_3 \left\langle p_2p_3 \right\rangle\right).\end{aligned}$$

These give the error formulas

$$\begin{aligned}\sigma_{\langle u^2 \rangle} &= \sqrt{\sum_{i=1}^{3} \left(|h_i|^2 \sigma_{\left\langle x_i^2 \right\rangle}\right)^2 + \sum_{i=1}^{2} \sum_{j>i}^{3} \left(2|h_i||h_j| \sigma_{\langle x_i x_j \rangle}\right)^2} \\ \sigma_{\langle v^2 \rangle} &= \sqrt{\sum_{i=1}^{3} \left(|g_i|^2 \sigma_{\left\langle p_i^2 \right\rangle}\right)^2 + \sum_{i=1}^{2} \sum_{j>i}^{3} \left(2|g_i||g_j| \sigma_{\langle p_i p_j \rangle}\right)^2}.\end{aligned}$$

The total error in S thus equals

$$\sigma_S = \sqrt{\sigma_{\langle u^2 \rangle}^2 + \sigma_{\langle v^2 \rangle}^2}.$$

4.5.3 Results

Coupled-mode

For the coupled-mode case, we measured the 6 x 6 three-mode covariance matrix for the 4, 6 and 7 GHz modes as

$$\mathbf{V}_{CM} = \begin{array}{c} \\ x_1 \\ p_1 \\ x_2 \\ p_2 \\ x_3 \\ p_3 \end{array} \begin{array}{c} \begin{array}{cccccc} x_1 & p_1 & x_2 & p_2 & x_3 & p_3 \end{array} \\ \begin{pmatrix} 2.05 & 0.00 & 1.87 & 0.00 & 0.88 & 0.00 \\ 0.00 & 2.04 & 0.00 & -1.87 & 0.00 & 0.88 \\ 1.87 & 0.00 & 2.85 & 0.00 & 1.56 & 0.00 \\ 0.00 & -1.87 & 0.00 & 2.85 & 0.00 & -1.56 \\ 0.88 & 0.00 & 1.56 & 0.00 & 1.79 & 0.00 \\ 0.00 & 0.88 & 0.00 & -1.56 & 0.00 & 1.79 \end{pmatrix} \end{array}.$$

Bisqueezing

Similarly, for the bisqueezing scheme, we measured the 6 x 6 three-mode covariance matrix for the 4, 6 and 7 GHz modes as

$$\mathbf{V}_{BS} = \begin{array}{c} \\ x_1 \\ p_1 \\ x_2 \\ p_2 \\ x_3 \\ p_3 \end{array} \begin{array}{c} \begin{array}{cccccc} x_1 & p_1 & x_2 & p_2 & x_3 & p_3 \end{array} \\ \begin{pmatrix} 3.91 & 0.00 & 2.34 & 0.00 & 2.78 & 0.00 \\ 0.00 & 3.91 & 0.00 & -2.33 & 0.00 & -2.78 \\ 2.34 & 0.00 & 2.28 & 0.00 & 1.45 & 0.00 \\ 0.00 & -2.33 & 0.00 & 2.28 & 0.00 & 1.45 \\ 2.78 & 0.00 & 1.45 & 0.00 & 2.72 & 0.00 \\ 0.00 & -2.78 & 0.00 & 1.45 & 0.00 & 2.72 \end{pmatrix} \end{array}.$$

The correlations are color coded with significant positive (negative) correlations in blue (red). We visualize the above matrices with the common 3D bar chart of correlation in Fig. 4.10.

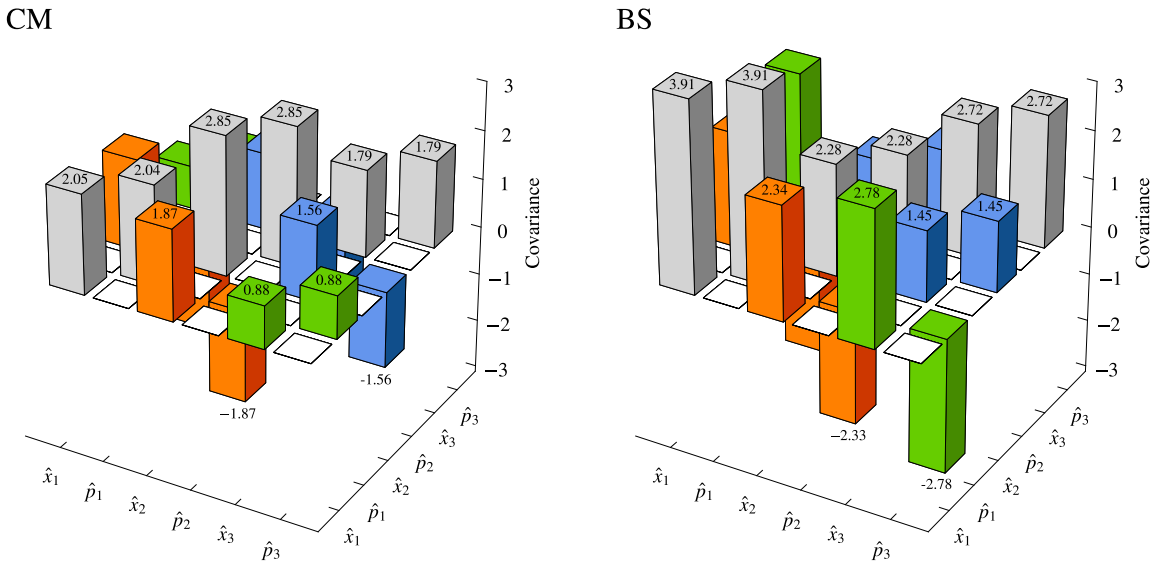

Figure 4.10: 3D bar plots for the three-mode covariance matrices. (left) Coupled-mode scheme. The two pairs of mode 1 & 2 and mode 1 & 3 are actively coupled by two simultaneously applied pump tones. One pump produces TMDC in mode 1 & 2 and gives the correlation structure $\langle \hat{x}_i \hat{x}_j \rangle = -\langle \hat{p}_i \hat{p}_j \rangle$. The second pump coherently coupled mode 1 & 3 and produces the correlation $\langle \hat{x}_i \hat{x}_j \rangle = \langle \hat{p}_i \hat{p}_j \rangle$. While mode 2 & 3 are not directly coupled by the pumps, they effectively exhibit the correlation structure of TMDC. This agrees with the prediction by the commutator calculated in 4.4.1. (right) Bisqueezing scheme. With TMDC simultaneous to mode 1 & 2 and mode 1 & 3 by the two pumps, we have the expected TMDC correlation structure $\langle \hat{x}_i \hat{x}_j \rangle = -\langle \hat{p}_i \hat{p}_j \rangle$. While mode 2 & 3 never directly interact, they exhibit a beam-splitter like correlation $\langle \hat{x}_i \hat{x}_j \rangle = \langle \hat{p}_i \hat{p}_j \rangle$, as if they were coherently coupled. Again, this agrees with the expectation from the commutator.

Full inseparability

Following the approach in the two-mode case, we first check to make sure the covariance matrices for the CM and BS schemes are both physical. They are confirmed in Table. 4.2. The results show a clear violation of entanglement bound for both schemes, indicating that the three-mode output states generated in both schemes cannot be written as product states of any bipartition of the modes. That is, the states are *fully inseparable*.

Genuine tripartite entanglement

Further, we test the output states using Eq. (4.28) to further rule out the possibility of expressing the three-mode states as a mixture of product states. As seen in the last column of Table. 4.2, we observed clearly that the bound is violated, showing that we have generated *genuine tripartite entanglement* with our output states.

	λ_{in}	ν_{min}	$\tilde{\nu}_{min}$ $\mathbf{V}_{4-67}$	$\mathbf{V}_{6-47}$	$\mathbf{V}_{7-46}$	$\mathcal{N}^{\text{tri}}$	S
CM	$.39 \pm .003$	$1.03 \pm .002$	$.476 \pm .002$	$.390 \pm .002$	$.569 \pm .002$	$.73 \pm .005$	$1.49 \pm .01$
BS	$.30 \pm .005$	$1.02 \pm .002$	$.305 \pm .003$	$.479 \pm .004$	$.386 \pm .004$	$.94 \pm .012$	$1.19 \pm .01$

Table 4.2: Entanglement measures of the three-mode output states. The $\tilde{\nu}_{\text{min}}$ column reports the minimum symplectic eigenvalues for all three bipartition. The $\mathcal{N}^{tri}$ column reports the tripartite negativity. The S column reports the measure of genuine tripartite entanglement in Eq.(4.28). The entanglement conditions are $\tilde{\nu}_{\text{min}} < 1$; $\mathcal{N} > 0$; and $S < 2$. Statistical errors are calculated using the numerical method described above.

With the above results, we conclude that device is capable of generating tripartite entanglement. We note that the method employed can be scaled up to entangling more number of modes by simultaneously applying more pump tones. In terms of limitations in our device, the degree of entanglement appears to be limited the purity of the states. We observe that the purity of the states simultaneously declines when the cavity is pumped harder. This suggests a nonideality such as higher-order nonlinearities or parametric coupling to other modes. In the future, more work can be dedicated to improving the purity of the states, as well as attempting to entangle more modes.

Chapter 5

An application of TMDC: Quantum-enhanced noise radar

As demonstrated in chapter 4, the two output modes, i.e. the signal and idler beams, generated by TMDC exhibit strong quantum correlations which are a form of entanglement. In particular, the correlations can be stronger than anything allowed by classical physics, giving the TMDC output a "quantum advantage". The correlations appear to be very robust in the presence of background noise and loss, as shown by a significant amount of covariance detected at room temperature (see section 4.2.4). Recent work has explored the use of these entangled beams for various applications, such as improving the sensitivity of radar and other target detection technologies [45, 46, 47]. The class of applications is often broadly referred to as "quantum illumination" (QI).

In this chapter, we will study one potential application of QI where we attempt to implement a form of noise radar using the TMDC signals. Recent experiments have demonstrated the basic principle of QI using TMDC at optical frequencies [48, 49, 50]. These are important results, however, conventional radar systems typically work at microwave frequencies. For this reason, it is of interest to study and possibly demonstrate QI in microwave regime. Recent work has studied some technical challenges of microwave QI and found them to be comparable to optical QI [51, 52, 53].

In the QI protocols mentioned above, it is assumed that the idler beam is maintained *in vivo*, for example, by running it in a lossless delay line or a quantum memory device. It is meant to be combined with the returning signal beam for performing a joint measurement, such as an interference measurement. While theoretically a joint measurement offers the best possible quantum performance, it creates problems which prevent it from

being practical. Notably, it essentially requires foreknowledge of the range of the target to be detected in order to allow the signal and idler to be combined at the same time for correlation.

We propose a novel protocol that we call quantum-enhanced noise radar (QENR). In our implementation, we relax the challenging requirement of joint measurement required by the existing protocols. This makes our schemes much more practical when compared to others. While giving up the joint measurement it may cause a reduction in the theoretical signal-to-noise ratio due to the additional noise from the amplifier. Here we note that the additional noise is small compared to the ambient noise and loss expected in any practical application. We will present a proof-of-principle experiment where we demonstrate a quantum enhancement in the detected signal-to-noise ratio of an order of magnitude. This is achieved by comparing the performance of an entangled-photon source to an ideal classical noise source which saturates the classical bound for correlation.

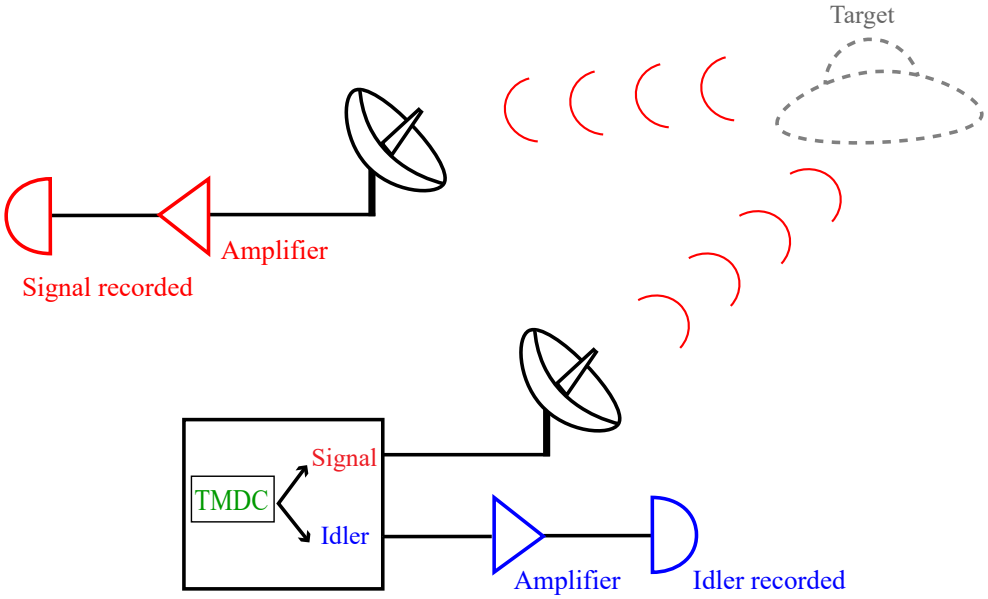

Figure 5.1: Cartoon of the proposed quantum-enhanced noise radar protocol. Amplifiers are used to measure both quadratures of the signal and idler. The idler beam is immediately recorded as a classical copy, while the signal beam is projected into the detection region. A second receiver will detect any returning signal beam. A detection event is inferred when the received signal correlates with the idler, indicating that a target is present and has reflected some parts of the signal beam.

5.1 Noise radar

We start by describing some basic principles of a noise radar. With a transceiver, the signal source emits a probe beam which is digitally designed to appear as noise, e.g., a continuous wave signal amplitude-modulated by a known Gaussian distribution. The receiver then continuously probes for any possible reflections of the emitted beam by a potential target. The reflected beam can be distinguished from the ambient noise by measuring the correlation between the received beam and the digital record used to generate the emitted beam. When the two correlate, a reflection is inferred and we learn that a target is present.

Noise radar has gained more attention because of the inherent difficulty in detecting the probe beam against the ambient thermal background noise [54, 55], essentially making the detection process invisible from the point of view of the target.

5.1.1 Quantum-enhanced noise radar

Our QENR protocol relies on the fundamental property of TMDC. An important characteristic of TMDC is that if one individually measures the signal or idler beams, they appear simply as thermal noise. It is only when both beams are measured and compared against each other that the strong correlation can be observed. The apparent thermal nature of the individual signal and idler enables us to utilize them in a noise radar.

In our scheme (see Fig. 5.1), the sensing transceiver will contain a TMDC source. One of the generated beams, say the idler beam, will be measured immediately by the transceiver, converting it into a classical record that can be copied and stored. The signal beam will be transmitted into the detection region. On the receiver side, the returning signal is then measured and also converted into a classical record. Instead of simply probing the amplitude or power of the returning signal, the signal and idler records are correlated digitally over an arbitrarily long time delay (see section 4.2.4). When a correlation is detected we know that the target is present, having reflected some part of the signal beam. Conversely, even if the receiver detects high power background noise from the environment, that noise will be uncorrelated with the idler and, thus, rejected.

The key advantage of the QENR protocol is that quantum mechanics makes it possible for the correlations between the signal and idler beams in TMDC to be significantly stronger than those allowed for classical beams. Due to this, it is predicted that the detection efficiency of a QENR system could exceed that of a classical system using the same beam power.

5.2 Experimental setup for quantum and classical illumination comparison

In our proof-of-principle experiment, we will compare various properties of quantum illumination from TMDC with that of a classical illumination from a classical source. Here we briefly introduce the setup designed around a direct comparison of the two types of illumination.

5.2.1 Illumination sources

Source of quantum illumination

Quantum illumination is given by the TMDC outputs generated from our device. In the measurement of quantum illumination, the input port to the device is terminated with 50 Ω termination at room temperature. The cavity modes are then in a cold vacuum state. Then, following section 4.1, we pump our device at the sum frequency of two modes, which perform SPDC to the modes and provide the signal and idler beams. In the experiment, we will stick to the same frequency configuration introduced in section 4.2.4.

Source of classical illumination

Meanwhile, the classical illumination considered here is an ideal classical analog of our quantum signal. It is represented by a pair of classically correlated beams which saturate the classical bound. To make the closest possible comparison, the beam should exhibit the same correlation structure as TMDC. These ideal classical beams can be generated at room temperature using readily available microwave equipment. We use a vector generator to generate band-limited Gaussian noise centered roughly at 1 GHz. This noise is then mixed with a carrier at approximately 5 GHz. This creates two sidebands of noise beam that have the same correlation structure as our TMDC source. In the experiment, the frequencies are selected such that the center frequency of the sidebands exactly matched our quantum signal and idler beams in section 4.2.4. At room temperature, we have verified that the correlation between the classical signal and idler sidebands is 99% (see Fig. 5.2). It is only limited by small experimental imperfections, e.g., nonideal behaviour of the mixer.

5.2.2 Signal routing for comparing quantum and classical beams

In the experiment, the signal and idler beams were always guided through cables and no antenna was used. This configuration represents the situation where a target is present and has reflected part of the beam. Meanwhile, the system noise and cable loss plays the role as the ambient noise and loss in a radar operation. We can thus focus on our goal to compare the performance of the quantum and classical beams as the probe.

The quantum beams emitted by our device travels through the amplifier chain to digitizers at room temperature as described in section 3.2.2. To directly compare classical beams and quantum beams, we inject the classical beams into the cryostat from the input (see Fig. 5.2) and attenuate them down to single-photon level. The injected classical beams are reflected off the unpumped cavity device where they then enter the amplifier chain in the exact same way as the quantum beams emitted by the device. As a result, the quantum and classical beams are scaled by the same system gain and have the same amount of system noise added. This is crucial for our comparison scheme, allowing us to directly compare the two types of beams using the RT measured data alone.

Quantifying the power of illuminations

We can quantify the source output by the measured beam power P_i for mode i, and the measured covariance between two beams C. When comparing the quantum and classical cases, due to the low beam power and the drift in system noise (see section 3.5.1), it is often necessary to subtract the system noise power from the beam power before different beams can be compared.

As the covariance is computed over two modes, we need to consider the subtracted powers for both modes. For simplicity, it is convenient to specify a single power quantity by considering the geometric average of the two subtracted powers. Thus, we quantify the output by defining the differenced signal power P_M,

$$\begin{aligned} P_M &= \sqrt{\left(P_{1,ON} - P_{1,OFF}\right)\left(P_{2,ON} - P_{2,OFF}\right)} \\ &= \sqrt{\left[\left\langle \hat{I}^2_{1,\text{sub}} \right\rangle + \left\langle \hat{Q}^2_{1,\text{sub}} \right\rangle\right]\left[\left\langle \hat{I}^2_{2,\text{sub}} \right\rangle + \left\langle \hat{Q}^2_{2,\text{sub}} \right\rangle\right]}. \end{aligned} \tag{5.1}$$

where $\left\langle \hat{I}^2_{1,\text{sub}} \right\rangle = \left\langle \hat{I}^2_{1,ON} \right\rangle - \left\langle \hat{I}^2_{1,OFF} \right\rangle$ is the subtracted variance of I_1. The same applies for other quadratures. Then, P_M can be obtained from the ON-OFF subtracted measurement considered in section 4.2.1. In the quantum case, the ON-OFF is done by toggling the

pump on and off. In the classical case, the ON-OFF is done by toggling the classical source on and off.

5.2.3 Effect of ambient noise and signal loss

One of the most promising aspects of QENR is its resiliency to noise and loss. As the signal transmission takes place fully inside the cryostat, we can use the system noise and the cable loss to simulate ambient noise and loss. This allows us to understand how additive noise and loss under ambient conditions affect our protocol. While the considered noise will then be fixed, it is still possible to vary the signal-to-noise ratio of the system by changing the beam power. For quantum beams this is controlled by the pump power applied to our device. For classical beams, we can simply vary the generated power by the vector generator at room temperature.

5.3 Comparing the quantum and classical protocols

In the following sections, we will compare the performance of our quantum and classical source. The comparisons considered below are based on the measured variance and covariance of the beams. For all cases, we will measure the output strength of the quantum and classical illuminations using the differenced signal power P_M developed in section 5.2.2, such that the two cases are compared equally.

5.3.1 Raw covariance comparison

We study the raw covariance including added noise, measured between the signal and idler beams. These measurements directly simulate the detection principle of our proposed QENR protocol. The system noise and cable loss plays the role of ambient noise and loss experienced by the signal beam as it propagates to and from the target. The raw covariance amplitude between signal and idler is the detection signal of our system. That is, the detection of a finite covariance indicates the presence of a target. As a result, the raw covariance (computed directly from the I and Q data) acts as a benchmark of the probe beams. The covariance is plotted against a range of P_M for the quantum and classical illumination in Fig. 5.2.

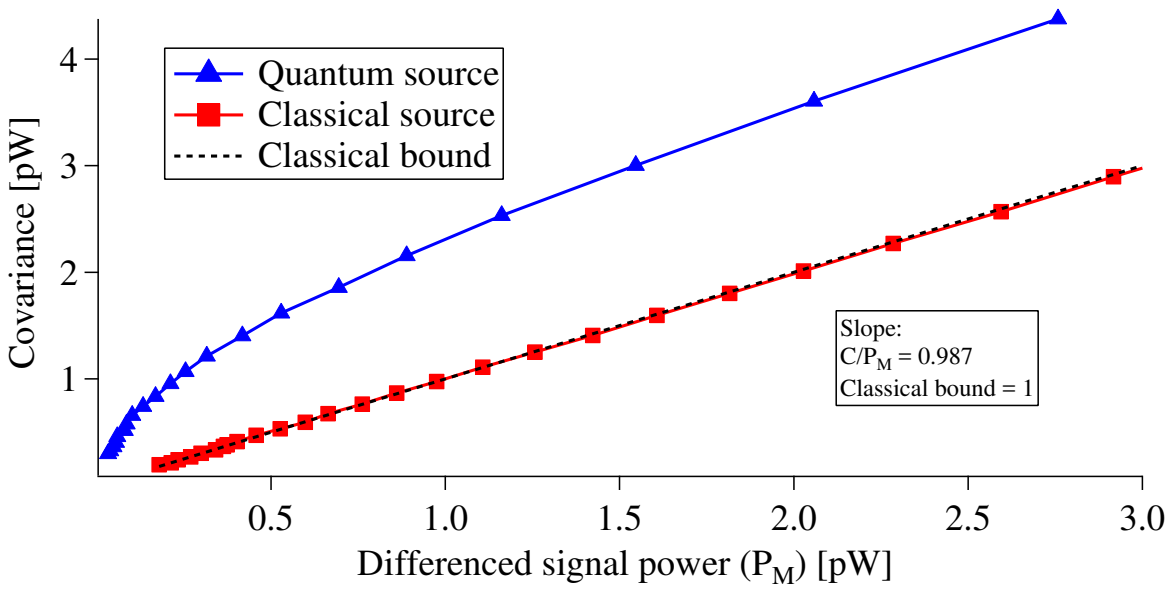

Figure 5.2: Comparing the raw, detected covariance between the signal and idler beam from the quantum and classical source. The bottom axis is P_M defined in Eq. (5.1). The left axis shows the detected raw covariance. At all powers, the covariance of the quantum source is higher than that of the classical source, illustrating the quantum enhancement.

From Fig. 5.2, we clearly observe that the quantum source provides higher covariance over the close-to-ideal classical source at all powers. This illustrates the enhancement created by the TMDC process. In these measurements, we attempted to measure the covariance with as low power as possible for both cases. Interestingly, as shown by the left side of the figure, we established that we could measure covariance at a lower power from the quantum source when compared to the classical source. This is an indication that the quantum protocol has a better signal-to-noise ratio than the classical protocol at the same power.

5.3.2 Quantum enhancement

To make the enhancement more evident, we define the quantity "quantum enhancement (E_Q)" as a ratio of the detected covariances for the quantum and classical sources. We note that since the measurement statistics of both the signal and noise are the same for the

classical and quantum case, the ratio of the covariances is the ratio of the signal-to-noise ratios.

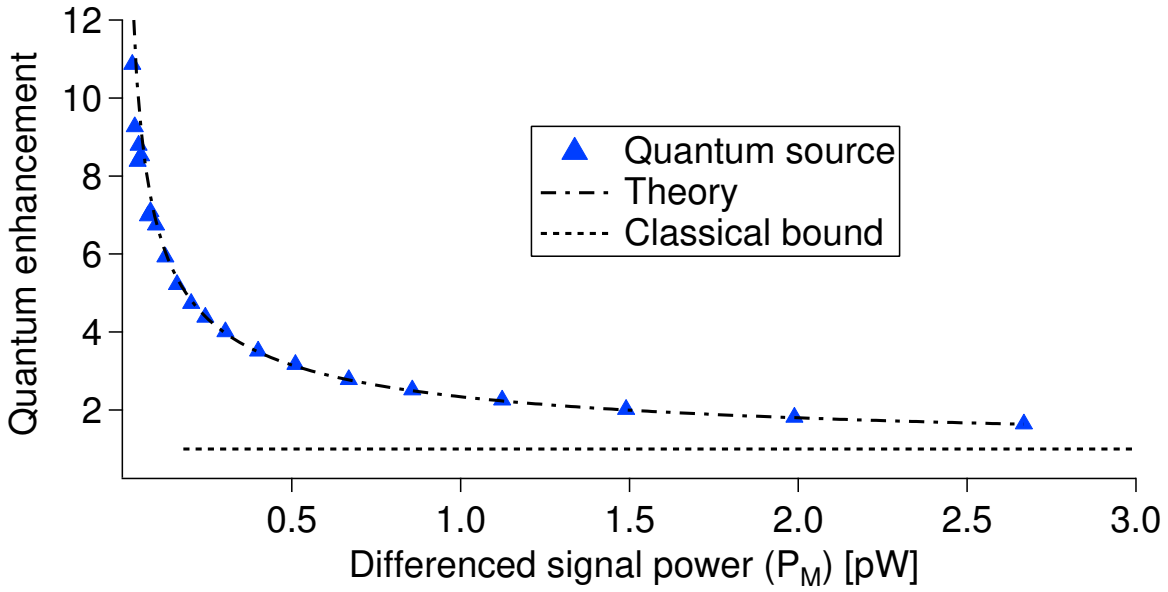

Figure 5.3: Quantum enhancement. We plot the ratio of the detected covariances for our quantum and classical sources as a function of P_M. The experimental data are fit to the expression in Eq. (5.3), derived for an ideal parametric amplifier. We observe that at the lowest powers, the quantum enhancement can exceed a factor of ten.

We plot the quantum enhancement over a range of differenced signal power in Fig 5.3. The enhancement starts from a high value and drops asymptotically with increasing output power, towards the classical bound of one. For the lowest powers, we were able to measure an enhancement exceeding a factor of ten.

Fitting experimental data with expected quantum enhancement

To further verify the quantum enhancement measured in Fig. 5.3 with theory, we can derive a simple expression for E_Q by assuming the device operates as an ideal parametric amplifier. Then we can attempt to fit the experimental data with the predicted E_Q.

By squeezing from a vacuum state, the output quadrature variance of mode i is $\langle \hat{x}_i^2 \rangle_Q = \cosh(2r)$ and the covariance between two modes is $\langle \hat{x}_i \hat{x}_j \rangle_Q = \sinh(2r)$. With an ideal

classical source, PPT bound corresponds to the variance minus a unit of vacuum noise (see Eq. (4.10)), that is $\langle \hat{x}_i \hat{x}_j \rangle_C = \cosh(2r) - 1$. In the last expression, we have taken the classical output power to be the same as the quantum output power. We note that the measured C_Q and C_C are both scaled by the same normalization factor P_0, respectively, to $\langle \hat{x}_i \hat{x}_j \rangle_Q$ and $\langle \hat{x}_i \hat{x}_j \rangle_C$ in the conversion from I,Q data to device output variance (see section 3.4.4). Thus, we get a simple expression of E_Q in terms of the squeezing parameter r,

$$\begin{aligned} E_Q(r) &= \frac{C_Q}{C_C} \\ &= \frac{C_Q/P_0}{C_C/P_0} = \frac{\langle \hat{x}_i \hat{x}_j \rangle_Q}{\langle \hat{x}_i \hat{x}_j \rangle_C} \\ &= \frac{\sinh 2r}{\cosh 2r - 1} \end{aligned} \tag{5.2}$$

$P_0 = \hbar BW\sqrt{G_1 G_2 \omega_1 \omega_2}/2$ is the scaling factor related to section 3.4.4. We note that Eq. (5.2) is a function of squeezing parameter r to which we do not have direct access. However, with our ideal classical source, $C_C = P_M$ and we can express r in terms of P_M.

$$\begin{aligned} \frac{C_C}{P_0} = \frac{P_M}{P_0} &= \cosh 2r - 1 \\ r &= \frac{1}{2} \cosh^{-1}\left(1 + \frac{P_M}{P_0}\right). \end{aligned}$$

Using the identity $\sinh\left(\cosh^{-1}(x)\right) = \sqrt{x^2 - 1}$, E_Q becomes

$$\begin{aligned} E_Q(P_M) &= \frac{\sinh\left(\cosh^{-1}\left(1 + P_M/P_0\right)\right)}{P_M/P_0} \\ &= \sqrt{1 + 2\frac{P_0}{P_M}} \end{aligned} \tag{5.3}$$

In Fig. 5.3, we include a fit of the data to the theoretical expression Eq. (5.3) with the single fitting parameter being $P_0 \propto G = \sqrt{G_1 G_2}$. The extracted value of $G = 61.1$ dB agrees well with the results of the independent calibration from SNTJ, which gives $G = 62.4$ dB.

5.4 Implication of the results

We note that our noise radar analog may not be the optimal classical detection scheme. Still, the experiment confirms that given the same ambient noise and beam power, the quantum source is superior to the best classical source giving a signal-to-noise ratio improvement exceeding a factor of ten.

Also, the quantum enhancement demonstrated may have practical implications for certain applications. Since the QI source and noise radar beam naturally look like thermal noise they are difficult to distinguish from the ambient thermal background, even if they are absorbed by a detector. Conversely, the man-made nature of a coherent probe belies the presence of the radar system. In applications where it is desirable to avoid detection of the radar system, the quantum enhancement demonstrated here will allow for the probe power to be further reduced, improving the undetectability of the system.

Chapter 6

Three-photon parametric processes

Since the early days, the generalization of the standard two-photon SPDC to many-photon SPDC have been explored. However, this seemingly natural next step has been proven difficult, both theoretically [56, 57, 58] and experimentally [59, 60]. Even demonstrating the next order, three-photon SPDC which generates photon triplets, has been a decades-long, on-going endeavour [15, 16, 17, 18]. This process was studied theoretically in the context of generalized squeezing [61, 62] where the vacuum state is shaped by the action of Hamiltonians with terms beyond a quadratic order. These higher-order squeezed states are known to exhibit non-Gaussian features, making them a promising resource for universal quantum computation with linear optics [63, 64]. Moreover, multimode three-photon SPDC has also been predicted to create entangled states, such as GHZ states [65], as well as heralded entangled pairs [66]. They are also potential resource states for novel quantum communication protocols, such as quantum secret sharing [67]. Despite the great interest, higher order nonlinearity is generally weaker, and direct three-photon SPDCs have been out of reach in quantum optics experiments.

In microwave quantum optics, with the flexibility of a SQUID, we can engineer Hamiltonians that enhance the terms necessary for three-photon SPDCs. In fact, with some modifications of our previous SQUID designs we were able to perform three-photon SPDCs to single and multiple modes, and observe the corresponding output signals. Throughout this chapter, we will explore the experimental aspect of three-photon SPDC from its generation mechanism to the analysis of output states.

6.1 Accessing three-photon interactions in SQUIDs

In the standard flux-pump configuration, the SQUID is designed to be symmetric (with two identical Josephson junctions) for maximum flux tunability. With this SQUID design, however, cavity fields only appear in even powers, forbidding the third order interactions needed for three-photon SPDCs. In order to realize three-photon SPDC, we need to introduce odd powers into the expansion. This can be conveniently done by introducing asymmetry to the SQUID design.

To understand the source of third order interactions in SQUID, we can take a step back and consider the SQUID energy without assuming identical junctions. The total SQUID energy is given by the sum of Josephson energy of the two junctions (α and β),

$$\hat{H}_{\mathrm{SQ}} = E_{J_\alpha} \cos\left(2\pi \frac{\hat{\Phi}_\alpha}{\hat{\Phi}_0}\right) + E_{J_\beta} \cos\left(2\pi \frac{\hat{\Phi}_\beta}{\hat{\Phi}_0}\right)$$

Using the change of variable in section 2.1.2,

$$\begin{aligned}
\hat{H}_{\mathrm{SQ}} &= E_{J_\alpha} \cos\left(2\pi \frac{\hat{\Phi}_c}{\Phi_0} - \pi \frac{\hat{\Phi}_{ext}}{\Phi_0}\right) + E_{J_\beta} \cos\left(2\pi \frac{\hat{\Phi}_c}{\Phi_0} + \pi \frac{\hat{\Phi}_{ext}}{\Phi_0}\right) \\
&= \left(E_{J_\alpha} + E_{J_\beta}\right) \left|\cos\left(\pi \frac{\hat{\Phi}_{ext}}{\Phi_0}\right)\right| \cos\left(2\pi \frac{\hat{\Phi}_c}{\Phi_0}\right) \\
&\qquad - \left(E_{J_\alpha} - E_{J_\beta}\right) \sin\left(\pi \frac{\hat{\Phi}_{ext}}{\Phi_0}\right) \sin\left(2\pi \frac{\hat{\Phi}_c}{\Phi_0}\right).
\end{aligned} \tag{6.1}$$

Eq. (6.1) reduces to Eq. (2.13) of a symmetric SQUID if $E_{J_\alpha} = E_{J_\beta} = E_J$. To proceed with the analysis, consider the case with the SQUID set to zero flux bias, i.e. $\hat{\Phi}_{ext} = \hat{\Phi}_p$. The Taylor series of the cosine and sine terms are then purely even and odd order expansions in flux, respectively. With the second term of Eq. (6.1), similar to section 2.2.2, we can now expand the pump flux (red) to the first order and the cavity flux (blue) to the third order. We arrive at the familiar SQUID interaction Hamiltonian

$$\hat{H}_{\mathrm{SQ}} \approx \hbar g_0 \left(\hat{a}_p + \hat{a}_p^\dagger\right) \left(\hat{a}_1 + \hat{a}_1^\dagger + \hat{a}_2 + \hat{a}_2^\dagger + \hat{a}_3 + \hat{a}_3^\dagger\right)^3, \tag{6.2}$$

except now we have the bosonic operators raised to cubic power.

6.1.1 Interaction strength comparing to two-photon processes

From the above derivation, we can roughly estimate the interaction strength of three-photon processes compared to the ordinary two-photon processes. We predict that the interaction strength will be significantly weaker in the three-photon processes.

First, we notice that Eq. (6.2) comes from the sine terms where the coefficient is the difference in Josephson energy of the two junctions, comparing to the sum energy of the cosine terms. This alone suggests that the three-photon interaction is weaker than the two-photon interaction by a ratio $\left(E_{J_\alpha} - E_{J_\beta}\right) / \left(E_{J_\alpha} + E_{J_\beta}\right)$. Second, the expansion to a third order in cavity flux requires an additional factor of $1/3$ comparing to a second order. With our device having an asymmetry of $1 : 1.7$, these translate to around an overall 10 dB lower interaction strength. Meanwhile, when doing three-photon SPDCs, the pump frequency needed is in general higher (e.g. being the sum of three modes instead of two), often increasing the cable loss by $5 - 10$ dB. As a result, a higher pump coupling is essential to realize three-photon interactions. In our new designs, this is addressed by utilizing kinetic inductance (see section 2.1.2).

The above reasoning provides a general idea on the pump power needed. The practical pump strength needed for the individual three-photon interaction will further depend on, for instance, the expansion coefficients of the individual terms in Eq. (6.2), as well as the transmission/reflection of the corresponding pump signal by the pump line.

6.2 Three-photon interactions due to the SQUID

Given how similar the three-photon interaction Hamiltonian (Eq. (6.2)) is to its two-photon counterpart (Eq. (2.15)), naturally, we expect it to also give multiple types of interactions with the same flexibility on their selective activations. This is indeed the case and, now with the cubic expansion, Eq. (6.2) exhibits an even richer set of interactions with each having a three-body interaction structure.

From the expansion of Eq. (6.2), by pumping the SQUID, we can follow the approach in section 2.2.2 to apply both the rotating wave and parametric approximation to analyse the individual interactions. We identify the following five types of three-photon interactions, separated into two categories.

6.2.1 Three-photon SPDCs

Unlike two-photon SPDCs which generate photon pairs, these three-photon SPDC processes can generate photon triplets in the output states. Being spontaneous processes, photons can be downconverted from the pump to the modes with all the downconverted modes initially sitting in a cold vacuum state, similar to their two-photon counterparts. When a "seed" is injected to any of the downconverted modes, it will result in stimulated downconversions and the processes can behave like a generalized parametric amplification process. In the following, we will list various three-photon processes achievable with our new SQUID design.

Single-mode three-photon SPDC

By driving the cavity with a pump frequency at three times a one mode frequency, e.g. $\omega_p = 3\omega_1$, we have the effective interaction Hamiltonian

$$\hat{H}_{1M} = \hbar g \left(\hat{a}_1^3 e^{i\theta_p} + \hat{a}_1^{\dagger 3} e^{-i\theta_p} \right). \tag{6.3}$$

Through this Hamiltonian, one pump photon is converted to three photons into the same mode.

Two-mode three-photon SPDC

Driving the cavity with a pump frequency at the sum of one mode and the double of another mode, e.g. $\omega_p = 2\omega_1 + \omega_2$, we have the effective interaction Hamiltonian

$$\hat{H}_{2M} = \hbar g \left(\hat{a}_1^2 \hat{a}_2 e^{i\theta_p} + \hat{a}_1^{\dagger 2} \hat{a}_2^\dagger e^{-i\theta_p} \right). \tag{6.4}$$

Through this Hamiltonian, one pump photon is converted to three photons, where two photons go to mode 1 and one goes to mode 2.

Three-mode three-photon SPDC

Driving the cavity with a pump frequency at the sum of three modes, e.g. $\omega_p = \omega_1 + \omega_2 + \omega_3$, we have the effective interaction Hamiltonian

$$\hat{H}_{3M} = \hbar g \left(\hat{a}_1 \hat{a}_2 \hat{a}_3 e^{i\theta_p} + \hat{a}_1^\dagger \hat{a}_2^\dagger \hat{a}_3^\dagger e^{-i\theta_p} \right). \tag{6.5}$$

Through this Hamiltonian, one pump photon is converted to three photons, from which mode $1, 2$ and 3 each gains one photon.

6.2.2 Three-photon coupling

Not surprisingly, there also exist three-photon coupling interactions that generalize the coherent beam-splitter coupling in two-photon processes. Such three-photon coupling processes are imbalanced, annihilating photon pairs to create single photons, and vice versa. As a result, we expect the two-photon port and the single-photon port of a three-photon coupling device to act different on the input signal. Similar to coherent coupling, three-photon coupling occurs only when at least one of the coupled mode contains photons, i.e. no photons can be created from the vacuum state. Below are two couplings we have tested with our device.

Two-mode generalized coupling

Pumping the cavity with $\omega_p = |2\omega_1 - \omega_2|$, we have the effective interaction Hamiltonian

$$\hat{H}_{2MC} = \hbar g \left(\hat{a}_1^2 \hat{a}_2^\dagger e^{i\theta_p} + \hat{a}_1^{\dagger 2} \hat{a}_2 e^{-i\theta_p} \right). \tag{6.6}$$

Through this Hamiltonian, two photons in mode 1 are swapped with one photon in mode 2.

Three-mode generalized coupling

Pumping the cavity with $\omega_p = |\omega_1 + \omega_2 - \omega_3|$, we have the effective interaction Hamiltonian

$$\hat{H}_{3MC} = \hbar g \left(\hat{a}_1 \hat{a}_2 \hat{a}_3^\dagger e^{i\theta_p} + \hat{a}_1^\dagger \hat{a}_2^\dagger \hat{a}_3 e^{-i\theta_p} \right). \tag{6.7}$$

Through this Hamiltonian, two photons, one each in mode 1 and 2 are swapped with one photon in mode 3.

6.2.3 Trisqueezed states

In the remaining sections of the thesis, we will focus on studying the three types of three-photon SPDC starting from a cold vacuum input state. We refer to the states produced by three-photon SPDC as trisqueezed states. The motivation for this name will become clearer as we look at the phase space distribution of the single-mode trisqueezed state. A summary of the pump and mode frequencies used in the experiments are summarized in Table. 6.1.

SPDC	Combinations	Frequency [GHz]			
		Pump	Mode 1	Mode 2	Mode 3
Single-mode	$f_{p1} = 3 \times f_1$	12.6	4.2	-	-
Two-mode	$f_{p2} = 2 \times f_1 + f_2$	14.5	4.2	6.1	-
Three-mode	$f_{p3} = f_1 + f_2 + f_3$	17.8	4.2	6.1	7.5

Table 6.1: A list of three-photon SPDC processes explored in this thesis.

6.3 Single-mode trisqueezed state

Starting from a cold vacuum state, under the evolution by a degenerate SPDC Hamiltonian, photons are generated into the same mode, interfering with each other to create distinct patterns in the phase space. In the ordinary two-photon single-mode squeezed state, the two photons interfere such that the Wigner function gives an elliptical profile. This state exhibits a nonclassical property where the variance of one quadrature can fall below that of a vacuum state [68]. It is therefore interesting to understand what the consequences are of quantum interference in a trisqueezed state.

6.3.1 Statistical characteristics of single-mode trisqueezed states

With single-mode trisqueezed states, instead of an elliptical profile, a triangular, star-like profile was predicted [69] in the phase space. As a result, this state had also been called a star state. It was also expected that a general squeezed state with an order $k > 2$ will not have ordinary squeezing of uncertainty [62], and the output state is not necessarily of minimum uncertainty.

Measurement of single-mode trisqueezed state

To characterise the state, we measure the propagating trisqueezed state output from the device at around 4.2 GHz, while pumping the device at 12.6 GHz. Following the previous experiments, we used a sampling frequency of 1 MHz and a trigger period of one second. As the output signal goes through the amplifier chain, we calibrate the system gain using SNTJ (see section 3.3) and scale the room temperature measured power back to the spectral density of the state at the device output, in unit of number of photons per second per Hertz according to section 3.4. For convenience in the following discussion, we define the photon flux density, $F(\omega)$ defined by $\left\langle \hat{a}^\dagger(\omega)\hat{a}(\omega')\right\rangle = F(\omega)\delta(\omega - \omega')$.

Bright single-mode trisqueezed state

Fig. 6.1 shows the quadrature histogram of a bright trisqueezed state. We can clearly observe the predicted star-shaped profile in the histogram. As the generated output state is a high power ($F = 66$), the profile is very clear even on top of the system noise of $F = 35$. With the cubic Hamiltonian Eq. (6.3) which has three operators, it should lead to three-body correlations. Thus, the trisqueezed state should exhibit a significant third order moment and is therefore a non-Gaussian state. Projecting onto the $\hat{x}$ quadrature, we clearly see the expected non-Gaussian characteristics. We can quantify the non-Gaussian character of our measured quadratures using the third standardized moment, also called skewness, which for the random variable y is given by $\gamma(y) = \frac{\overline{(y-\overline{y})^3}}{\sigma_y}$. The overline represents the expectation value, $\overline{y}$ is the mean and σ_y^2 is the variance of y. Roughly, the skewness measures the asymmetry of the distribution of y and is zero for Gaussian variables. We can also associate γ with the three-photon quantum correlator $\langle \hat{x}_\phi^3 \rangle$. (With our states, $\overline{y}$ is essentially zero.)

From Fig. 6.1, the asymmetry of the measured quadrature distributions is not invariant under phase rotations, that is, the skewness of $\hat{x}$ and $\hat{p}$ are not generally identical. To study the transformation properties of the skewness, we define the generalized quadrature $\hat{x}_\phi = \hat{x}\cos\phi - \hat{p}\sin\phi$. We can then study the skewness of the measurement of $\hat{x}_\phi$. We define for simplicity $\gamma_\phi = \gamma(x_\phi)$ where we use x, p to represent a classical measurement record associated with the observables $\hat{x}, \hat{p}$. γ_ϕ measures the asymmetry of the quadrature distribution with respect to the symmetry axis perpendicular to the direction of $\hat{x}_\phi$. By digitally rotating the data, we measure γ_ϕ for different ϕ to form the polar plot in Fig. 6.1. The polar plot gives the same three-fold symmetry as the data with very high signal-to-noise ratio, despite it being a higher-order statistic. We can conclude from the strong nodes at $\phi = \frac{2\pi}{3}(n + 1/2)$ that the skewness of the system noise is indeed small. Also, we can observe that the nodes correspond to angles where the symmetry plane aligns with a lobe of the star, while the antinodes correspond to the symmetry planes being perpendicular to a lobe. From the above, we find the measurement of γ_ϕ a useful way to characterize the non-Gaussian character of the single-mode trisqueezed states.

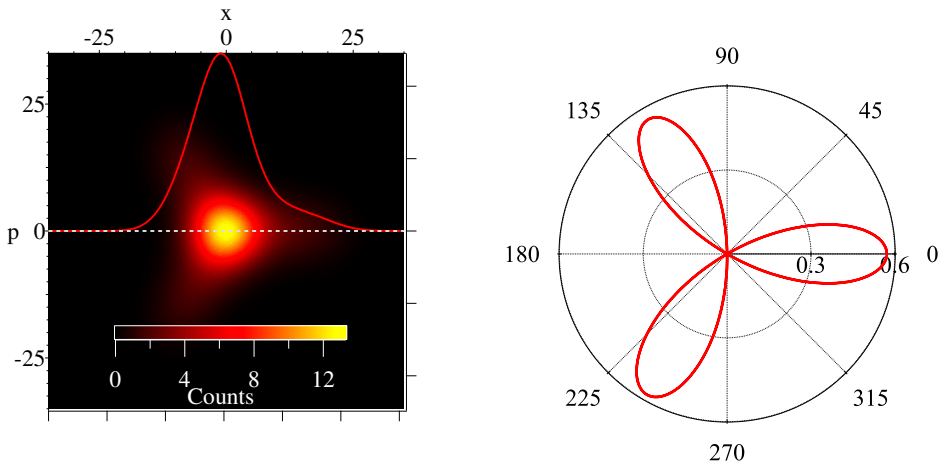

Figure 6.1: The phase space distribution of single-mode trisqueezed state, with $F = 66$. (left) The 2D histogram of the quadratures in the presence of system noise ($F = 35$). The x and p scaling has been calibrated with the system gain obtained from SNTJ to reflect the quadrature amplitude at the device output. The profile clearly indicates the expected triangular, star-shaped profile. The red curve is plotting the distribution along the axis of $\hat{x}$ quadrature, showing that the distribution is clearly skewed. (right) A polar plot of γ_ϕ (see text). The polar plot shows the same three-fold symmetry observed in the quadrature histogram. The node of the polar plot falls almost to zero, as the system noise is Gaussian and it does not contribute to the skewness computation.

Weak single-mode trisqueezed state

Quantum mechanical properties are often fragile, thus, it is desirable to also analyse data with a weak drive. However, with the weaker output, it makes observing the trisqueezed state more difficult, particularly in the presence of the strong system noise. For instance, consider the weak single-mode trisqueezed state with $F = 1.16$ in Fig. 6.2.

As the signal power is much weaker than the Gaussian system noise, the star-shaped profile of the signal is largely obscured. As a result, it becomes difficult to judge if the output contains the desired state. Nonetheless, the profile of the state can still be extracted by forming the polar plot of γ_ϕ, illustrated in Fig. 6.2. Despite the weak flux of the trisqueezed state, we still obtain a very clear profile of the three-fold symmetry. This suggests that the trisqueezed state, even at a very low flux density $F = 1.16$, shows a clear non-Gaussian character. This again shows that skewness analysis is a useful approach for

analysing trisqueezed states. We note that the symmetry of the state can also be observed by subtracting the 2D histogram of the system noise. The ON-OFF subtracted histogram (with 10^9 samples averaged) shows the same three-fold symmetry contained in the signal.

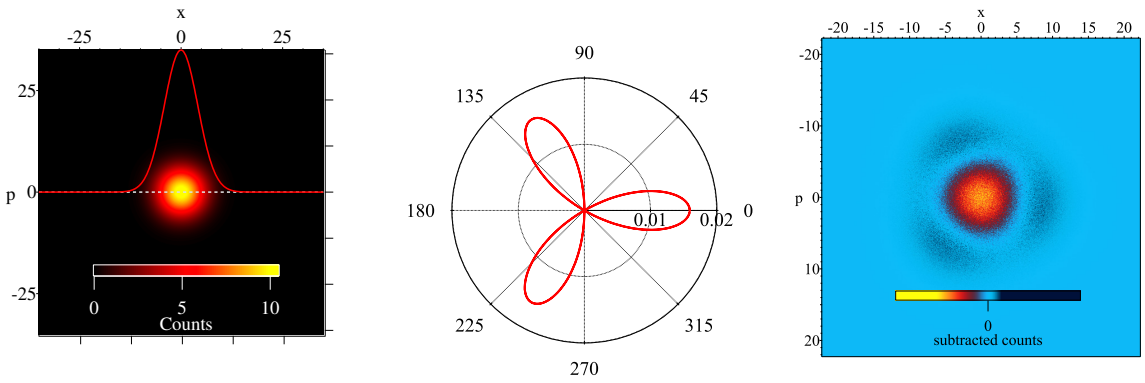

Figure 6.2: The phase space distribution of single-mode trisqueezed state at low output power ($F = 1.16$). (left) The 2D histogram of the x and p quadrature. Different from the high power case in Fig. 6.1, the star-like profile of the state is largely obscured by the system noise. (middle) γ_ϕ. We again extract the three-fold symmetry of the state, even though the system noise is overwhelmingly large. (right) ON-OFF subtracted histogram. Also showing the three-fold symmetry of the state.

6.3.2 Wigner functions of single-mode trisqueezed states

Having demonstrated the non-Gaussian character of the single-mode trisqueezed states, we move on to investigate if the states are indeed nonclassical. One well-accepted method is to check if the Wigner function of the state contains some negative regions. This property is often referred to as "Wigner negativity" [70, 71]. However, the reconstruction of Wigner functions in microwave quantum optics is, in general, a challenging task, due to the lack of a single photon detector and the inevitable added noise from linear amplifiers.

Following [7], we can derive a general expression for the Wigner function under the single-mode approximation (see section 3.4),

$$W(\alpha) = \sum_{n,m} \int d^2\lambda \frac{\left\langle \left(\hat{a}^\dagger\right)^n \hat{a}^m \right\rangle (\lambda^*)^n \lambda^m}{\pi^2 n! m!} e^{-\frac{1}{2}|\lambda|^2 + \alpha\lambda^* - \alpha^*\lambda}, \tag{6.8}$$

where $\alpha = x + ip$ is the complex coordinate of the Wigner function. This expression is particular useful as it depends only on the moments of the bosonic operators of the state, which can be measured with a linear amplifier.

While we have the states for reconstruction, it is inevitably contaminated by amplifier noise. To remove the noise, we will perform an ON-OFF measurement of the moments to correct for the amplifier noise. We can start by connecting the moment terms of the input and output bosonic operators of the amplifier chain using Eq. (3.5). Assuming a large system gain, $G - 1 \approx G$,

$$\left\langle \left(\hat{A}^\dagger\right)^n \hat{A}^m \right\rangle_\rho = G^{\frac{n+m}{2}} \sum_{i,j=0}^{n,m} \binom{m}{j} \binom{n}{i} \left\langle \left(\hat{a}^\dagger\right)^i \hat{a}^j \right\rangle \left\langle \hat{h}^{n-i} \left(\hat{h}^\dagger\right)^{m-j} \right\rangle \quad \text{Pump ON} \tag{6.9}$$

$$\left\langle \left(\hat{A}^\dagger\right)^n \hat{A}^m \right\rangle_{|0\rangle\langle 0|} = G^{\frac{n+m}{2}} \left\langle \hat{h}^n \left(\hat{h}^\dagger\right)^m \right\rangle \quad \text{Pump OFF.} \tag{6.10}$$

The first equation describes the relation of moments for a general state at the input and output of the amplifier chain. We see that the measured signal always contains the system noise.

We can invert Eq. (6.9) with the noise moments obtained from Eq. (6.10) and iteratively reconstruct the moment terms of the signal $\left\langle \left(\hat{a}^\dagger\right)^i \hat{a}^j \right\rangle$. In practice, the uncertainty in the reconstructed moments increase with their orders, thus, limiting the order we can reliably reconstruct.

Maximum likelihood method using the moment matrix

In principle, we could directly reconstruct the Wigner function from the moments, however, noise in the measurement can make it unreliable, e.g. making the reconstructed state unphysical. Therefore, it is common to use a maximum likelihood method that smooths out the effects of noise. Following [72], we can maximize the likelihood function

$$\mathcal{L} = -\sum_{n,m} \frac{1}{\sigma_{n,m}^2} \left| \left\langle \left(\hat{a}^\dagger\right)^n \hat{a}^m \right\rangle - \mathrm{Tr}\left[\rho \left(\hat{a}^\dagger\right)^n \hat{a}^m\right] \right|^2 \tag{6.11}$$

with respect to the elements of the density matrix ρ. As physical constraints, we require ρ to be Hermitian, positive semi-definite, and to have a trace of one. As we are working with a truncated Fock space, we also verify that the expectation value of the bosonic commutator is one, i.e. $\mathrm{Tr}\left(\rho\left[\hat{a}, \hat{a}^\dagger\right]\right) = 1$.

6.3.3 Wigner function of a weak star state

The moment matrix of a single-mode trisqueezed state tends to quickly increase in size with increasing F, such that the Wigner function reconstruction will need to take into account moment terms of higher order. Thus, it is preferable to start reconstructing the Wigner function for a weaker trisqueezed state where the higher order terms are less significant and can be neglected. Using an example with $F = 1.16$, the magnitude of the moment terms are given by the following matrix (showing terms up to the fifth order, illustrated by Fig. 6.3),

$$\left|\left\langle \left(\hat{a}^\dagger\right)^n \hat{a}^m \right\rangle\right| = \begin{pmatrix} 1 & 0.00 & 0.00 & 4.11 & 0.28 & 7.70 \\ 0.00 & 1.16 & 0.02 & 0.29 & 79.58 & \\ 0.00 & 0.02 & 16.02 & 1.68 & & \\ 4.11 & 0.29 & 1.68 & & & \\ 0.28 & 79.58 & & & & \\ 7.70 & & & & & \end{pmatrix},$$

with the error of the moments given by

$$\sigma_{n,m} = \begin{pmatrix} 0.00 & 0.00 & 0.01 & 0.05 & 0.55 & 7.91 \\ 0.00 & 0.01 & 0.03 & 0.33 & 3.69 & \\ 0.01 & 0.03 & 0.36 & 2.29 & & \\ 0.05 & 0.33 & 2.29 & & & \\ 0.55 & 3.69 & & & & \\ 7.91 & & & & & \end{pmatrix}.$$

The moment matrix exhibits the interesting features of the trisqueezed state. First, we notice that the degree of second order coherence is defined by $g^{(2)}(0) = \frac{\left\langle \hat{a}^\dagger \hat{a}^\dagger \hat{a} \hat{a} \right\rangle}{\left\langle \hat{a}^\dagger \hat{a} \right\rangle^2} \approx 11.8 > 2$. This indicates superbunching beyond that of a thermal state. Second, we notice that terms are significant only when the difference in the moment order $|n - m|$ is an integer multiple of three (see Fig. 6.3). This suggests the generation of photon triplets, such that the signal predominately contains Fock states that are a multiple of 3, i.e. $|3n\rangle$.

From Eq. (6.8), the moments are divided by $n!m!$ reflecting the normalization in Eq. (6.8). We can therefore refer to the reduced matrix $\left|\left\langle \left(\hat{a}^\dagger\right)^n \hat{a}^m \right\rangle\right| / n!m!$ to see if the moments converge so we can truncate the reconstruction to the lower order terms. We

visualized the reduced matrix by the 3D bar chart in Fig. 6.3 and see that the terms diverge. This leads to convergence problems for a direct reconstruction, which are greatly exacerbated by noise.

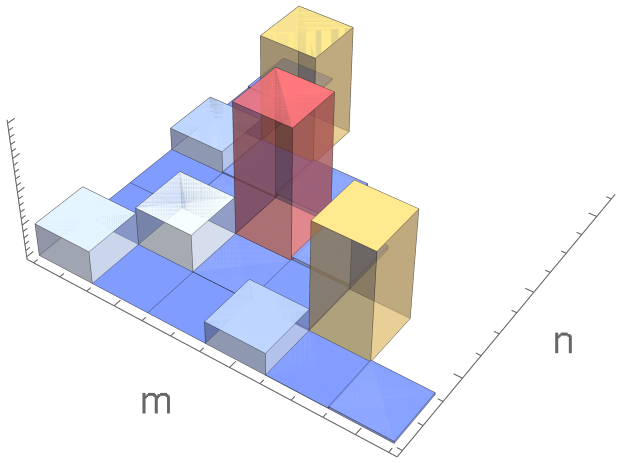

Figure 6.3: The moment matrix of a single-mode trisqueezed state divided by $n!m!$ at $F = 1.16$. The significant terms increase with higher order, even after the division by $n!m!$, suggesting possible convergence problems.

Reconstructed density matrix and Wigner function

To smooth out the noise, we apply the maximum likelihood method. With the help from our theory collaborators, we obtained the density matrix and the Wigner function of the $F = 1.16$ single-mode trisqueezed state data, shown in Fig. 6.4. Similar to the moment matrix, the density matrix entries show significant amplitudes only when $|n - m|$ is an integer multiple of three. This again suggests the creation of photon triplets. Meanwhile, the Wigner function clearly shows the triangular, star-shaped profile predicted by the theory. We also observe negativity in the Wigner function indicating that the reconstructed state is nonclassical.

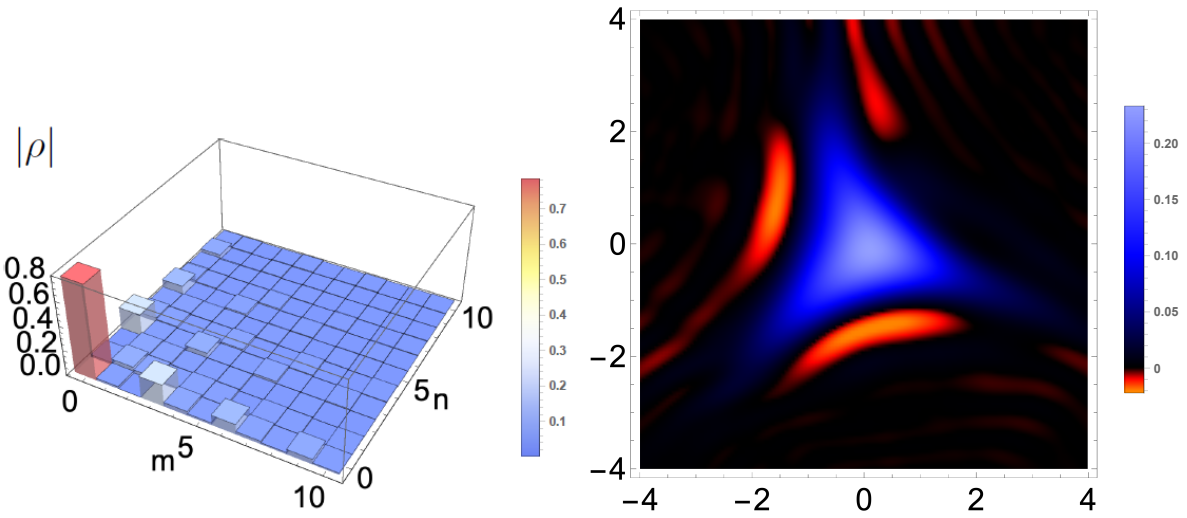

Figure 6.4: Reconstructed density matrix and Wigner function for a single-mode trisqueezed state. Figure courtesy of Fernando Quijandria. (left) Density matrix reconstructed from the trisqueezed state data. Significant amplitude is observed in terms with $|n - m|$ being an integer multiple of three. The amplitude decreases monotonically from the origin. (right) The reconstructed Wigner function. It shows the predicted triangular star-shaped profile, with amplitude peaked at the origin. Negativity is observed, as expected.

With the brighter trisqueezed states, the maximum likelihood method using moment matrices is becoming more numerically intensive and, thus, is not practical. A method that works with more photons will be needed for further analysis of brighter single-mode trisqueezed states.

6.4 Multimode trisqueezed state

In this section, we move on to study the two-mode and three-mode three-photon SPDC achievable with our device. Similarly, we will refer the output signals generated as two-mode and three-mode trisqueezed states. Similar to the single-mode state, the multimode states can be produced by the appropriate choice of the pump frequency, naturally given by the conservation of energy (see Table. 6.1). As observed in the single-mode case, we expect significant third-order statistics in the output states, thus, we characterize the two-mode and three-mode trisqueezed states statistically using the so-called coskewness of A, B and C defined as $\gamma_{ABC} = \frac{\overline{ABC}}{\sigma_A \sigma_B \sigma_C}$, now assuming the measurements are mean-zero. We can associate this statistical measure with the three-point quantum correlators $\left\langle \hat{A}\hat{B}\hat{C} \right\rangle$, where A, B and C are some quadratures of the multimode trisqueezed states. In the following, we will use angle brackets with quantum operators, e.g. $\langle \hat{A} \rangle$, to denote expectation values; and angle brackets with variables, e.g. $\langle A \rangle$, to denote time averages.

6.4.1 Measurement setup of multimode trisqueezed states

We performed correlation measurements for both two-mode and three-mode trisqueezed states. In the two-mode case, the amplified output signal from the cavity was split into two paths. The two frequency modes were simultaneously measured using two digitizers. In the three-mode case, we split the output signal into three paths and simultaneously digitized all three modes. This is different from the pair-wise measurements performed for the tripartite entangled states as described in section 4.5. All measurements were taken by sampling at 1 MHz, and each trigger lasts for one second.

6.4.2 Correlations in multimode trisqueezed states

Motivated by the standard two-photon SPDC, we started analysing the data by looking for covariance between each pair of modes in the trisqueezed states. However, we observed no covariance between any pair of the modes in either the two-mode or three-mode case, as shown in Fig. 6.6. Instead, we observed significant coskewness between the signals (see Fig. 6.6 and 6.5). To verify that the observed coskewness was a coherent process due to the pump, we swept the pump phase while we measured the covariance and coskewness, as shown in Fig. 6.6. The coskewness oscillated with the pump phase as a sinusoid, while covariances stayed at zero. The observation of coskewnesss (three-body interactions) in

the absence of covariance (two-body interactions) is a strong indication of non-Gaussian statistics in the multimode trisqueezed states.

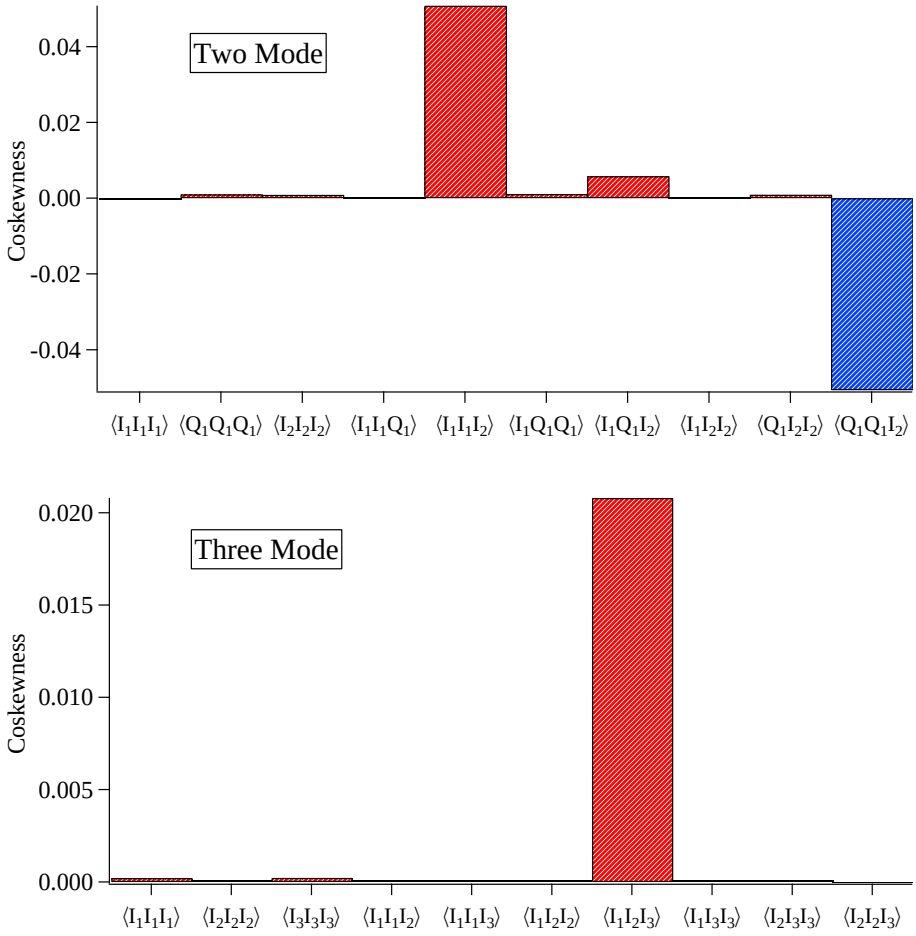

Figure 6.5: Measured coskewness in (top) the two-mode case and (bottom) the three-mode case. In the two-mode case, we considered the three quadratures I_1, Q_1 and I_2 as the representative samples. We expected the significant terms to include mode 1 twice and mode 2 once. This is matched by our data. We empirically adjusted the pump phase until only $\langle I_1 I_1 I_2 \rangle$ and $\langle Q_1 Q_1 I_2 \rangle$ are significant. The small amplitude at $\langle I_1 Q_1 I_2 \rangle$ is caused by a phase mismatch between the pump and digitizers in the experiment. In the three-mode case, we consider the I quadratures of all three modes. As expected, the only nonzero term includes all three modes, i.e. $\langle I_1 I_2 I_3 \rangle$, clearly indicated by the data.

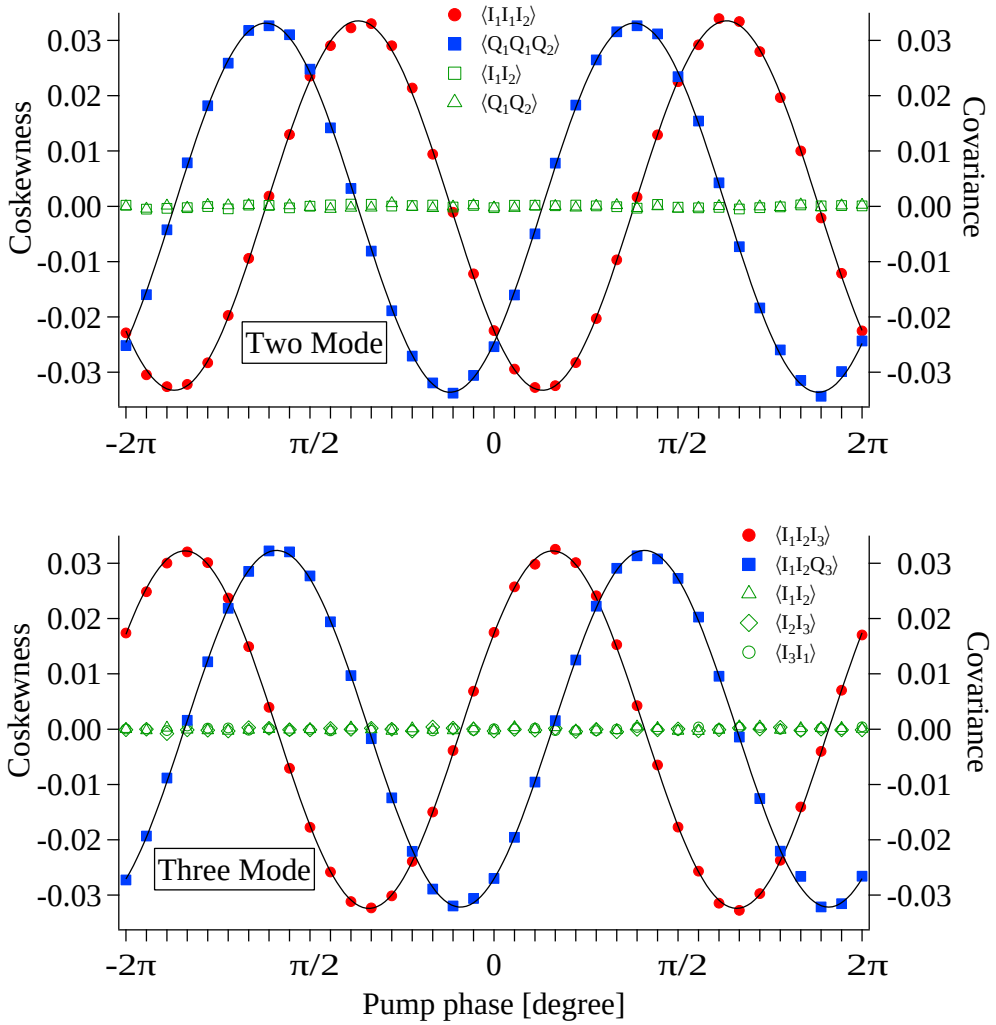

Figure 6.6: Covariance and coskewness of three-photon SPDC to (top) two modes and (bottom) three modes measured at room temperature. In the two-mode case, we have a degeneracy between two of the three generated photons. This leads to one mode participating twice in the nonzero coskewness term. For our choice of pump phase, the only significant coskewness terms are then $\langle I_1 I_1 I_2 \rangle$ and $\langle Q_1 Q_1 I_2 \rangle$. In the three-mode case, the only nonzero coskewness term must contain all three modes, e.g. $\langle I_1 I_2 I_3 \rangle$. To demonstrate that the observed coskewness is a coherent process due to the pump, we sweep the pump phase from -2π to 2π and observe the effect. The data shows a clear oscillation in the coskewness and the oscillations fit well to a sinusoid. Conversely, all covariance terms are essentially zero throughout the sweep, suggesting that the states do not contain second-order correlations.

With a maximum of three modes, and thus six quadratures, there exist a number of two-mode and three-mode coskewness statistics that we can compute. Fig. 6.5 shows many of them. In the two-mode case, there is a degeneracy between two of the three generated photons, as two photons will go to one of the modes. We therefore expect that only terms, such as $\langle I_1 I_1 I_2 \rangle$, where one mode participates twice in the coskewness, will be nonzero. Meanwhile, in the three-mode case, where one photon goes to each mode, we expect that the only nonzero coskewness terms should contain all three modes, e.g., $\langle I_1 I_2 I_3 \rangle$. This is observed in Fig. 6.5.

6.4.3 Structure of correlation in multimode trisqueezed states

To learn the structure of the three-body correlation in the multimode trisqueezed states, we now generalize the phase analysis used in Fig. 6.1. We take the transformations to study the set of symmetry operations of an N-mode Gaussian state. These form the symplectic group and are generated by quadratic Hamiltonians. The symplectic group includes squeezing operations which create or destroy photons, but we will limit ourselves to the passive operations which conserve photon numbers. These operations form a unitary subgroup and include phase rotations of a single mode, with generators such as $\hat{a}_i^\dagger \hat{a}_i + \hat{a}_i \hat{a}_i^\dagger$, and beam-splitter rotations between modes, with generators such as $\hat{a}_i^\dagger \hat{a}_j + \hat{a}_i \hat{a}_j^\dagger$. Importantly, we expect different trisqueezing Hamiltonians (see section 6.2.1) to have different transformation properties under these operations.

With six quadratures, we have a six-dimensional phase space to explore. The symplectic operations can then be represented by 6×6 matrices. In order to illustrate the transformation properties using a 3D figure, we project into a three-quadrature subspace. The transformations then become generalized rotations between the three selected quadratures. Collecting the quadratures into a 3-vector, we can explore arbitrary combinations of the quadratures by applying a series of two rotations according to

$$(A', B', C')^t = R_Z(\phi) \times R_Y(\theta) \times (A, B, C)^t \,, \tag{6.12}$$

where R_i are standard 3D rotation matrices with the rotation axis specified by the subscript, given by

$$R_Y(\theta) = \begin{pmatrix} \cos\theta & 0 & \sin\theta \\ 0 & 1 & 0 \\ -\sin\theta & 0 & \cos\theta \end{pmatrix}$$

and

$$R_Z(\phi) = \begin{pmatrix} \cos\phi & -\sin\phi & 0 \\ \sin\phi & \cos\phi & 0 \\ 0 & 0 & 1 \end{pmatrix}.$$

After the rotations, we consider the generalized quadrature

$$A_{\phi\theta} = \cos(\phi)\cos(\theta)A - \sin(\phi)B + \cos(\phi)\sin(\theta)C, \tag{6.13}$$

and compute its skewness $\gamma_{\phi\theta}$ which in general is a mix of all of the possible three-point correlators of the three quadratures. Generalizing the one-mode case, we can think of $\gamma_{\phi\theta}$ representing the asymmetry of the 3D distribution of measured quadratures with respect to the symmetry plane perpendicular to the direction of $\hat{A}_{\phi\theta}$.

In Fig. 6.7, we show spherical plots of γ as a function of $\theta \in [0, \pi]$ and $\phi \in [0, 2\pi]$ for both the two-mode and three-mode case. Explicitly, for the two-mode case, we chose $A = I_1, B = Q_1$ and $C = I_2$. The transformation specified by Eq. (6.12) is then first a beam-splitter rotation by θ between mode 1 and mode 2, followed by a phase rotation of mode 1 by ϕ (which mixes I and Q). In the three-mode case, we have $A = I_1, B = I_2$ and $C = I_3$, such that Eq. (6.12) describes two beam-splitter rotations among the three modes, first coupling mode 1 and mode 3 and then modes 1 and 2. Fig. 6.7 shows the experimental results for $\gamma_{\phi\theta}$ along with theoretical predictions for the states produced by the multimode trisqueezing Hamiltonian $\hat{H}_{2M}$ and $\hat{H}_{3M}$ in section 6.2.1. The agreement between theory and experiment is very good. We observe that different processes produce very different profiles for $\gamma_{\phi\theta}$, which essentially fingerprints the underlying Hamiltonians and allow us to see in a clear, visual way how cleanly we generate one Hamiltonian compared to another. We can now connect the features in the 3D figures to the correlation structure of the multimode trisqueezed states.

Starting with the three-mode trisqueezed state, consider Fig. 6.7d. The first important feature is that $\gamma_{\phi\theta}$ has nodes in the three XY, YZ ad ZX-planes. We can understand the presence of these nodes by noticing that in these planes at least one of the modes is excluded from the generalized quadrature $A_{\phi\theta}$. This indicates that two-mode correlators such as $\langle {I_1}^2 I_2 \rangle$ and single-mode correlators such as $\langle {I_1}^3 \rangle$ are zero. Exactly as we would expect for a state generated by the pure three-mode trisqueezing Hamiltonian $\hat{H}_{3M}$. Conversely, the antinodes (lobes) correspond to the angles where the contribution of the three-mode correlator $\langle I_1 I_2 I_3 \rangle$ are maximized. Therefore, the pattern tells us that we have both activated $\hat{H}_{3M}$ and not activated $\hat{H}_{1M}$ nor $\hat{H}_{2M}$. This is also a clear indication that we are observing genuine three-mode interference.

The structure of two-mode trisqueezed state can be understood in a similar way. Recall that for the specific choice of pump frequency (see section 6.2.1), we expect that we are creating two photons in mode 1 and one photon in mode 2. Referring to Fig. 6.7a, we can then consider the behaviour in the ZX-plane, also highlighted in Fig. 6.7c. It shows clear nodes at $\theta = 0(\pi/2)$, where we are calculating the skewness of I_1 (I_2) alone. This is in agreement with our expectations from Fig. 6.5. Instead $\gamma_{\phi\theta}$ is at maximum around $\theta = \pi/4$ and $\theta = 3\pi/4$, where I_1 and I_2 are maximally contributed from the two-mode correlator $\langle {I_1}^2 I_2 \rangle$. As above, these fingerprints clearly indicate that we are now activating $\hat{H}_{2M}$ but not $\hat{H}_{1M}$, with two photons generated in mode 1. We note that the expected lobes at $\theta = 5\pi/4$ and $\theta = 7\pi/4$ are missing at first glance, but in fact they overlap the lobes at $\theta = \pi/4$ and $\theta = 3\pi/4$ as the sign of $\gamma_{\phi\theta}$ becomes negative. The structure in the XY-plane can be explained in a similar way, except then we are mixing Q_1 and I_2.

While we can create more of these projections of the 6D phase space into 3D, it is already clear from these two examples that the structure of $\gamma_{\phi\theta}$ is a useful way to characterize the multimode trisqueezed states. In particular, with a library of the possible fingerprints generated by different trisqueezing Hamiltonians, we can efficiently identify what is generating the observed state by comparing the 3D figures. By observing the relative depth of nodes (3×10^{-6} for three-mode case) compared to the antinodes (0.024), with a ratio greater than 1000 we can also appreciate how purely we generate just a single member of the trisqueezing Hamiltonian family.

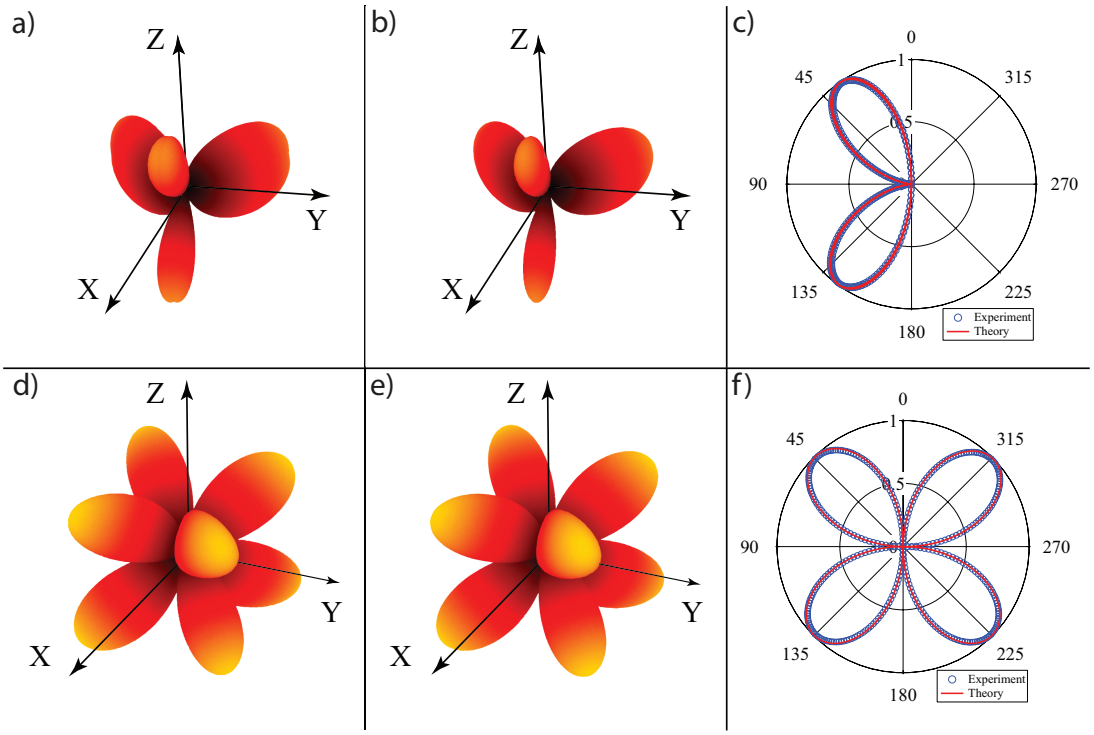

Figure 6.7: Third-order correlation analysis of multimode trisqueezed states. Row 1 and 2 show results for, respectively, the two-mode and three-mode trisqueezed states, generated by $\hat{H}_{2\mathrm{M}}$ and $\hat{H}_{3\mathrm{M}}$. The spherical plots show $\gamma_{\phi\theta}$, which is the skewness of the generalized multimode quadrature $A_{\phi\theta}$ (see (6.13)), which mixes the mode quadratures through symplectic symmetry operations. The 6D phase space of the three modes are projected into a 3D space for the purposes of visualization. Generally, $\gamma_{\phi\theta}$ combines the contributions of the skewness and coskewness of the three modes involved in each case. a) Experimental data for the two-mode case. b) The theoretical prediction for $\hat{H}_{2\mathrm{M}}$. The clear agreement shows that the observed state is generated by that specific Hamiltonian. c) A plane-cut of the spherical plots through the ZX-plane. The curves are normalized, but otherwise the theory has no adjustable parameters. There are no lobes apparent on the right half of the plot as $\gamma_{\phi\theta}$ is negative for $\phi \in [\pi/2, 3\pi/2]$, causing these lobes to overlap those of $\phi \in [-\pi/2, \pi/2]$. d) Experimental data for the three-mode case. e) The theoretical prediction for $\hat{H}_{3\mathrm{M}}$. f) A plane-cut at $\phi = +35$ degrees from the ZX-plane. Again, we see a clear agreement between the observed state and the target Hamiltonian. In particular, the antinodes (lobes) of $\gamma_{\phi\theta}$ appear only at angles where all three modes are mixed, as expected from a genuine three-mode interference.

6.4.4 Correlation feed-forward

Currently, we have observed a radically different correlation structure from trisqueezed states. Compared to the conventional two-photon squeezed states, trisqueezed states exhibit strong third-order correlation (coskewness) with the absence of second-order correlation (covariance). The result seems to suggest that these output states from three-photon SPDC appear to be disconnected from the ordinary two-photon squeezed states. Here, we want to explore the relationship between the two.

Recovery of second-order correlation by seeding

An interesting experimental observation in this direction is that, while the three-mode trisqueezed state does not show covariance between any pair of modes when starting from a vacuum state, by seeding one of the three modes with a weak coherent tone, the noise power emitted from the other modes is enhanced and that it then has nonzero covariance. Similarly, in the two-mode trisqueezed state, by seeding the mode participating only once, i.e. mode 2, we observe the emission of squeezed noise from the other mode. These results can be understood from the point of view of dynamical constraints imposed by the conservation of energy. In the standard two-photon case, signal and idler photon pairs are constrained to have a symmetric detuning around $\omega_p/2$. In the rotating frame at $\omega_p/2$, the phasors of the signal and idler photons process at the same frequency but in opposite directions, such that the axis (phase) of the sum phasor is stationary in time and the same for all pairs. This gives rise to the observed covariance between the signal and idler modes. Now, in the three-photon case, we have three free frequencies (energies). This extra degree of freedom washes out the two-mode correlations. Seeding one mode effectively fixes one photon frequency in the resulting stimulated emission, establishing a fixed relation between the other two. This produces correlations similar to two-photon SPDC.

This argument suggests that by having information about one mode, it should be possible to reveal the second-order correlations of the remaining modes. That is, by conditioning our measurement of the remaining modes on the measurement of the first "reference" mode, we should be able to recover a conditional distribution with two-mode correlations.

Correlation feed-forward protocol

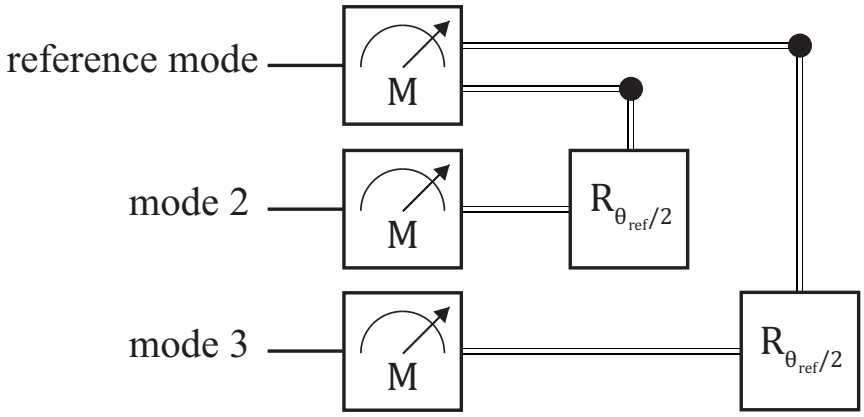

Figure 6.8: A cartoon for the correlation feed-forward protocol for the three-mode trisqueezed state. This scheme tests our hypothesis on the conditional structure of two- and three-mode correlations. In the three-mode protocol shown here, we first measure the local phase of the reference mode (mode 1 in this example), followed by applying a rotation by $\theta_{ref}/2$ on the other two modes. The result is an observable correlation between mode 2 and mode 3 with the characteristic structure of two-photon SPDC, i.e. two-mode downconversion.

Three-mode correlation feed-forward

To test our hypothesis, we developed a protocol named "correlation feed-forward" to demonstrate the recovery of a second order correlation from the three-mode trisqueezed state data. First, from the three modes, we select the reference mode and estimate its local phase from the digitized signal. This is done for every sample period using the standard relation $\theta_{\text{ref}} = \arctan(Q_{\text{ref}}/I_{\text{ref}})$. The data used was acquired with the same configuration as the earlier coskewness analysis (see section 6.4.1). Then, we rotate the quadratures of the remaining modes using θ_{ref}, as illustrated in Fig. 6.8. The action of the phase rotation can again be explained by energy conservation: as the frequencies of the three photons must sum to ω_p, a small frequency shift ($\delta\omega_p$) from the center in the reference mode needs to be compensated by changes in the other two modes. In our example with the three-mode case, we used mode 1 as the reference and applied rotations by $\theta/2$ to modes 2 and modes

3. Table II shows the resulting correlation recovered. We see that the correlation structure is the same as TMDC.

	Feed-forward			
	Yes		No	
Quads	Pump On	Pump Off	Pump On	Pump Off
I_2I_3	0.30 ± 0.02	0.00 ± 0.02	0.00 ± 0.02	0.00 ± 0.02
Q_2Q_3	-0.30 ± 0.02	0.00 ± 0.02	0.00 ± 0.02	0.00 ± 0.02
I_2Q_3	-0.36 ± 0.02	0.00 ± 0.02	0.00 ± 0.02	0.00 ± 0.02
Q_2I_3	-0.36 ± 0.02	0.00 ± 0.02	0.00 ± 0.02	0.00 ± 0.02

Table 6.2: The resultant two-mode correlation coefficient (normalized covariance) between mode 2 and mode 3 after applying correlation feed-forward to the three-mode trisqueezed state (see Fig. 6.8). As shown, we recover a significant amount of second-order correlation when applying our feed-forward correction.

Two-mode correlation feed-forward

We also applied the correlation feed-forward protocol to the two-mode trisqueezed state. We selected mode 2 as our reference with the hope of seeing two-photon interference in mode 1. To see the effect of correlation feed-forward protocol on mode 1, we make a histogram of the corrected quadratures. Fig. 6.9 shows the resulting histogram after subtracting the system noise histogram. We can clearly see a stretching of the distribution along the $\hat{x}$ quadrature, indicating squeezing-like correlations. We find the ratio in the variance of $\hat{x}$ to $\hat{p}$ to be 1.110 ± 0.007 for the output with pump on, compared to 1.000 ± 0.002 for the control output with pump off.

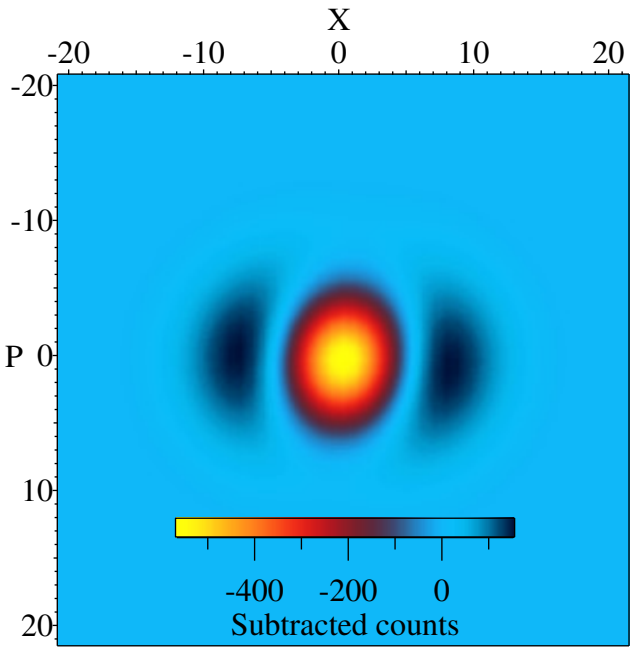

Figure 6.9: The resultant single-mode histogram of mode 1 after applying correlation feed-forward to the two-mode trisqueezed state. We take mode 2 as the reference mode, correcting the phase of mode 1. We have subtracted the system noise histogram. We clearly see that the subtracted histogram is stretched along the x-axis, indicating squeezing of the ON state. The small rotation of the figure can be explained by a small amount of coskewness in $\langle I_1 Q_1 I_2 \rangle$ due to an imperfect configuration of the pump and digitizer phases (see Fig. 6.5).

These results validate our hypothesis about the conditional structure of two-mode and three-mode correlations in our system. Meanwhile, the correlation feed-forward demonstrations here are only proof-of-principles, as our measured phase is contaminated by the system noise. Future work can further explore the fundamental limit of this reconstruction method.

Conclusion

In this thesis, we studied two-photon and three-photon parametric interactions through a series of experiments. We focused on analysing the outputs from spontaneous parametric downconversion processes which are generated by our flux-pumped SQUID-terminated superconducting cavity resonator.

We began by describing the design and working principles of our flux-pumped cavity resonator. Based on the conventional SQUID-terminated CPW resonator structures, we have explored various novel designs in an effort of making a device better fit our objectives. We implemented the stepped-impedance resonator design following [8] and achieved an anharmonicity of 600 MHz which allowed the highly selective activations of parametric processes. In order to achieve sufficient pump strength for driving three-photon downconversion, we improved the pump coupling by exploiting the kinetic inductance of a superconducting nanowire incorporated it into the SQUID. With this new design, we obtained a 30 dB increase in coupling strength.

Next we described the measurement system. We discussed the microwave environment and went through the details on device mounting, shielding and cabling in the cryostat. Then, we demonstrated an absolute system calibration technique using a SNTJ to extract the system noise, system gain and the input-state temperature. We demonstrated a low input-state temperature of 25 mK, which puts our device deep in the quantum regime. The accuracy of the system calibrated was shown to be critical to our demonstrations of entanglement and quantum-enhanced sensing.

Having introduced the device and the measurement environment, we moved on to experimentally study two-photon parametric processes. We started by reviewing the essential theory behind two-mode downconversion and coherent coupling. We motivated the discussion by analysing a simplified classical bound of entanglement, derived from the variance and covariance of the signals' quadrature amplitudes. Then, we introduced a more sophisticated method using the positive partial-transpose (PPT) criterion. We illustrated the use of these test by demonstrating two-mode entanglement generation from the device

over a range of output power. Then, we extend our two-mode entanglement to tripartite entanglement of three modes by simultaneously performing two two-photon processes. We studied the effective interactions brought by the two-tone pumping, proposing two schemes for tripartite entanglement generation. We then went through two tripartite entanglement verification methods. We first extended the PPT criterion to three modes, testing the output for full inseparability. We then introduced the test for genuine tripartite entanglement. Finally, we demonstrated that our experimental results from both schemes exhibited both full inseparability and genuine tripartite entanglement.

We next explored an application of TMDC for long-range quantum sensing, developing and testing a protocol we named quantum-enhanced noise radar. In the protocol, the output beams from a TMDC process acts as the radiation source of a noise radar. To benchmark the TMDC beams against its classical counterpart, we designed a classical source which generates two-mode correlated beams with the same correlation structure of TMDC. We measured its performance and observed that its correlation saturated the classical bound. Thus it represents the ideal classical source of correlated beams. Then, we developed a measurement method which allowed us to directly compare the two cases without system calibration. We observed that the quantum beams provides higher raw covariance then the classical beams under the same influence of ambient noise and transmission loss. Further, we developed the quantity of quantum enhancement as a ratio of the covariance of the quantum and classical beams. We clearly observed an improvement in the signal-to-noise ratio using the quantum source over the classical source. Finally, we developed a simple expression for quantum enhancement by assuming a perfect TMDC process and ideal classical source. The expression fits very well to the experimental data, and the extracted system gain agreed very well with the independently calibrated gain from SNTJ.

In the final chapter, we took a step forward to visit the unexplored territory of three-photon parametric interactions. We began by describing the necessary modification of the standard SQUID design in order to access three-photon interactions. We analysed the expected, weaker interaction strength in the higher order process, which justified the need for our improvement in pump coupling. We listed five three-photon interactions achieved with our device, and we focused our discussion on analysing the output of the three three-photon SPDC processes, which we referred to as trisqueezing processes. In single-mode three-photon SPDC, we analysed the statistical property of the single-mode trisqueezed state generated and observed very clear signature of three-point correlation. This was indicated by the strong skewness in the quadrature amplitude of the signal, observed from across a broad range of average output photon flux. This shows that the state is non-Gaussian. We further analysed the state for nonclassicality using a Wigner-function

reconstruction approach proposed by [7]. From a weak trisqueezed state, we reconstructed the moment matrix and observed traces of photon triplet generations. We applied a maximum likelihood reconstruction and obtained the a density matrix and Wigner function of the single-mode trisqueezed state. We observed clear negativity in the Wigner function, indicating that we have generated a propagating nonclassical state by three-photon downconversion. Moving on to the multimode case, we analyse the correlation structure of the two-mode and three-mode trisqueezed states. We observe that they carried significant three-point correlations with a distribution that agrees well with theoretical predictions. Further, we studied the effect of a set of symmetry operations performed on the states, drawn from the passive operations of the symplectic. In this way, we visualized the correlation structure of the states with 3D spherical plots and compared that to the theoretically expected outcomes. We found very good agreement between the experimental data and theory. Finally, we developed a protocol based on the multiple trisqueezed states called correlation-feedforward. It suggests a relationship between the three-photon and two-photon SPDC outputs. Through the protocol, two-photon correlations can be recovered from the three-photon state by means of a feedforward of measurement results. In our proof-of-principle experiments, we demonstrated the recovery of two-mode correlation from a three-mode trisqueezed state, as well as an observation of squeezing in a single-mode state recovered from a two-mode trisqueezed state. These connections are interesting from a fundamental point of view, as well as opening up the states for new potential applications like quantum metrology.

Future work

With the quantum-enhanced noise radar work, we are working towards realizing the protocol with an actual antenna setup. While we demonstrated that the quantum beams are superior to the classical beams, the current measurements are done all inside the cryostat. In order to utilize the signal for detection, we need to route the signal out of the cryostat without amplifications. This can be achieved by using circulators over multiple temperature stages to direct the signal out while isolating the device from thermal photons. Performing the experiment will allow us to demonstrate the QENR protocol in real-life and stimulate further research from the field of noise radar. With our single-mode three-photon SPDC results, we are currently limited to analysing nonclassicality with weak trisqueezed states. This is due to the demanding computational power needed by the maximum likelihood method for our states. We are working closely with the theorists to testing other reconstruction method which work better for higher power states. On the multimode

trisqueezed states, we want to further test the states for possible nonclassicality like non-Gaussian tripartite entanglement. This requires more work on the theoretical side and we are actively working with collaborators on this. We believe our results will inspire novel work in quantum optics which will be beneficial to the quantum information community and the long-term development of universal quantum computers.

Letter of Copyright Permission

Use of material from Ref. [73] is covered by American Physical Societys (APS) standing rules on their Physical Review journals of which, for the purpose of use of an article in a thesis where the thesis author is also the author of said article, Yes, the author has the right to use the article or a portion of the article in a thesis or dissertation without requesting permission from APS, provided the bibliographic citation and the APS copyright credit line are given on the appropriate pages.

References

[1] Y. Nakamura, Yu A. Pashkin, and J. S. Tsai. Coherent control of macroscopic quantum states in a single-Cooper-pair box. *Nature*, 398(6730):786–788, 4 1999.

[2] P. Forn-Díaz, J.J. García-Ripoll, B. Peropadre, J.-L. Orgiazzi, M.A. Yurtalan, R. Belyansky, C.M. Wilson, and A. Lupascu. Ultrastrong coupling of a single artificial atom toan electromagnetic continuum in the nonperturbative regime. *Nature Physics*, 13(1):39–43, 1 2017.

[3] J. R. Johansson, G. Johansson, C. M. Wilson, and Franco Nori. Dynamical Casimir effect in superconducting microwave circuits. *Physical Review A - Atomic, Molecular, and Optical Physics*, 82(5):1–17, 2010.

[4] C. M. Wilson, G. Johansson, A. Pourkabirian, M. Simoen, J. R. Johansson, T. Duty, F. Nori, and P. Delsing. Observation of the dynamical Casimir effect in a superconducting circuit. *Nature*, 479(7373):376–379, 11 2011.

[5] J. R. Johansson, G. Johansson, and Franco Nori. Optomechanical-like coupling between superconducting resonators. *Physical Review A - Atomic, Molecular, and Optical Physics*, 90(5), 2014.

[6] Ali .C. Hardal, Nur Aslan, C. M. Wilson, and zgr E. Müstecapllolu. Quantum heat engine with coupled superconducting resonators. *Physical Review E*, 96(6):1–14, 2017.

[7] C. Eichler, D. Bozyigit, C. Lang, L. Steffen, J. Fink, and A. Wallraff. Experimental state tomography of itinerant single microwave photons. *Physical Review Letters*, 106(22):3–6, 2011.

[8] Eva Zakka-Bajjani, Franois Nguyen, Minhyea Lee, Leila R. Vale, Raymond W. Simmonds, and Jos Aumentado. Quantum superposition of a single microwave photon in two different 'colour' states. *Nature Physics*, 7(8):599–603, 2011.

[9] Jens Koch, Terri M. Yu, Jay Gambetta, A. A. Houck, D. I. Schuster, J. Majer, Alexandre Blais, M. H. Devoret, S. M. Girvin, and R. J. Schoelkopf. Charge-insensitive qubit design derived from the Cooper pair box. *Physical Review A - Atomic, Molecular, and Optical Physics*, 76(4):1–19, 2007.

[10] Lafe Spietz, K. Lehnert, I. Siddiqi, and R.J. Schoelkopf. The Shot Noise Thermometer: Primary Electronic Thermometry using the Noise from a Tunnel Junction. *2004 Conference on Precision Electromagnetic Measurements*, 300(5627):638–639, 6 2004.

[11] Lafe Spietz, R. J. Schoelkopf, and Patrick Pari. Shot noise thermometry down to 10mK. *Applied Physics Letters*, 89(18):183123, 10 2006.

[12] Luke C.G. Govia and Aashish A. Clerk. Enhanced qubit readout using locally generated squeezing and inbuilt Purcell-decay suppression. *New Journal of Physics*, 19(2), 2017.

[13] Nicolas Didier, Archana Kamal, William D. Oliver, Alexandre Blais, and Aashish A. Clerk. Heisenberg-Limited Qubit Read-Out with Two-Mode Squeezed Light. *Physical Review Letters*, 115(9):093604, 8 2015.

[14] W Tittel, J Brendel, H Zbinden, and N Gisin. Quantum Cryptography Using Entangled Photons in Energy-Time Bell States. *Physical Review Letters*, 84(20):4737–4740, 5 2000.

[15] N A Borshchevskaya, K G Katamadze, S P Kulik, and M V Fedorov. Three-photon generation by means of third-order spontaneous parametric down-conversion in bulk crystals. *Laser Physics Letters*, 12(11):115404, 11 2015.

[16] Mara Corona, Karina Garay-Palmett, and Alfred B. U'Ren. Third-order spontaneous parametric down-conversion in thin optical fibers as a photon-triplet source. *Physical Review A - Atomic, Molecular, and Optical Physics*, 84(3):1–13, 2011.

[17] M Akbari and A A Kalachev. Third-order spontaneous parametric down-conversion in a ring microcavity. *Laser Physics Letters*, 13(11):115204, 11 2016.

[18] Andrea Cavanna, Felix Just, Xin Jiang, Gerd Leuchs, Maria V. Chekhova, Philip St.J. Russell, and Nicolas Y. Joly. Hybrid photonic-crystal fiber for single-mode phase matched generation of third harmonic and photon triplets. *Optica*, 3(9):952, 2016.

[19] Vinay Ambegaokar and Alexis Baratoff. Tunneling Between Superconductors. *Physical Review Letters*, 10(11):486–489, 6 1963.

[20] J. Bardeen, L. N. Cooper, and J. R. Schrieffer. Theory of Superconductivity. *Physical Review*, 108(5):1175–1204, 12 1957.

[21] Theodore. Van Duzer and C. W. (Charles William) Turner. *Principles of superconductive devices and circuits*. Prentice Hall, 1999.

[22] W. Meissner and R. Ochsenfeld. Ein neuer Effekt bei Eintritt der Supraleitfhigkeit. *Die Naturwissenschaften*, 21(44):787–788, 11 1933.

[23] Carlos Sabín, Borja Peropadre, Lucas Lamata, and Enrique Solano. Simulating superluminal physics with superconducting circuit technology. *Physical Review A*, 96(3):032121, 9 2017.

[24] David M. Pozar. *Microwave Engineering*. John Wiley & Sons, 12 2012.

[25] FREDRIK PERSSON. *Fast readout of a single Cooper-pair box using its quantum capacitance*. PhD thesis, Chalmers University of Technology, 2010.

[26] M H Devoret, A Wallraff, and J M Martinis. Superconducting Qubits: A Short Review, 2004.

[27] B. R. Mollow and R. J. Glauber. Quantum Theory of Parametric Amplification. II. *Physical Review*, 160(5):1097–1108, 8 1967.

[28] H. Nyquist. Thermal agitation of. *Phys. Rev.*, 32(1918):110, 1928.

[29] E. Flurin, N. Roch, J. D. Pillet, F. Mallet, and B. Huard. Superconducting quantum node for entanglement and storage of microwave radiation. *Physical Review Letters*, 114(9):1–5, 2015.

[30] R. E. Slusher, L. W. Hollberg, B. Yurke, J. C. Mertz, and J. F. Valley. Observation of squeezed states generated by four-wave mixing in an optical cavity. *Physical Review Letters*, 55(22):2409–2412, 1985.

[31] Ling An Wu, H. J. Kimble, J. L. Hall, and Huifa Wu. Generation of squeezed states by parametric down conversion. *Physical Review Letters*, 57(20):2520–2523, 11 1986.

[32] David Edward Bruschi, Carlos Sabín, Pieter Kok, Gran Johansson, Per Delsing, and Ivette Fuentes. Towards universal quantum computation through relativistic motion. *Scientific Reports*, 6(September 2015):1–14, 2016.

[33] David Edward Bruschi, Carlos Sabín, and Gheorghe Sorin Paraoanu. Entanglement, coherence, and redistribution of quantum resources in double spontaneous down-conversion processes. *Physical Review A*, 95(6):062324, 6 2017.

[34] Samuel L. Braunstein and Peter van Loock. Quantum information with continuous variables. *Reviews of Modern Physics*, 77(2):513–577, 6 2005.

[35] Lu Ming Duan, G Giedke, J I Cirac, and P Zoller. Inseparability criterion for continuous variable systems. *Physical Review Letters*, 84(12):2722–2725, 3 2000.

[36] R. Simon. Peres-Horodecki Separability Criterion for Continuous Variable Systems. *Physical Review Letters*, 84(12):2726–2729, 3 2000.

[37] R. Simon, N. Mukunda, and Biswadeb Dutta. Quantum-noise matrix for multimode systems: U(n) invariance, squeezing, and normal forms. *Physical Review A*, 49(3):1567–1583, 3 1994.

[38] Gerardo Adesso and Fabrizio Illuminati. Gaussian measures of entanglement versus negativities: Ordering of two-mode Gaussian states. *Physical Review A*, 72(3):032334, 9 2005.

[39] Pasi Lähteenmäki, Gheorghe Sorin Paraoanu, Juha Hassel, and Pertti J. Hakonen. Coherence and multimode correlations from vacuum fluctuations in a microwave superconducting cavity. *Nature Communications*, 7(1):12548, 11 2016.

[40] G. Giedke, B. Kraus, M. Lewenstein, and J. I. Cirac. Separability properties of three-mode Gaussian states. *Physical Review A*, 64(5):052303, 10 2001.

[41] Peter van Loock and Akira Furusawa. Detecting genuine multipartite continuous-variable entanglement. *Physical Review A - Atomic, Molecular, and Optical Physics*, 67(5):13, 2003.

[42] S. Gerke, J. Sperling, W. Vogel, Y. Cai, J. Roslund, N. Treps, and C. Fabre. Multipartite Entanglement of a Two-Separable State. *Physical Review Letters*, 117(11):1–6, 2016.

[43] R. Y. Teh and M. D. Reid. Criteria for genuine N -partite continuous-variable entanglement and Einstein-Podolsky-Rosen steering. *Physical Review A - Atomic, Molecular, and Optical Physics*, 90(6):1–17, 2014.

[44] E. Shchukin and P. Van Loock. Generalized conditions for genuine multipartite continuous-variable entanglement. *Physical Review A - Atomic, Molecular, and Optical Physics*, 92(4):1–10, 2015.

[45] Seth Lloyd. Enhanced sensitivity of photodetection via quantum illumination. *Science (New York, N.Y.)*, 321(5895):1463–5, 9 2008.

[46] Si-Hui Tan, Baris I. Erkmen, Vittorio Giovannetti, Saikat Guha, Seth Lloyd, Lorenzo Maccone, Stefano Pirandola, and Jeffrey H. Shapiro. Quantum Illumination with Gaussian States. *Physical Review Letters*, 101(25):253601, 12 2008.

[47] S. Pirandola, B. R. Bardhan, T. Gehring, C. Weedbrook, and S. Lloyd. Advances in photonic quantum sensing. *Nature Photonics*, 12(12):724–733, 12 2018.

[48] Adrian J. Menssen, Alex E. Jones, Benjamin J. Metcalf, Malte C. Tichy, Stefanie Barz, W. Steven Kolthammer, and Ian A. Walmsley. Distinguishability and Many-Particle Interference. *Physical Review Letters*, 118(15):1–22, 2017.

[49] Zheshen Zhang, Maria Tengner, Tian Zhong, Franco N. C. Wong, and Jeffrey H. Shapiro. Entanglements Benefit Survives an Entanglement-Breaking Channel. *Physical Review Letters*, 111(1):010501, 7 2013.

[50] Duncan G. England, Bhashyam Balaji, and Benjamin J. Sussman. Quantum-enhanced standoff detection using correlated photon pairs. *Physical Review A*, 99(2):023828, 2 2019.

[51] Mikel Sanz, Kirill G. Fedorov, Frank Deppe, and Enrique Solano. Challenges in Open-air Microwave Quantum Communication and Sensing. In *2018 IEEE Conference on Antenna Measurements & Applications (CAMA)*, pages 1–4. IEEE, 9 2018.

[52] Marco Lanzagorta and Jeffrey Uhlmann. Virtual Modes for Quantum Illumination. In *2018 IEEE Conference on Antenna Measurements & Applications (CAMA)*, pages 1–4. IEEE, 9 2018.

[53] Matthew Brandsema. Current Readiness for Quantum Radar Implementation. In *2018 IEEE Conference on Antenna Measurements & Applications (CAMA)*, pages 1–4. IEEE, 9 2018.

[54] Krzysztof Kulpa. *Signal Processing in Noise Waveform Radar.* Artech House, 2013.

[55] James D. Taylor. *Advanced Ultrawideband Radar: Targets, Signals and Applications.* CRC Press, 2016.

[56] Kevin Marshall, Raphael Pooser, George Siopsis, and Christian Weedbrook. Repeat-until-success cubic phase gate for universal continuous-variable quantum computation. *Physical Review A - Atomic, Molecular, and Optical Physics*, 91(3):1–7, 2015.

[57] Francesco Arzani, Nicolas Treps, and Giulia Ferrini. Polynomial approximation of non-Gaussian unitaries by counting one photon at a time. *Physical Review A*, 95(5):052352, 5 2017.

[58] Mark Hillery. Photon number divergence in the quantum theory of n -photon down conversion. *Physical Review A*, 42(1):498–502, 7 1990.

[59] E. A.Rojas González, A. Borne, B. Boulanger, J. A. Levenson, and K. Bencheikh. Continuous-Variable Triple-Photon States Quantum Entanglement. *Physical Review Letters*, 120(4):43601, 2018.

[60] Kamel Bencheikh, Fabien Gravier, Julien Douady, Ariel Levenson, and Benot Boulanger. Triple photons: a challenge in nonlinear and quantum optics. *Comptes Rendus Physique*, 8(2):206–220, 2007.

[61] Kevin Zelaya, Sanjib Dey, and Vronique Hussin. Generalized squeezed states. *Physics Letters A*, 382(47):3369–3375, 11 2018.

[62] Samuel L. Braunstein and Robert I. McLachlan. Generalized squeezing. *Physical Review A*, 35(4):1659–1667, 2 1987.

[63] Shohini Ghose and Barry C. Sanders. Non-Gaussian states of light as an offline resource for universal continuous variable quantum information processing. In Ronald E. Meyers and Yanhua Shih, editors, *Quantum Communications and Quantum Imaging III*, volume 5893, page 58930X. International Society for Optics and Photonics, 8 2005.

[64] Ryuji Takagi and Quntao Zhuang. Convex resource theory of non-Gaussianity. *Physical Review A*, 97(6):062337, 6 2018.

[65] Seiji Armstrong, Meng Wang, Run Yan Teh, Qihuang Gong, Qiongyi He, Jiri Janousek, Hans-Albert Bachor, Margaret D. Reid, and Ping Koy Lam. Multipartite EinsteinPodolskyRosen steering and genuine tripartite entanglement with optical networks. *Nature Physics*, 11(2):167–172, 2 2015.

[66] Deny R. Hamel, Lynden K. Shalm, Hannes Hübel, Aaron J. Miller, Francesco Marsili, Varun B. Verma, Richard P. Mirin, Sae Woo Nam, Kevin J. Resch, and Thomas Jennewein. Direct generation of three-photon polarization entanglement. *Nature Photonics*, 8(10):801–807, 10 2014.

[67] Mark Hillery, Vladimr Bužek, and Andr Berthiaume. Quantum secret sharing. *Physical Review A*, 59(3):1829–1834, 3 1999.

[68] Bonny L. Schumaker and Carlton M. Caves. New formalism for two-photon quantum optics. II. Mathematical foundation and compact notation. *Physical Review A*, 31(5):3093–3111, 5 1985.

[69] Konrad Banaszek and Peter L. Knight. Quantum interference in three-photon down-conversion. *Physical Review A*, 55(3):2368–2375, 3 1997.

[70] Anatole Kenfack and Karol Yczkowski. Negativity of the Wigner function as an indicator of non-classicality. *Journal of Optics B: Quantum and Semiclassical Optics*, 6(10):396–404, 10 2004.

[71] A. Mari and J. Eisert. Positive wigner functions render classical simulation of quantum computation efficient. *Physical Review Letters*, 109(23):1–5, 2012.

[72] C. Eichler, D. Bozyigit, and A. Wallraff. Characterizing quantum microwave radiation and its entanglement with superconducting qubits using linear detectors. *Physical Review A*, 86(3):032106, 9 2012.

[73] C. W. Sandbo Chang, M. Simoen, Jos Aumentado, Carlos Sabín, P. Forn-Díaz, A. M. Vadiraj, Fernando Quijandría, G. Johansson, I. Fuentes, and C. M. Wilson. Generating Multimode Entangled Microwaves with a Superconducting Parametric Cavity. *Physical Review Applied*, 10(4):044019, 10 2018.

APPENDICES

Appendix A

Calibration results

A.1 Chapter 6: Single-mode trisqueezed state

Frequency: 4.194 GHz
Temp: 26.6 mK ± 5.3 mK
Gain: 7800000 ± 0.02

A.2 Chapter 4: Tripartite entanglement

A.2.1 Two-mode entanglement

mode 1

Frequency: 4.2044 GHz
Temp: 28.7 mK ± 1.6 mK
Gain: 2760000 ± 1881

mode 2

Frequency: 6.1554 GHz
Temp: 30.8 mK ± 5.3 mK
Gain: 2840000 ± 6600

A.2.2 Tripartite entanglement

System Gain

	Frequencies [GHz]			System Gain/1000		
	Mode 1	Mode 2	Mode 3	Mode 1	Mode 2	Mode 3
CM	4.2039	6.1551	7.5538	$2461 \pm 3, 2485 \pm 3$	$138.2 \pm 0.18, 90.6 \pm 0.12$	$36.8 \pm 0.06, 36.5 \pm 0.06$
BS	4.2042	6.1553	7.5545	$2455 \pm 3, 2450 \pm 3$	$136.8 \pm 0.17, 89.0 \pm 0.13$	$37.1 \pm 0.06, 36.4 \pm 0.06$

Input Temperature

	Frequencies [GHz]			T_{in} [mK]		
	Mode 1	Mode 2	Mode 3	Mode 1	Mode 2	Mode 3
CM	4.2039	6.1551	7.5538	$30.0 \pm 3, 32 \pm 3.1$	$25.6 \pm 3.2, 27 \pm 3.2$	$32.1 \pm 3.6, 25.8 \pm 3.8$
BS	4.2042	6.1553	7.5545	$29 \pm 3.1, 25.7 \pm 3.2$	$28.2 \pm 3, 32.2 \pm 3.2$	$37.3 \pm 3.4, 29.6 \pm 3.6$

System Noise Temperature

	Frequencies [GHz]			T_{N} [K]		
	Mode 1	Mode 2	Mode 3	Mode 1	Mode 2	Mode 3
CM	4.2039	6.1551	7.5538	$6.07 \pm 0.009, 6.07 \pm 0.009$	$6.28 \pm 0.009, 6.05 \pm 0.009$	$8.03 \pm 0.014, 8.03 \pm 0.014$
BS	4.2042	6.1553	7.5545	$6.07 \pm 0.009, 6.07 \pm 0.008$	$6.30 \pm 0.010, 6.08 \pm 0.008$	$7.98 \pm 0.014, 8.05 \pm 0.014$

Table A.1: Calibration results for tripartite entanglement experiments. Each mode is calibrated twice, before measuring the three mode-pair combinations $\{1|2, 1|3, 2|3\}$. The results of both calibrations are shown, color coded by which digitizer was used in the calibration (digitizer 1 in red and digitizer 2 in blue). Only mode 2 is calibrated by both digitizers. Calibrating the digitizers individually eliminates any difference between the two digitizers. The calibrations were done consecutively over a span of a few hours. We observe a drift in system gain of about 1%. The input temperatures ranged from 25 mK to 37 mK throughout all calibrations done. This level of drift in the physical temperature of the cryostat would not be unusual. Further, it is easily verified that for all combinations of frequency and temperature, we are deeply in the quantum regime with $\coth(hf_i/2k_BT_i) = 1.00$ to at least 3 significant figures. It is because of this that we have a relatively large uncertainty in the measured temperature, of order 10%, even the though the uncertainty in the measured noise power, dominated by quantum noise, is much smaller.

Appendix B

Part numbers

Here we list some part numbers for the components used in the experiments.

Type			Brand	Part number	Remakrs
Amplifiers	DC		TI	INA 110	For amplifying SNTJ probe voltage, 100x.
	AC		LNF	LNC4_8A	
			Pasternack	PE1522	
Transmission lines	300 K - 50 K	Cable	Coax.co	SC-219/50-B-B	For the 300 K to 3 K, Beryllium copper cables from Bluefors are used. The connector type maybe different.
		Connector	Cinch Connectivity Solutions Johnson	142-0693-001	
	50 K - 3 K	Cable	Coax.co	SC-219/50-B-B	For the 300 K to 3 K, Beryllium copper cables from Bluefors are used. The connector type maybe different.
		Connector	Cinch Connectivity Solutions Johnson	142-0693-001	
	3 K - 800 mK	Cable	Coax.co	SC-219/50-Nb-Nb SC-219/50-SS-SS	
		Connector	TE	1050611-1	
	800 mK to 100 mK	Cable	Coax.co	SC-219/50-Nb-Nb	
		Connector	TE	1050611-1	
	100 mK - 10 mK	Cable	Coax.co	SC-219/50-Nb-Nb	
		Connector	TE	1050611-1	
	Within 10 mK	Cable	EZ Form Cable	EZ-86-CU/M17	Certain custom assembled cables from EZ Form were also used.
		Connector	Cinch Connectivity Solutions Johnson	142-0693-001	
Attenuators	Low temperature	1 dB	XMA	2082-6418-01-Cryo-1603	
		3 dB	XMA	2082-6418-03-Cryo-1605	
		6 dB	XMA	2082-6418-061-Cryo	
		10 dB	XMA	2082-6418-10-Cryo	
		20 dB	XMA	2082-6418-20-Cryo	
		50 Ohm termination	XMA	2001-7010-02-Cryo-1603	
Circulators			Raditek	RADC-4-8-Cryo-0.02-4K-S23-1NR-MS-b	
BiasTee			INMET	64671 8800SFF2-12	
Microwave switch	Low temperature		Radiall	R570432000 0-18 GHz	For switching between SNTJ and device at the MXC stage.
	Room temperature		miniCircuit	MSP2T-18-12	For toggling pump/signal ON/OFF at RT.
Resistors	SNTJ biasing	100 kOhm	Stackpole Electronics Inc	RNF14BTE100K	
	SNTJ probing	1 kOhm	Yageo	MFP-25BRD52-1K	
DC wires	Magnetic coil		Supercon	SC-T48B-M-0.3mm	Lakeshore wire was used down to 4 K, then Supercon wire connected from 4 K to 10 mK.
			Lakeshore	WCT-RB-34-100	
	SNTJ biasing/probing		Supercon	SC-T48B-M-0.3mm	
			Lakeshore	WCT-RB-34-100	
	HEMT biasing		Lakeshore	WCT-RB-34-100	
Filters	AC	LPF 8 GHz	RLC Electronics	F-30-8000-R, 1346	For filtering the input/output lines
		LPF 18 GHz	RLC Electronics	F-30-18.0-R,1522	For filtering the pump line.
	DC	Stainless steel powder filter	Remington	44 AWG Cu wire	For filtering the SNTJ bias signal.
			Alfa Aesa	Fe:Cr:Ni 70:19:11 wt%	
Microwave equipment	Generators		Rohde and Schwarz	SGS100A	For pumping the parametric processes.
	AWG	High frequency	Aeroflex	3025C	For generating classically correlated signals.
		Low frequency	Tektronics	AFG2021	For biasing the SNTJ in calibrations.
	Digitizer		Aeroflex	3035C, 3036C	
	DC voltage source		Yokogawa	GS200	For driving the DC coil.
	VNA		Agilent	E5071C	
Custom parts	Sample holder		machined OFHC copper		
	Aluminum shield		machined 6061 aluminum		

Appendix C

Additional data

C.1 Numerical values for reconstructed density matrix for the single-mode trisqueezed state

$$\rho_{\text{real}} = \begin{pmatrix} 0.78 & 0.00 & 0.00 & 0.12 & -0.03 & -0.01 & 0.00 & -0.01 & -0.01 & -0.03 \\ 0.00 & 0.05 & -0.01 & 0.00 & 0.01 & 0.00 & 0.00 & 0.00 & 0.01 & 0.00 \\ 0.00 & -0.01 & 0.02 & 0.01 & -0.01 & 0.01 & 0.00 & 0.00 & 0.00 & 0.00 \\ 0.12 & 0.00 & 0.01 & 0.05 & -0.01 & 0.01 & 0.02 & -0.01 & 0.00 & 0.00 \\ -0.03 & 0.01 & -0.01 & -0.01 & 0.02 & 0.00 & 0.00 & 0.01 & 0.00 & 0.00 \\ -0.01 & 0.00 & 0.01 & 0.01 & 0.00 & 0.01 & 0.00 & 0.00 & 0.00 & 0.00 \\ 0.00 & 0.00 & 0.00 & 0.02 & 0.00 & 0.00 & 0.01 & 0.00 & 0.00 & 0.00 \\ -0.01 & 0.00 & 0.00 & -0.01 & 0.01 & 0.00 & 0.00 & 0.01 & 0.00 & 0.00 \\ -0.01 & 0.01 & 0.00 & 0.00 & 0.00 & 0.00 & 0.00 & 0.00 & 0.00 & 0.00 \\ -0.03 & 0.00 & 0.00 & 0.00 & 0.00 & 0.00 & 0.00 & 0.00 & 0.00 & 0.00 \end{pmatrix}$$

$$\rho_{\text{imag}} = \begin{pmatrix} 0.00 & -0.02 & 0.00 & -0.13 & 0.01 & -0.01 & -0.08 & 0.02 & 0.01 & -0.03 \\ 0.02 & 0.00 & 0.03 & 0.02 & -0.02 & 0.02 & 0.00 & -0.01 & 0.01 & 0.00 \\ 0.00 & -0.03 & 0.00 & 0.00 & -0.01 & -0.01 & 0.00 & 0.00 & -0.01 & 0.00 \\ 0.13 & -0.02 & 0.00 & 0.00 & -0.01 & -0.01 & -0.02 & 0.00 & 0.00 & -0.01 \\ -0.01 & 0.02 & 0.01 & 0.01 & 0.00 & 0.00 & 0.00 & -0.01 & 0.00 & 0.00 \\ 0.01 & -0.02 & 0.01 & 0.01 & 0.00 & 0.00 & 0.00 & 0.00 & 0.00 & 0.00 \\ 0.08 & 0.00 & 0.00 & 0.02 & 0.00 & 0.00 & 0.00 & 0.00 & 0.00 & 0.00 \\ -0.02 & 0.01 & 0.00 & 0.00 & 0.01 & 0.00 & 0.00 & 0.00 & 0.00 & 0.00 \\ -0.01 & -0.01 & 0.01 & 0.00 & 0.00 & 0.00 & 0.00 & 0.00 & 0.00 & 0.00 \\ 0.03 & 0.00 & 0.00 & 0.01 & 0.00 & 0.00 & 0.00 & 0.00 & 0.00 & 0.00 \end{pmatrix}$$